

Chapter 2

Mechanism of Multidimensional Optical Storage

The principles of multidimensional storage involve a lot of research area. The chapter focuses on the discussion of physical and chemical mechanisms of interaction of light with materials in the optical storage.

2.1 Photophysics and Photochemistry

Photophysics and photochemistry are basic principles for multidimension storage as both deals with the impact of energy in the form of photons on materials. Photochemistry focuses on the chemistry involved as a material is impacted by photons, where as photophysics deals with physical changes that result from the impact of photons. The essential theory of photophysics and photochemistry will be applied in multidimension optical storage. There are lot of books introduced as N.S. Allen, Photochemistry in 2010, Vincenzo Balzani and Paola Ceroni etc., Photochemistry and Photophysics in 2014, C. Carraher, Polymer Chemistry in 2008, R. Dessauer, Photochemistry in 2006, D. Neckers and Advances in Photochemistry in 2007, D. Phillips and Polymer Photophysics in 2007, V. Ramamurthy Semiconductor Photochemistry and Photophysics in 2003, N. Turro, V. Ramamurthy and J. Scaiano, Principles of Molecular Photochemistry in 2009 which are important significance for this research [1–4].

This section will focus on some of the basic principles related to photophysics and photochemistry followed by general examples. Finally, these principles will be related to photosynthesis. In many ways, there is a great similarity between a material's behavior when struck by photons, whether the material is small or macromolecular. Differences are related to size and the ability of polymers to transfer the effects of radiation from one site to another within the chain or macromolecular complex. The importance of the interaction with photons in the natural world can hardly be overstated. It forms the basis for photosynthesis converting carbon dioxide and water into more complex plant-associated structures.

Polymer photochemistry and physics have been recently reviewed, and readers are encouraged to investigate this further in the suggested readings given at the end of the chapter. Here, introduce some of the basic concepts of photophysics and photochemistry, and illustrate the use of photochemistry and photophysics in the important area of solar energy conversion.

Photophysics involves the absorption, transfer, movement, emission of electromagnetic and light energy without chemical reactions. By comparison, photochemistry involves the interaction of electromagnetic energy that results in chemical reactions. Briefly review the two major types of spectroscopy with respect to light. In absorption, the detector is placed along the direction of the incoming light and the transmitted light is measured. In emission studies, the detector is placed at some angle, generally 90° , away from the incoming light. When absorption of light occurs, the resulting polymer P^* , contains excess energy and is excited as



The light can be simply reemitted:



Of much greater interest is light migration, either along the polymer backbone or to another chain. This migration allows the energy to move to a site of interest. Thus, for plants, the site of interest is chlorophyll. These 'light-gathering' sites are referred to as antennas. Natural antennas include chlorophyll, carotenoids, and special pigment-containing proteins. These antenna sites harvest the light by absorbing the light photon and storing it in the form of an electron, which is promoted to an excited singlet energy state (or other energy state) by the absorbed light.

Bimolecular occurrences can occur, leading to an electronic relaxation called quenching. In the approach P^* find another molecule or part of the same chain A , and transferring the energy to A .



Generally, the quenching molecule or site is initially in its ground state. Eliminating chemical rearrangements, quenching is most likely ends with electronic energy transfer, complex formation, or increased nonradioactive decay. Electronic transfer involves an exothermic process, in which part of the energy is absorbed as heat and part is emitted as fluorescence or phosphorescence radiation. Polarized light is taken on in fluorescence depolarization, also known as luminescence anisotropy. Thus, if the chain segments are moving at about the same rate as the reemission, part of the light is depolarized. The extent of depolarization is then a measure of the segmental chain motions.

Complex formation is important in photophysics. Two terms need to be described here. First, an exciplex is an excited state complex formed between

photophysics and photochemistry two different kinds of molecules, that one is excited and other one is in ground state. The second term, excimer is similar, except the complex is formed between like molecules. Here focus on excimer complexes that form between two like polymer chains or within the same polymer chain. Such complexes can be formed between two aromatic structures. Resonance interactions between aromatic structures, such as two phenyl rings in polystyrene, give a weak intermolecular force formed from attractions between the π -electrons of the two aromatic entities. Excimers involving such aromatic structures give strong fluorescence. Excimer formation can be described as follows where $[PP]^*$ is the excimer:



The excimer decays, giving two ground-state aromatic sites and emission of fluorescence by:



As always, the energy of the light emitted is less than that originally taken on. Through studying the amount and energy of the fluorescence, radiation decay rates, depolarization effects, excimer stability, and structure can be determined.

2.1.1 Light Absorption

Light is composed of particles known as photons, each of which has the energy of Planck's quantum, hc/λ ; where h is Planck's constant, c is velocity of light, and λ is the wavelength of the radiation. Light has dualistic properties of both waves and particles; ejection of electrons from an atom as a result of light bombardment is due to the particle behavior, whereas the observed light diffraction at gratings is attributed to the wave properties. The different processes related to light interactions with molecules can be represented as in Fig. 2.1. The absorption of light by materials produces physical and chemical changes. On the negative side, such absorption can lead to discoloration generally as a response to unwanted changes in the material's structure. Absorption also can lead to a loss in physical properties, such as strength. In the biological world, it is responsible for a multitude of problems, including skin cancer. It is one of the chief modes of weathering by materials. Here focus on the positive changes effected by the absorption of light. Absorption of light has intentionally resulted in polymer cross-linking and associated insolubilization. This forms the basis for coatings and negative-lithographic resists. Light-induced chain breakage is the basis for positive-lithographic resists. Photoconductivity forms the basis for photocopying, and photovoltaic effects form the basis for solar cells being developed to harvest light energy. It is important to remember that the basic laws governing small and large molecules are the same.

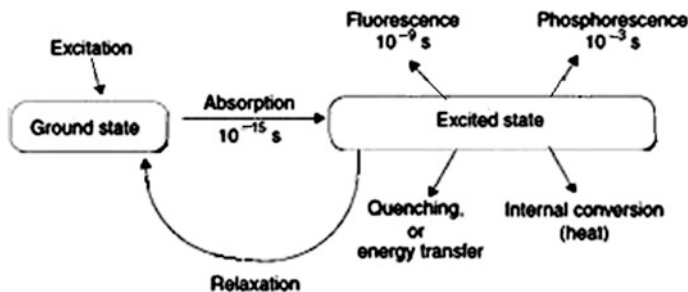


Fig. 2.1 Different processes associated with light interaction with a molecule

The Grotthus–Draper law states that photophysical/photochemical reactions occur only when a photon of light is absorbed. This forms the basis for the First Law of Photochemistry—that is, only light that is absorbed can have a photophysical/photochemical effect and can write as following:



where M^* is M after it has taken on some light energy acquired during a photochemical reaction. The asterisk is used to show that M is now in an excited state. Optical transmittance T is a measure of how much light that enters a sample is absorbed as:

$$T = I/I_\infty \quad (2.7)$$

If no light is absorbed then $I = I_0$. Low transmittance values indicate that lots of the light has been absorbed.

Most spectrophotometers give their results in optical absorbency A , or optical density which is defined by:

$$A = \log(I/I_0) \quad (2.8)$$

so that

$$A = \log(1/T) = -\log T \quad (2.9)$$

Beer's law states that A , the absorbance of chromophores, increases in proportion to the concentration of the chromophores, where k is a constant.

$$A = kc \quad (2.10)$$

Beer's law predicts a straight-line relationship between absorbance and concentration and is often used to determine the concentration of an unknown after construction of the known absorbance verses concentration line.

The optical path l , is the distance the light travels through the sample. This is seen in looking at the color in a swimming pool, where the water is deeper colored at the deep end because the optical path is greater. This is expressed by Lambert's law, where k' is another empirical constant as:

$$A = k'l \quad (2.11)$$

To the eye some colors appear similar but may differ in intensity, when c and l are the same. These solutions have a larger molar absorption coefficient, ϵ , meaning they adsorb more. The larger the adsorption coefficient the more the material adsorbs. The Beer–Lambert law combines the two laws and giving by:

$$A = \epsilon lc \quad (2.12)$$

The proportionality constant in the Lambert's law is ϵ . The extinction coefficients of chromophores vary widely from $100 < M \text{ cm}^{-1}$, for a so-called forbidden transition, to greater than $10^5 M \text{ cm}^{-1}$ for fully allowed transitions, can redefine the elements of the Beer–Lambert law, where l is the sample thickness and c is the molar concentration of chromophores. This can be rearranged to determine the penetration depth of light into a polymer material. Here l is defined as the path length, where 90 % of the light of a particular wavelength is absorbed so A approaches l is giving:

$$l(\text{in } \mu\text{m}) = 10^4 \epsilon c \quad (2.13)$$

This relationship holds when the polymer chromophore (or any chromophore) is uniformly distributed in a solution or bulk. In polymers with a high chromophore concentration, l is small and the photochemical/photophysical phenomenon occurs largely in a thin surface area. As examine the color of a red wine that the wine contains color sites or chromophores. The photons that are not captured pass through and give us the red coloration. Can see color became a chromophore interacts with light. Molecules that absorb photons of energy corresponding to wavelengths in the range 190 to $\sim 1000 \text{ nm}$ absorb in the UV-VIS region of the spectrum.

The molecule that absorbs a photon of light becomes excited. The energy that is absorbed can be translated into rotational, vibrational, or electronic modes. The quantized internal energy E_{int} of a molecule in its electronic ground or excited state can be approximated, with sufficient accuracy for analytical purposes by:

$$E_{\text{int}} = E_{\text{el}} + E_{\text{vib}} + E_{\text{rot}} \quad (2.14)$$

where E_{el} , E_{vib} , and E_{rot} are the electronic, vibrational, and rotational energies, respectively. According to the Born–Oppenheimer approximation, electronic transitions are much faster than atomic motion. Upon excitation, electronic transitions occur in about 10^{-15} s , which is very fast compared to the characteristic time scale

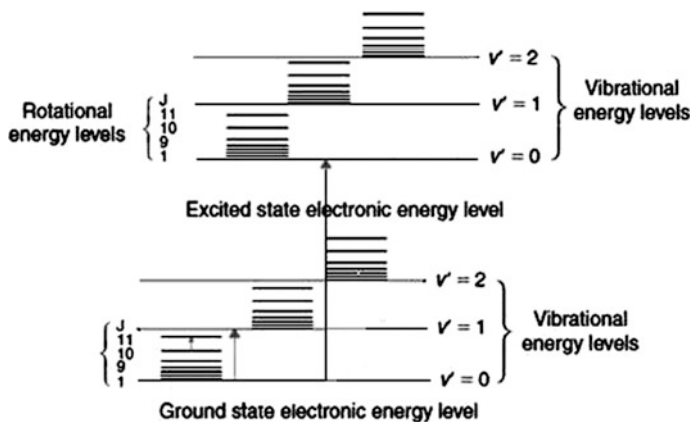


Fig. 2.2 The relative ordering of electronic, vibrational and rotational energy levels

for molecular vibrations of 10^{-10} to 10^{-12} s. Hence, the influence of vibrational and rotational motions on electronic states should be almost negligible. Franck–Condon stated that electronic transition is most likely to occur without changes in the position of the nuclei in the molecular entity and its environment. It is then possible to describe the molecular energy by a potential energy diagram in which the vibrational energies are superimposed upon the electronic curves as in Fig. 2.2.

For most molecules, only one or two lower energy electronic transitions are normally postulated. Thus one would expect that the UV-VIS spectrum would be relatively simple. This is often not the case. The question shows that why are many bands often exhibiting additional features. The answer lies in the Franck–Condon principle, by which vibronic couplings are possible for polyatomic molecules. Indeed, both vibronic and electronic transitions will be observed in the spectrum, generating vibrationally structured bands, and sometimes even leading to broad unresolved bands. Each resolved absorption peak corresponds to a vibronic transition, which is a particular electronic transition coupled with a vibrational mode belonging to the chromophore. For solids (when possible) and liquids, the rotational lines are broad and overlapping, so that no rotational structure is distinguishable [5].

To apply this concept for a simple diatomic molecule, the example is given in Fig. 2.3. At room temperature, according to the Boltzman distribution, most of the molecules are in the lowest vibrational level v of the ground state, i.e., $v = 0$. The absorption spectrum presented in Fig. 2.3b exhibits, in addition to the pure electronic transition that the so-called 0–0 transition, several vibronic peaks whose intensities depend on the relative position and shape of the potential curve.

The transition from the ground to the excited state, where the excitation goes from $v = 0$ (in the ground state) to $v = 2$ (in the excited state), is the most probable for vertical transitions because it falls on the highest point in the vibrational probability curve in the excited state. Yet many additional transitions occur, so that

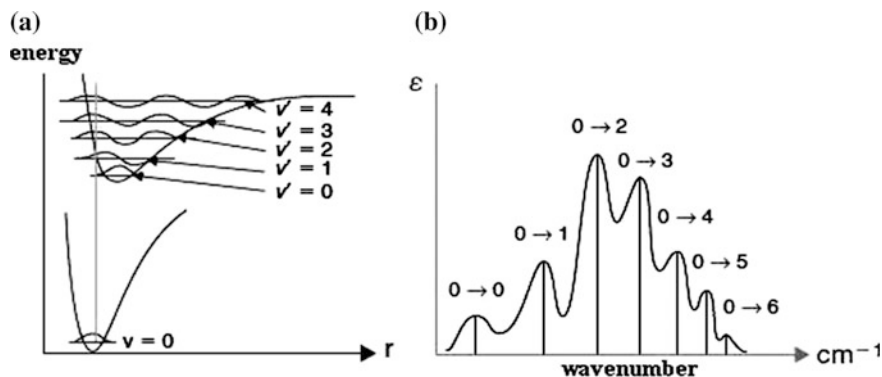


Fig. 2.3 **a** Potential energy diagram for a diatomic molecule, illustrating the Franck–Condon excitation. **b** Intensity distribution among vibronic bands as determined by the Franck–Condon principle

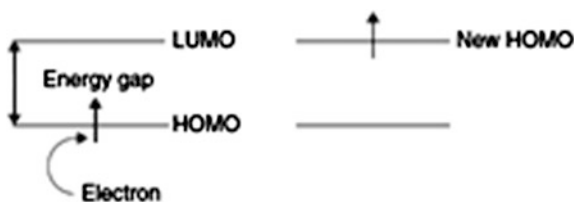
the fine structure of the vibronic broad band is a result of the probabilities for the different transitions between the vibronic levels.

There are two kinds of spectra, i.e., excitation and absorption in this action. The absorption and excitation spectra are distinct but usually overlap, energy levels sometimes to the extent that they are nearly indistinguishable.

The excitation spectrum is the spectrum of light emitted by the material as a function of the excitation wavelength. The absorption spectrum is the spectrum of light absorbed by the material as a function of wavelength. The origin of the occasional discrepancies between the excitation and absorption spectra are due to the differences in structures between the ground and the excited states or the presence of photo reactions or the presence of nonradiative processes that relax the molecule to the ground state without passing through the luminescent states, i.e., S_1 and T_1 .

Visible color is normally a result of changes in the electron states. Molecules that reside in the lowest energy level are said to be in the ground state or unexcited state. Restricted the attention to the electrons that are in the highest occupied molecular orbital (HOMO) and the lowest unoccupied molecular orbital (LUMO). These orbitals are often referred to as the frontier orbitals. Excitation of photons results in the movement of electrons from the HOMO to the LUMO as shown in Fig. 2.4. Photon energies can vary. Only one photon can be accepted at a time by an orbital.

Fig. 2.4 A photon being absorbed by a single molecule of chromophore



This is stated in the Stark–Einstein law also known as the Second Law of Photochemistry—if a species absorbs radiation, then one particle (molecule, ion, atom, etc.) is excited for each quantum of radiation (photon) that is absorbed. [6]

Remember that a powerful lamp will have a greater photon flux than a weaker lamp. Further, photons enter a system one photon at a time. Thus, every photon absorbed does not result in bond breakage or other possible measurable effect. The quantum yield ϕ is a measure of the effectiveness for effecting the desired outcome, possibly bond breakage, and formation of free radicals:

$$\phi = N_m/N_p \quad (2.15)$$

where N_m is number of molecules of reactant consumed, N_p is number of photo consumed.

Quantum yields can provide information about the electronic excited state relaxation processes, such as the rates of radiative and nonradiative energy gap.

Moreover, they can also find applications in the determination of chemical structures and sample purity. The emission quantum yield can be defined as the fraction of molecules that emits a photon after direct excitation by a light source. So emission quantum yield is also a measure of the relative probability for radiative relaxation of the electronically excited molecules. Quantum yields vary greatly, the photons range from very ineffective (10^{-6}) to very effective (10^6). If values >1 indicate that some chain reaction, such as in a polymerization. To differentiate between the primary quantum yield, which focuses on only the first event, here the quantum yield cannot be >1 and secondary quantum yield, which focuses on the total number of molecules formed via secondary reactions that the quantum yield can be high. The common emission quantum yield measurement involves the comparison of a very dilute solution of the studied sample with a solution of approximately equal optical density of a compound of known quantum yield, i.e., standard reference. The quantum yield of an unknown sample is related to that of a standard by Eq. (2.16) as:

$$\Phi_u = \left[\frac{(A_s F_u n^2)}{(A_u F_s n_0^2)} \right] \Phi_s \quad (2.16)$$

where, the subscript u refers to ‘unknown,’ and s to the comparative standard, Φ is the quantum yield, A is the absorbance at a given excitation wavelength, F is the integrated emission area across the band, and n and n_0 are the refractive indices of the solvent containing the unknown and the standard, respectively. For the most accurate measurements, both the sample and standard solutions should have low absorptions (≤ 0.05) and have the similar absorptions at the same excitation wavelength.

2.1.2 Luminescence

Luminescence is a form of cold body radiation. Older TV screens operated on the principle of luminescence, by which the emission of light occurs when they are relatively cool. Luminescence includes phosphorescence and fluorescence. In a TV, electrons are accelerated by a large electron gun sitting behind the screen. In the black-and-white sets, the electrons slam into the screen surface, which is coated with a phosphor that emits light when hit with an electron. Only the phosphor that is hit with these electrons gives off light. The same principle operates in the old-generation color TVs, except the inside of the screen is coated with thousands of groups of dots, each group consisting of three dots (red, green, and blue). The kinetic energy of the electrons is absorbed by the phosphor and reemitted as visible light to be seen. Fluorescence involves the molecular absorption of a photon that triggers the emission of a photon of longer wavelength, i.e., less energy as in Fig. 2.2. The energy difference ends up as rotational, vibrational, or heat energy losses. Here excitation is described as



and emission as



where S_0 is the ground state and S_1 is the first excited state. The excited state molecule can relax by a number of different, generally competing pathways. One of these pathways is conversion to a triplet state that can subsequently relax through phosphorescence or some secondary nonradiative step. Relaxation of the excited state can also occur through fluorescence quenching. Molecular oxygen is a particularly efficient quenching molecule because of its unusual triplet ground state.

Watch hands that can be seen in the dark allow to read the time without turning on a light. These watch hands typically are painted with phosphorescent paint. Like fluorescence, phosphorescence is the emission of light by a material previously hit by electromagnetic radiation. Unlike fluorescence, phosphorescence emission persists as an afterglow for some time after the radiation has stopped. The shorter end of the duration for continued light emission is 10^{-3} s but the process can persist for hours or days. An energy level diagram representing the different states and transitions is called a Jablonski diagram or a state diagram. The Jablonski diagram was first introduced in 1935, a slightly modified version is presented in Fig. 2.5. The different energy levels are given in this figure, where S_0 represents the electronic ground state and S_1 and S_2 represent the first and second singlet excited states, respectively. The first and second triplet states are denoted T_1 and T_2 , respectively. In the singlet states, all electron spins are paired and the multiplicity of this state is 1. The subscript indicates the relative energetic position (electronic level) compared to other states of the same multiplicity. On the other hand, in the triplet states, two electrons are no longer antiparallel and the multiplicity is 3. The triplet state is more

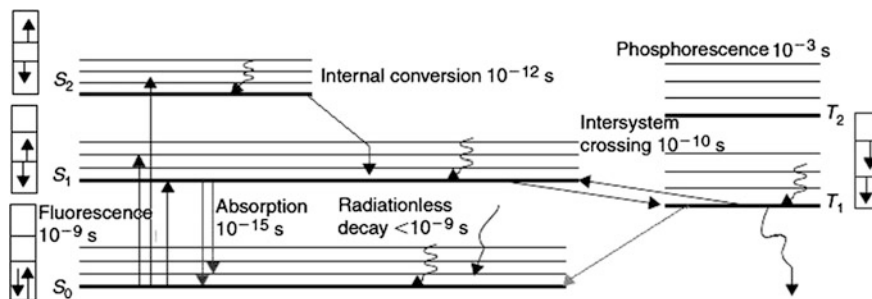


Fig. 2.5 Jablonski diagram showing the various processes associated with light absorption and their time scale. *Arrows in boxes, the relative spin states of the paired electrons*

stable than the singlet counterpart (S) and the source for this energy difference is created by the difference in the Coulomb repulsion energies between the two electrons in the singlet versus triplet states and the increase in degree of freedom of the magnetic spins. Because the electrons in the singlet excited state are confined within the same orbital, the Coulomb repulsive energy between them is higher than in the triplet excited state where these electrons are now in separate orbitals. The splitting between these two states (S - T) also depends on the nature of the orbital.

Consider a case, where the two orbitals involved in a transition are similar, i.e., two p -orbitals of an atom, or two π -orbitals of an aromatic hydrocarbon. For this situation, the overlap between them may be high, and the two electrons will be forced to be close to each other resulting in the S - T splitting being large. The other situation is the case where the two orbitals are different (i.e., n - π^* or d - π transitions), resulting in a small overlap. Because the overlap is small that the two electrons will have their own region of space in which to spread, resulting in a minimization of the repulsive interactions between them, and hence the S - T splitting will be small. Absorption occurs on a time scale of about 10^{-15} s. When inducing the promotion of an electron from the HOMO to the LUMO, the molecule passes from an electronic ground singlet state S_0 (for diamagnetic molecules) to a vibrational level of an upper singlet or triplet excited state S_n or T_n , respectively. The energy of the absorbed photon determines which excited state is accessible. After a while, the excited molecule relaxes to the ground state via either radiative with emission of light or nonradiative without emission of light processes. The radiative processes for diamagnetic molecules include either the spin-allowed fluorescence or spin-forbidden phosphorescence. Nonradiative processes include intersystem crossings (ISCs), a process allowing a molecule to relax from the S_n to the T_n manifolds, and internal conversions (IC and IP), a stepwise (vibrational) energy loss process relaxing molecules from upper excited states to any other state without or with a change in state multiplicity, respectively. An internal conversion (IC) is observed when a molecule lying in the excited state relaxes to a lower excited state. This is a radiationless transition between two different electronic states of the same multiplicity and is possible when there is a good overlap of the vibrational wave functions or probabilities that are involved between the two states to beginning and final.

2.2 Photoinduced Electron Transfer Process

Internal conversion occurs on a time scale of 10^{-12} s, which is a time scale associated with molecular vibrations. A similar process occurs for an internal conversion, (IP) when it is accompanied by a change in multiplicity such as triplet T_1 down to S_0 . Upon nonradiative relaxation, heat is released. This heat is transferred to the media by collision with neighboring molecules. Fluorescence is a radiative process in a diamagnetic molecule involving two states (excited and ground states) of the same multiplicity, for example $S_1 \rightarrow S_0$ and $S_2 \rightarrow S_0$ is shown in Fig. 2.6. Fluorescence spectra show the intensity of the emitted light versus the wavelength. A fluorescence spectrum is obtained by initial irradiation of the sample, normally at a single wavelength, where the molecule absorbs light. The lifetime of fluorescence is typically on the order of 10^{-8} to 10^{-9} s, i.e., an ns time scale for organic molecules and faster for metal-containing compounds (10^{-10} s or shorter). In general, the fluorescence band, typically $S_1 \rightarrow S_0$, is a mirror image of the absorption band ($S_0 \rightarrow S_1$), as illustrated in Figs. 2.6 and 2.7. This is particularly true for rigid

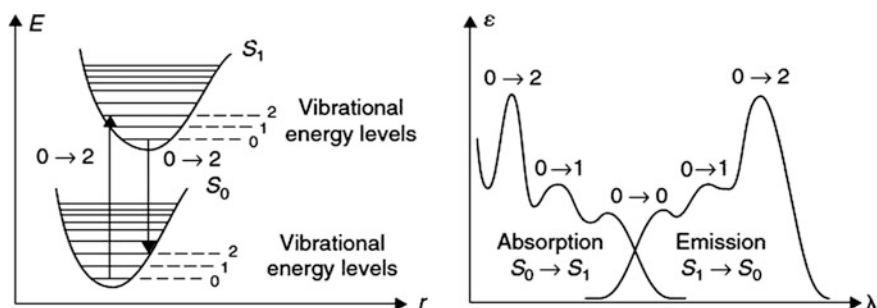


Fig. 2.6 Potential energy curves and vibronic structure in fluorescence spectra

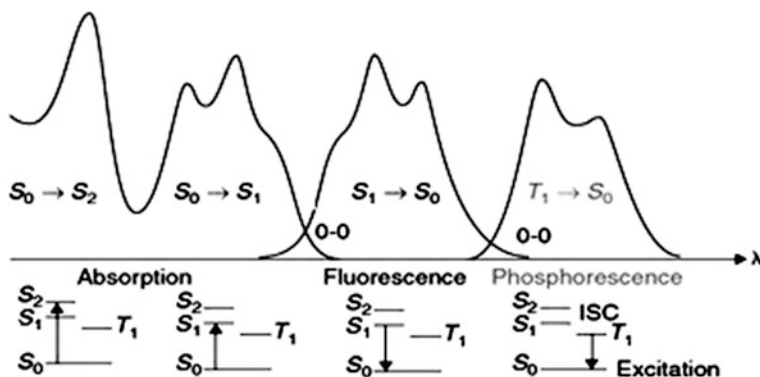


Fig. 2.7 Relative positions of absorption, fluorescence and phosphorescence. The 0-0 is common to both absorption and fluorescence spectra (see Fig. 2.6). ISC, Intersystem crossing

molecules, such as aromatics. Once again, the Franck–Condon principle is applicable, and hence the presence of vibronic bands is expected in the fluorescence band. However, there are numerous exceptions to this rule, particularly, when the molecule changes geometry in its excited state. Another observation is that the emission is usually red shifted in comparison with absorption. This is because the vibronic energy levels involved are lower for fluorescence and higher for absorption, as illustrated in Fig. 2.6. The difference in wavelength between the 0–0 absorption and the emission band is usually known as the Stokes shift. The magnitude of the Stokes shift gives an indication of the extent of geometry difference between the ground and excited states of a molecule as well as the solvent–solute reorganization. Another nonradiative process that can take place is known as intersystem crossing from a single to a triplet or triplet to a single state. This process is very rapid for metal-containing compounds. This process can take place on a time scale of $\sim 10^{-6}$ to 10^{-8} s for an organic molecule, while for organometallics it is $\sim 10^{-11}$ s [7, 8].

This rate enhancement is due to spin-orbit coupling present in the metal-containing systems—that is, an interaction between the spin angular momentum and the orbital angular momentum, which allows mixing of the spin angular momentum with the orbital angular momentum of S_n and T_n states. Thus, these singlet and triplet states are no longer “pure” singlets and triplets, and the transition from one state to the other is less forbidden by multiplicity rules. A rate increase in intersystem crossing can also be achieved by the heavy atom effect, arising from an increased mixing of spin and orbital quantum number with increased atomic number. This is accomplished either through the introduction of heavy atoms into the molecule via chemical bonding (internal heavy atom effect) or with the solvent (external heavy atom effect). The spin-orbit interaction energy of atoms grows with the fourth power of the atomic number Z . In addition to the increase in the intersystem crossing rate, heavy atoms exert more effects, which can be summarized as follows. Their presence acts (1) to decrease the phosphorescence lifetime due to an increase in the nonradiative rates, (2) to decrease the fluorescence lifetime, and (3) to increase the phosphorescence quantum yield. The presence of a heavy atom affects not only the rate for intersystem crossing but also the energy gap between the singlet and the triplet states, where the rate for the intersystem crossing increases as the energy gap between S_1 and T_1 decreases. Moreover, the nature of the excited state exerts an important effect on the intersystem crossing. For example, the $S_1(n, \pi^*) \rightarrow T_2(\pi, \pi^*)$ (e.g., as in benzophenone) transition occurs almost three orders of magnitude faster than the $S_1(\pi, \pi^*) \rightarrow T_2(\pi, \pi^*)$ transition for example in anthracene.

Relaxation of triplet state molecules to the ground state can be achieved by either internal conversion (nonradiative IP) or phosphorescence (radiative). Emissions from triplet states, i.e., phosphorescence that exhibit longer lifetimes than fluorescence. These long-lived emissions occur on time scale of 10^{-3} s for organic samples and 10^{-5} to 10^{-7} s for metal-containing species. This difference between the fluorescence and the phosphorescence is associated with the fact that it involves a spin-forbidden electronic transition. Moreover, as already noted, the

phosphorescence bands are always red shifted in comparison with their fluorescence counterpart because of the relative stability of the triplet state compared to the singlet manifold as shown in Fig. 2.7. Nonradiative processes in the triplet states increase exponentially with a decrease in triplet energies (energy gap law). Hence phosphorescence is more difficult to observe when the triplet states are present in very low energy levels. It is also often easier to observe phosphorescence at lower temperatures, at which the thermal decay is further inhibited.

2.2.1 Emission Lifetime

The luminescence lifetime is the average time the molecule remains in its excited state before the photon is emitted. From a kinetic viewpoint, the lifetime can be defined by the rate of depopulation of the excited (singlet or triplet) states following an optical excitation from the ground state. Luminescence generally follows first-order kinetics and can be described as follows.

$$[S_1] = [S_1]_0 e^{-\Gamma t} \quad (2.19)$$

where $[S_1]$ is the concentration of the excited state molecules at time t , $[S_1]_0$ is the initial concentration and Γ is the decay rate or inverse of the luminescence lifetime. Various radiative and nonradiative processes can decrease the excited state population. Here, the overall or total decay rate is the sum of these rates:

$$\Gamma_{\text{total}} = \Gamma_{\text{radiative}} + \Gamma_{\text{nonradiative}} \quad (2.20)$$

For a complete photophysical study, it is essential to study not only the emission spectrum but also the time domain because it can reveal a great deal of information about the rates and hence the kinetics of intramolecular and intermolecular processes. The fundamental techniques used to characterize emission lifetimes of the fluorescence and the phosphorescence are briefly described next.

When a molecule is excited (Eq. 2.21), it is promoted from the ground to the excited state. This excited molecule can then relax to the ground state after emission lifetime losing its extra energy gained from the exciting source via a radiative (Eq. 2.22) and nonradiative (Eq. 2.23) processes:



Therefore, can write as:

$$-\frac{d[A^*]}{dt} = (k_r + k_n)[A^*]t = -\frac{t}{\tau} \quad (2.24)$$

where $[A^*]$ is the concentration of the species A in its excited state at a given time t and k_r and k_n are the rate constants for the radiative and nonradiative processes, respectively. The relative concentration of A^* is given by

$$\ln \frac{[A^*]_t}{[A^*]_{t=0}} = -(k_r + k_n)t = -\frac{t}{\tau} \quad (2.25)$$

Hence, the mean lifetime (τ) of $[A^*]$ is

$$\tau = 1/(k_r + k_n) \quad (2.26)$$

where k_r and k_n are the rate constants for the radiative and nonradiative processes, respectively, represented by Eqs. (2.22) and (2.23). Thus, the measured unimolecular radiative lifetime is the reciprocal of the sum of the unimolecular rate constants for all the deactivation processes. The general form of the equation is given by

$$\tau = \frac{1}{\sum_i k_i} \quad (2.27)$$

where τ is observed radiative lifetime and the rate constant k_i represents the unimolecular or pseudo-unimolecular processes that deactivate A^* . The lifetime can be measured from a time-resolved experiment in which a very short pulse excitation is made, followed by measurement of the time dependent intensity, as illustrated in Fig. 2.8. The intensity decays are often measured through a polarizer oriented at some angle such as about from the vertical z -axis to avoid the effects of Introduction to Photophysics and Photochemistry anisotropy on the intensity decay. Then, the log of the recorded intensity is plotted against time to obtain a straight line predictable from the integration of the Eq. (2.24). The slope of this line is the negative reciprocal of the lifetime. When more than one lifetime is present in the decay traces, then there is more than one radiative pathway to relaxation. This often signifies that more than one species is emitting light at the excitation wavelength. The analysis of such multicomponent decays involves the deconvolution of an equation of the same form of Eq. (2.24) where a weighing factor for each component is added to each component. One possible explanation for the polyexponential curves can be an exciton process. The exciton phenomenon is a delocalization of excitation energy through a material. A description of this is given in Fig. 2.9. It shows a one-dimensional coordination or organometallic polymer denoted by $-[M_n]-[M_n]-[M_n]-[M]-$, where M_n represent a mononuclear ($n > 1$) or polynuclear center ($n = 1$). The incident irradiation is absorbed by a single

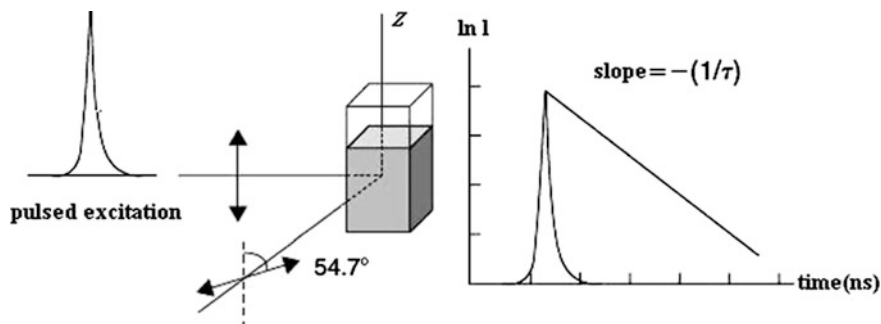


Fig. 2.8 Time-domain lifetime measurement

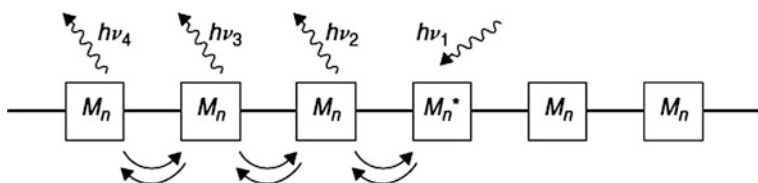


Fig. 2.9 The excitation phenomenon and process

chromophore, $[M_n]$, along the backbone, and then this stored energy is reversibly transmitted via an energy transfer process to the neighboring chromophore (with no thermodynamic gain or loss; i.e., $\Delta G^0 = 0$). This newly created chromophore can reemit, or not, the light ($h\nu_2$, $h\nu_3$, $h\nu_4$, ...) at a given moment. The interactions between the different units in the excited states are called excimers. These excimers can be excited dimers, trimers, tetramers, etc. These excited oligomers have different wavelengths and emission lifetimes. The extent of the interactions in the excited state (dimers, trimers, tetramers) is hard to predict because it depends on the amplitude of the interactions and the relaxation rates. Hence, the lifetime decay curve will have a polyexponential nature.

2.2.2 Ground and Excited State Molecular Interactions

Ground-state intermolecular interactions are present in some systems and require measurements of the binding constants. These interactions are manifested by the spectral changes experienced in the absorption spectra. Therefore, these changes can be monitored as a function of the concentration of the substrates leading to the extraction of the binding constants. On the other hand, intermolecular and intramolecular excited state interactions refer to the energy and electron transfer operating in the excited states of different dyad or polyad systems. These can also be

excimers, dimers, or oligomers that are formed only in the excited states. Studies of photoinduced energy and electron transfers involve the measurement of their corresponding rates. The theory and methods used to characterize the different types of interactions are described next. Binding constant considerations are described elsewhere.

2.2.3 Energy and Electron Transfer

The energy and electron transfer is excited state interactions and reactions indeed. The possible deactivation pathways of the excited state are summarized in Fig. 2.10. The fluorescence and phosphorescence relaxation pathways and the thermal deactivation processes. A transfer of the excitation energy from the donor to the acceptor will occur when an energy acceptor molecule is placed at the proximity of an excited energy donor molecule. After energy transfer, the donor relaxes to its ground state and the acceptor is promoted to one of its excited states. A photoinduced electron transfer can be initiated after photoexcitation when an excited single electron in the LUMO of the electron donor is transferred to a vacant molecular orbital (LUMO) of the acceptor. The mechanisms for the energy and electron transfers are outlined below [9, 10].

1. Energy Transfer

In presence of a molecule of a lower energy excited state (acceptor), the excited donor (D^*) can be deactivated by a process known as energy transfer which can be represented by the following sequence of equations.



For energy transfer to occur, the energy level of the excited state of D^* has to be higher than that for A^* and the time scale of the energy transfer process must be faster than the lifetime of D^* . Two possible types of energy transfers are known—namely, radiative and nonradiative (radiationless) energy transfer. Radiative

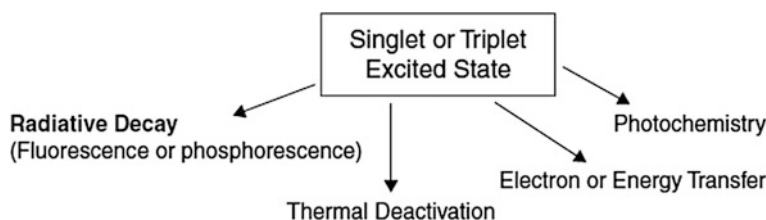


Fig. 2.10 Different pathways for the reactivation of the excited state

transfer occurs when the extra energy of D^* is emitted in form of luminescence and this radiation is absorbed by the acceptor (A).

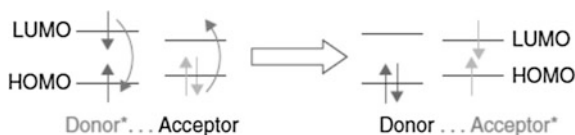


For this to be effective, the wavelengths where the D^* emits need to overlap with those where A absorbs. This type of interaction operates even when the distance between the donor and acceptor is large (100 Å). However, this radiative process is inefficient because luminescence is a three-dimensional process in which only a small fraction of the emitted light can be captured by the acceptor. The second type, radiationless energy transfer, is more efficient. There are two different mechanisms used to describe this type of energy transfer: the Förster and Dexter mechanisms.

The energy transfer action is according to Förster mechanism. The Förster mechanism is also known as the coulombic mechanism or dipole-induced dipole interaction. It was first observed by Förster. Here, the emission band of one molecule (donor) overlaps with the absorption band of another molecule (acceptor). In this case, a rapid energy transfer may occur without a photon emission. This mechanism involves the migration of energy by the resonant coupling of electrical dipoles from an excited molecule (donor) to an acceptor molecule. Based on the nature of interactions present between the donor and the acceptor, this process can occur over a long distances (30–100 Å). The mechanism of the energy transfer by this mechanism is illustrated in Fig. 2.11. In Fig. 2.11, an electron of the excited donor placed in the LUMO relaxes to the HOMO, and the released energy is transferred to the acceptor via coulombic interactions. As a result, an electron initially in the HOMO of the acceptor is promoted to the LUMO. This mechanism operates only in singlet states of the donor and the acceptor. This can be explained on the basis of the nature of the interactions (dipole–induced dipole) because only multiplicity conserving transitions possess large dipole moments. This can be understood considering the nature of the excited state in both the singlet and the triplet states. The triplet state has a diradical structure, so it is less polar, making it difficult to interact over long distances (i.e., Förster mechanism). The rate of energy transfer (k_{ET}) according to this mechanism can be evaluated by the Eq. (2.32):

$$k_{ET} = k_D R_F^6 \left(\frac{1}{R} \right)^6 \quad (2.32)$$

Fig. 2.11 Mechanism of energy transfer action according to Förster



where k_D is the emission rate constant for the donor, R is the interchromophore separation, and R_F is the Förster radius, which can be defined as the distance between the donor and the acceptor at which 50 % of the excited state decays by energy transfer—that is, the distance at which the energy transfer has the same rate constant as the excited state decay by the radiative and nonradiative channels ($k_{ET} = k_r + k_{nr}$). R_F is calculated by the overlap of the emission spectrum of the donor excited state (D^*) and the absorption spectrum of the acceptor (A).

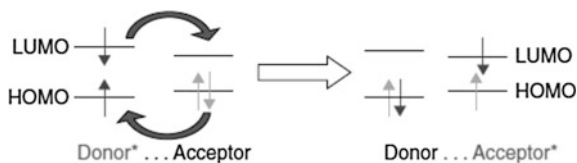
The energy transfer action is according to the Dexter mechanism also. The Dexter mechanism is a nonradiative energy transfer process that involves a double electron exchange between the donor and the acceptor (Fig. 2.12). Although the double electron exchange is involved in this mechanism, no charge-separated state is formed.

The Dexter mechanism can be thought of as electron tunneling, by which one electron from the donor's LUMO moves to the acceptor's LUMO at the same time as an electron from the acceptor's HOMO moves to the donor's HOMO. In this mechanism, both singlet–singlet and triplet–triplet energy transfers are possible. This contrasts with the Förster mechanism, which operates in only singlet states. For this double electron exchange process to operate, there should be a molecular orbital overlap between the excited donor and the acceptor molecular orbital. For a bimolecular process, intermolecular collisions are required as well. This mechanism involves short-range interactions that is about 6–20 Å or shorter. Because it relies on tunneling, it is attenuated exponentially with the intermolecular distance between the donor and the acceptor. The rate constant can be expressed by the following:

$$k_{ET} = \frac{2\pi}{\hbar} V_0^2 J_D \exp\left(-\frac{2R_{DA}}{L}\right) \quad (2.33)$$

where R_{DA} is distance between the donor and the acceptor, J_D is the integral spectral overlap between the donor and the acceptor, L is the effective Bohr radius of the orbitals between which the electron is transferred, \hbar is Plank's constant, and V_0 is the electronic coupling matrix element between the donor and acceptor at the contact distance. Comparing the two energy transfer mechanisms, the Förster mechanism involves only dipole–dipole interactions, and the Dexter mechanism operates through electron tunneling. Another difference is their range of interactions. The Förster mechanism involves longer range interactions (up to ~ 30 – 100 Å), but the Dexter mechanism focuses on shorter range interactions that is from 6 Å up to 20 Å because orbital overlap is necessary. Furthermore, the Förster

Fig. 2.12 Mechanism of energy transfer action according to the Dexter mechanism



mechanism is used to describe interactions between singlet states, but the Dexter mechanism can be used for both singlet–singlet and triplet–triplet interactions. Hence for the singlet–singlet energy transfer, both mechanisms are possible.

Simulated graphs using reasonable values for the parameters for the two mechanisms have been constructed for the purpose of distinguishing between the zones where Förster and Dexter mechanisms are dominant. The experimental values of the energy transfer rates in cofacial bisporphyrin systems were found to agree with the theoretically constructed graphs (see Fig. 2.13). In these graphs a Bohr radius value (L) of 4.8 Å (the value for porphyrin) is used in the Dexter equation. Also, the solid lines correspond to hypothetical situations in which only the Förster mechanism operates; the dotted lines are hypothetical situations for when the Dexter mechanism is the only process. The curved lines are simulated lines obtained with Eq. (2.32) (Förster) or Eq. (2.33) (Dexter) but transposed onto the other graph, i.e., Förster equation plotted against Dexter formulation and vice versa. These plots clearly suggest the presence of a crossing point between the two mechanisms. There is a zone in which one mechanism is dominant and vice versa. All in all, the relaxation of an excited molecule via energy transfer processes will use all the pathways available to it so the total rate for energy transfer can be better described as k_{ET} (total) $\approx k_{ET}$ (Förster) + k_{ET} (Dexter). According to Fig. 2.13, the distance at which there is a change in dominant mechanism is about 5 Å.

2. Electron Transfer

Photoinduced electron transfer (PET) involves an electron transfer within an electron donor–acceptor pair. The situation is represented in Fig. 2.14. PET represents one of the most basic photochemical reactions and at the same time it is the

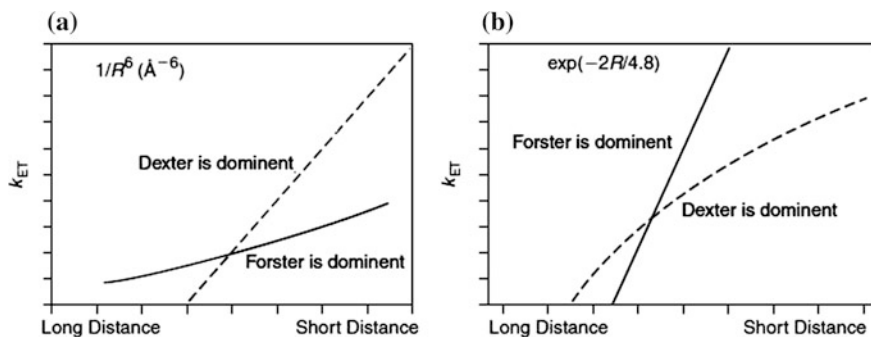


Fig. 2.13 Qualitative theoretical plots for **a** k_{ET} versus $1/R^6$ (Förster) and **b** k_{ET} versus $\exp(-2R/4.8)$

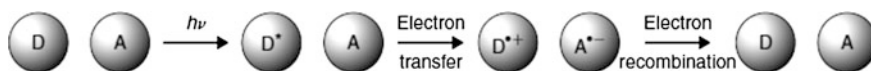
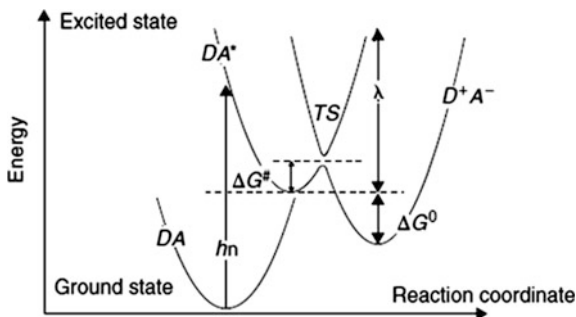


Fig. 2.14 Photoinduced electron transfer process

Fig. 2.15 Potential energy surfaces for the ground state (DA), the excited state (DA^* —reactant state), and the charge-separated state (D^+A^- —product state), by Marcus's theory. λ —total reorganization energy, TS —transition state



most attractive way to convert light energy or to store it for further applications. In Fig. 2.14, one can see a process taking place between a donor and acceptor after excitation, resulting in the formation of a charge-separated state, which relaxes to the ground state via an electron-hole recombination (back electron transfer).

A theory used to study and interpret the PET in solution was described by Marcus. In this theory, the electron transfer reaction can be treated by transition state theory where the reactant state is the excited donor and acceptor and the product state is the charge-separated state of the donor and acceptor (D^+A^-), shown in Fig. 2.15. According to the Franck–Condon principle, the photoexcitation triggers a vertical transition to the excited state, which is followed by a rapid nuclear equilibration. Without donor excitation, the electron transfer process would be highly endothermic. However, after exciting the donor, electron transfer occurs at the crossing of the equilibrated excited state surface and the product state. The change in Gibbs free energy associated with the electron transfer event is given by the following relation as:

$$\Delta G^\# = \frac{(\lambda + \Delta G^0)^2}{4\lambda} \quad (2.34)$$

The total reorganization energy (λ), which is required to distort the reactant structure to the product structure without electron transfer, is composed of solvent (λ_s) and internal (λ_i) components ($\lambda = \lambda_i + \lambda_s$). The reaction free energy (ΔG^0), is the difference in free energy between the equilibrium configuration of the reactant (DA^*) and of the product states (D^+A^-). The internal reorganization energy represents the energy change that occurs in bond length and bond angle distortions during the electron transfer step and is usually represented by a sum of harmonic potential energies. In the classical Marcus theory, the electron transfer rate is given by equation

$$k_{ET} = \kappa_{ET} \nu_n \exp\left(\frac{-\Delta G^\#}{k_B T}\right) \quad (2.35)$$

where ν_n is the effective frequency of motion along the reaction coordinate and κ_{ET} is the electronic transmission factor. The transmission factor is related to the transition probability (P_0) at the intersection of two potential energy surfaces, as given by the Landau–Zener theory.

$$\kappa_{\text{ET}} = \frac{2P_0}{1 + P_0} \quad (2.36)$$

A graph showing the change of the driving force for the electron transfer rate, calculated from Marcus theory, versus the rate constant is given in Fig. 2.16 (bottom). Using Eq. (2.35) to estimate the electron transfer rate, we can assign the Marcus normal region as that where the free reaction energy (ΔG^0) is decreased, leading to an increase of the electron transfer rate (k_{ET}). The second region that can be identified in Fig. 2.16 is the optimal or activationless region, where the driving force for electron transfer equals the reorganization energy—that is, $-\Delta G^0 = \lambda$. If ΔG^0 becomes even more negative, the activation barrier ΔG^\ddagger reappears, resulting in a decrease in the values of k_{ET} . This last situation is observed over the region known as the inverted Marcus region and was first experimentally demonstrated by Closs and Miller. The potential energy illustrating the different Marcus regimes can be seen in Fig. 2.16 (top).

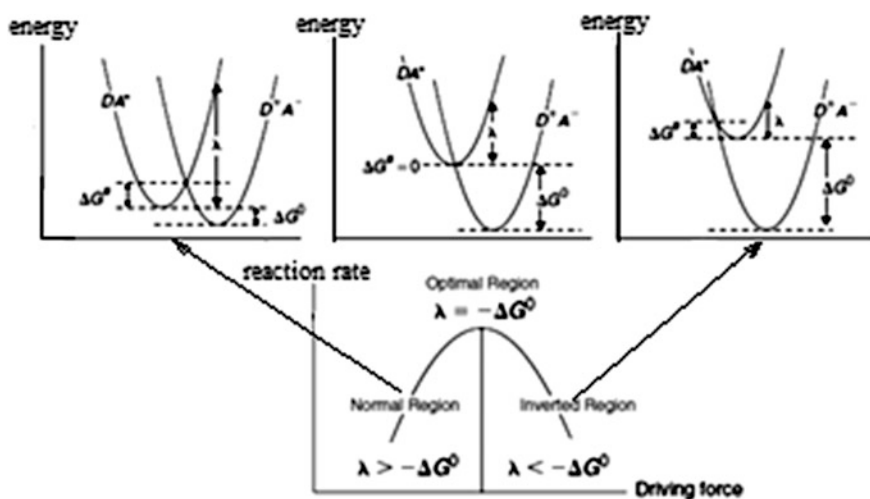


Fig. 2.16 The free energy regimes for electron transfer (top) and the corresponding reaction rate dependence on the free energy (bottom, driving force is $\Delta G^0 - \lambda$)

2.3 Other Actions of Photon to Materials

2.3.1 *Nonlinear Optical Action*

Nonlinear optics (NLO) involves the interaction of light with materials resulting in a change in the frequency, phase, or other characteristics of the light. There are a variety of frequency-mixing processes. Second-order NLO behavior includes second harmonic generation of light that involves the frequency doubling of the incident light. Frequency mixing where the frequency of two light beams are either added or subtracted. Electrooptic effects can occur where both frequency and amplitude changes and where rotation of polarization occurs. NOL behavior has been found in inorganic and organic compounds and in polymers. The structural requirement is the absence of an inversion center requiring the presence of asymmetric centers and/or poling. Poling is the application of a high voltage field to a material that orients some or all of the molecule dipoles generally in the direction of the field. The most effective poling in polymers is found when they are poled above the T_g (which allows a better movement of chain segments) and then cooled to lock in the poled structure. Similar results are found for polymers that contain side chains that are easily poled. Again, cooling helps lock in the poled structure. At times, cross-linking is also employed to help lock in the poled structure. Third-order NLO behavior generally involves three photons, resulting in effects similar to those obtained for second-order NLO behavior. Third-order NLO behavior does not require the presence of asymmetric structures. Polymers that have been already been found to offer NLO behavior include polydiacetylenes and a number of polymers with liquid crystal side chains. Polymers are also employed as carriers of materials that themselves are NLO materials. Applications include communication devices, routing components, and optical switches [11–13].

2.3.2 *Photoconductive and Photonic Polymers*

Some polymeric materials become electrically conductive when illuminated with light. For instance, poly (*N*-vinylcarbazole) is an insulator in the dark, but when exposed to UV radiation it becomes conductive as shown in Fig. 2.17a. The addition of electron acceptors and sensitizing dyes allows the photoconductive response to be extended into the visible and NIR regions. In general, such photoconductivity depends on the materials ability to create free-charge carriers, electron holes, through absorption of light, and to move these carriers when a current is applied.

Related to this are materials whose response to applied light varies according to the intensity of the applied light. This is nonlinear behavior. In general, polymers with whole-chain delocalization or large-area delocalization in which electrons are optically excited may exhibit such nonlinear optical behavior.

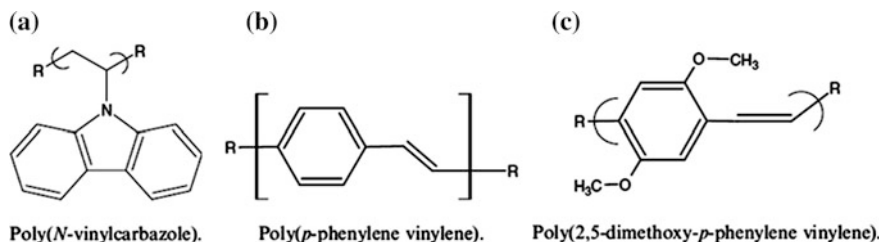


Fig. 2.17 Molecular configuration of poly (*N*-vinylcarbazole) photonic polymers

A photoresponsive sunglass whose color or tint varies with the intensity of the sunlight is an example of nonlinear optical material. Some of the so-called smart windows are also composed of polymeric materials whose tint varies according to the incident light. Currently, information is stored using electronic means but optical storage is becoming common place with the use of CD-ROM and WORM devices. Such storage has the advantages of rapid retrieval and increased knowledge density (i.e., more information stored in a smaller space).

Since the discovery of doped polyacetylene, a range of polymeric semiconductor devices has been studied, including normal transistors, field-effect transistors (FETs) photodiodes, and light-emitting diodes (LEDs). Like conductive polymers, these materials obtain their properties from their electronic nature, specifically the presence of conjugated π -bonding systems. In electrochemical light-emitting cells, the semiconductive polymer can be surrounded asymmetrically with a hole-injecting material on one side and a low work function electron injecting metal (such as magnesium, calcium, or aluminum) on the other side. The emission of light may occur when a charge carrier recombines in the polymer as electrons from one side and holes from the other meet.

Poly(*p*-phenylene vinylene) (PPV) was the first reported in 1990 that polymer to exhibit electroluminescence. PPV is employed as a semiconductor layer. The layer was sandwiched between a hole-injecting electrode and electron injecting metal on the other. PPV has an energy gap of about 2.5 eV and thus produces a yellow-green luminescence when the holes and electron recombine. Today, many other materials are available that give a variety of colors as in Fig. 2.17b.

A number of poly (arylene vinylene) (PAV) derivatives have been prepared. The electron-donating substituents, such as two methoxy groups, act to stabilize the doped cationic form and thus lower the ionization potential. These polymers exhibit both solvatochromism (color change as solvent is changed) and thermochromism (color is temperature dependent) as in Fig. 2.17c. The introduction of metals into polymers that can exhibit entire chain electron delocalization is at the basis of much that is presented in this volume. These metal-containing sites are referred to as chromophores, and the combination of metal chromophores exhibiting metal to ligand charge transfer (MLCT) excited states opens new possibilities for variation of electronic and optical properties needed for the continual advancement in electronics and electronic applications. Application areas include light-emitting

polymeric diodes, solar energy conversion and nonlinear optical materials (NLOs) and materials exhibiting photorefraction, electrochromism and electrocatalysis as shown in Fig. 2.17.

One of the major reasons for interest in this area is the ease with which the new hybrid materials' properties can be varied by changing the metal, metal oxidation state, metal matrix, and polymer. Multiple metal sites are readily available. This allows the metal-containing system to have a high degree of tunability. This is due to the often strong electronic interaction between the metal and the delocalized electron systems. The already noted variety of available metal sites is further leveraged by the increasingly capability of modern synthetic methodologies to achieve the desired structures. But the presence of metal atoms is at the heart of this.

2.3.3 *Photosynthesis*

The recent environmental issues related to the greenhouse effect and atmospheric contamination heightens the importance of obtaining energy from clean sources, such as photosynthesis. Photosynthesis also acts as a model for the creation of synthetic light-harvesting systems that might mimic chlorophyll in its ability to convert sunlight into usable energy. The basis of natural photosynthesis was discovered by Melvin Calvin. Using carbon-14 as a tracer, Calvin and his team found the pathway that carbon follows in a plant during photosynthesis. They showed that sunlight supplies the energy through the chlorophyll site, allowing the synthesis of carbon-containing units, mainly saccharides or carbohydrates. Chlorophyll is a metal embedded in a protein polymer matrix and illustrates the importance of metals in the field of photochemistry and photophysics. A brief description of the activity of chlorophyll in creating energy from the sun follows. The maximum solar power density reaching Earth is approximately 1350 W/m^2 . When this energy enters the Earth's atmosphere, the magnitude reaching the surface drops approximately to 1000 W/m^2 owing to atmospheric absorption. The amount that is used by plants in photosynthesis is about seven times the total energy used by all humans at any given time, thus it is a huge energy source. Solar energy is clean and economical energy, but it must be converted into useful forms of energy. For example, solar energy can be used as a source of excitation to induce a variety of chemical reactions. Natural examples for conversion of light energy are plants, algae, and photosynthetic bacteria that used light to synthesize organic sugar-type compounds through photosynthesis. In photosynthesis, green plants and some bacteria harvest the light coming from the sun by means of their photosynthetic antenna systems. The light harvesting starts with light gathering by antenna systems are consist of pigment molecules, including chlorophylls, carotenoids, and their derivatives. The absorbed photons are used to generate excitons, which travel via Förster energy transfers towards the reaction centers (RCs). This overall series of processes is represented in Fig. 2.18.

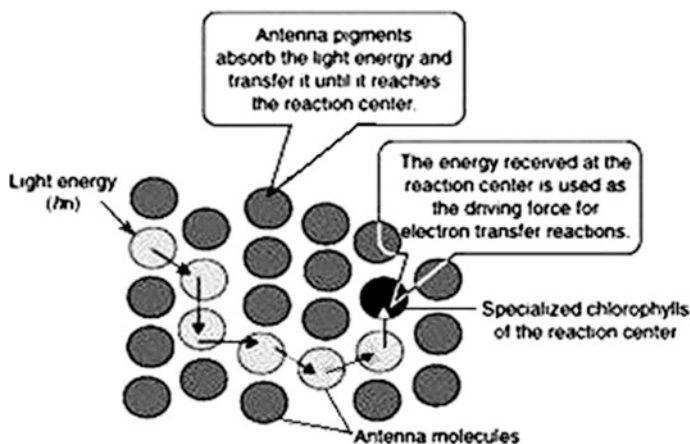


Fig. 2.18 Light is absorbed by the antenna, and the energy is transferred to the RC, where charge separation takes place to generate chemical energy

In RCs, this energy drives an electron transfer reaction, which in turn initiates a series of slower chemical reactions. Energy is saved as redox energy, inducing a charge separation in a chlorophyll dimer called the special pair (chlorophyll). Charge separation, which forms the basis for photosynthetic energy transfer, is achieved inside these RCs Eqs. (2.37), (2.38).



Specialized reaction center (RC) proteins are the final destination for the transferred energy. Here, it is converted into chemical energy through electron transfer reactions. These proteins consist of a mixture of polypeptides, chlorophylls (plus the special pair), and other redox-active cofactors. In the RCs, a series of downhill electron transfers occur, resulting in the formation of a charge-separated state. Based on the nature of the electron acceptors, two types of RCs can be described. The first type (photosystem I) contains iron-sulfur clusters (Fe_4S_4) as their electron acceptors and relays, whereas the second type (photosystem II) features quinones as their electron acceptors.

Both types of RCs are present in plants, algae, and cyanobacteria, whereas the purple photosynthetic bacteria contain only photosystem II and the green sulfur bacteria contain a photosystem I. To gain a better understanding of these two types of RCs each will be further discussed.

2.3.4 Purple Photosynthetic

1980s later, Deisenhofer reported his model for the structure of photosystem II for two species of purple photosynthetic bacteria (*Rhodospseudomonas viridis* and *Rhodobacter*) based on X-ray crystallography of the light-harvesting device II (LH II). Photosynthetic centers in purple bacteria are similar but not identical models for green plants. Because they are simpler and better understood, they will be described here. The photosynthetic membrane of purple photosynthetic bacteria is composed of many phospholipid-filled ring systems (LH II) and several larger dissymmetric rings (LH I) stacked almost like a honeycomb. Inside the LH I is a protein called the RC. The LH II complex antenna is composed of two bacteriochlorophyll a (BChl) molecules, which can be classified into two categories. The first one is a set of 18 molecules arranged in a slipped face-to-face arrangement and is located close to the membrane surface perpendicularly to these molecules. The second ring is composed of BChl in the middle of the bilayer. The first BChl have an absorption maximum at 850 nm and are collectively called B850, while the second (9 BChl) have an absorption maximum at 800 nm and are called B800. These structures are contained within the walls of protein cylinders with radii of 1.8 and 3.4 nm. Once the LH II complex antenna absorbs light, a series of very complex nonradiative photophysical processes are triggered.

First, the excitation energy migrates via energy transfers involving the hopping of excitation energy within almost isoenergetic subunits of a single complex. This is followed by a fast energy transfer to a lower energy complex with minimal losses (see Fig. 2.19). These ultrafast events occur in the singlet state (S_1) of the BChl pigments and are believed to occur by a Förster mechanism. The energy collected by the LH II antenna is transferred to another antenna complex known as LH I, which surrounds the RC. The photosynthetic RCs of bacteria consist mainly of a protein that is embedded in and spans a lipid bilayer membrane. In the RC, a series of electron transfer reactions are driven by the captured solar energy. These electron transfer reactions convert the captured solar energy to chemical energy in Fig. 2.19. Two light-harvesting II (LH II) units is next to one light-harvesting I (LH I) unit. Gray circles, polypeptides, bars, rings of interacting bacteriochlorophylls a (called B850). In the middle of LH I, there is the RC, where the primary PET takes place

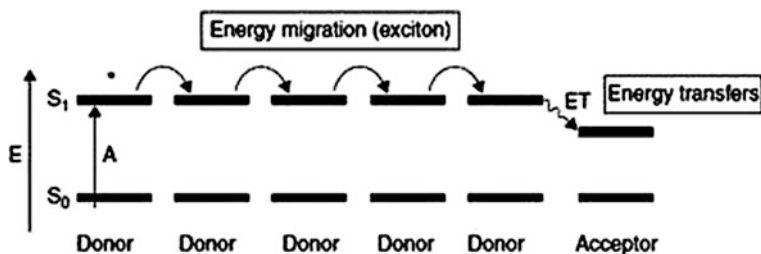


Fig. 2.19 The exciton and energy transfer processes

from the special pair of bacteriochlorophylls. Introduction to Photophysics and Photochemistry formed a charge separation process across the bilayer. The mechanism of this process is illustrated in Fig. 2.20. A special BCHI (P870) pair is excited either by the absorption of a photon or by acquiring this excitation energy from an energy transfer from the peripheral antenna BCHI (not shown in the figure for simplicity), triggering a photoinduced electron transfer inside the RC. Two photoinduced electrons are transferred to a plastoquinone located inside the photosynthesis membrane. This plastoquinone acts as an electron acceptor and is consequently reduced to a semiquinone and finally to a hydroquinone. This reduction involves the uptake of two protons from water on the internal cytoplasmic side of the membrane. This hydroquinone then diffuses to the next component of the apparatus, a proton pump called the cytochrome bc1 complex as in Fig. 2.20.

The oxidation of the hydroquinone back to a quinone and the energy released is used for the translocation of the protons across the membrane. This establishes a proton concentration and charge imbalance (proton motive force, pmf). Thus, the oxidation process takes place via a series of redox reactions triggered by the oxidized special pair BCHI, which at the end is reduced to its initial state. The oxidation process is ultimately driven, via various cytochrome redox relays, by the oxidized P870. Oxidized P870 becomes reduced to its initial state in this sequence. Finally, the enzyme ATP synthase allows protons to flow back down across the membrane driven by the thermodynamic gradient, leading to the release of ATP formed from adenosine diphosphate and inorganic phosphate (P_i).

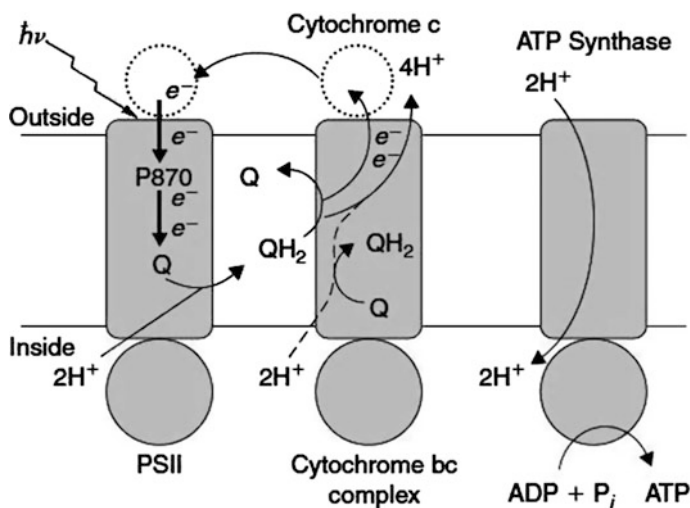


Fig. 2.20 A cross-section of the photosynthetic membrane in the purple photosynthetic bacteria. PS II-photosystem II; P870-special pair; Q-plastoquinone; QH_2 -dihydroplastoquinone; ADP-adenosine diphosphate; ATP-adenosine triphosphate

2.4 Photophysical Properties of Organometallic Polymers

Organic and organometallic polymers exhibit potential applications in photonics. Organometallic polymers have received a lot of interest because they could combine the advantages of the high luminescence of the organic moiety with the high carrier density, mobility, steady chemical properties, and physical strength of inorganic materials. Research on such materials is expanding because of their potential use as electric components, such as FETs, LEDs, and solar cells.

Much effort involving solar energy conversion is based on the natural chlorophyll system as a model. Here, a metal atom is embedded within a polymer matrix that exhibits high electron mobility (delocalization). Ruthenium, platinum, and palladium are the most employed metals. The use of materials containing the bis (2,2-bipyridine)ruthenium II moiety is common with ruthenium because this moiety absorbs energy in the UV region and emits it at energies approximating those needed to cleave water molecule bonds. The use of solar energy to create hydrogen that is harvested and later converted to useful energy has been a major objective. Here, we focus on a more direct conversion of solar energy into energy to charge batteries. For this purpose, metal-containing polymers can be classified into three types (types I, II, and III), as illustrated in Fig. 2.21. In type I, the metal centers are connected to the conjugated polymer backbone through saturated linkers, such as alkyl chains. Polymers of type I act as a conducting support. The electronic, optical, and chemical properties of the metal ions in this type of polymer remain the same as they would be if they were alone (i.e., unattached to the polymer backbone).

In the second type, the metal centers are electronically coupled to the conjugated polymer backbone. This affects both the polymer and the metal group properties. The metal centers for type III are located directly within the conjugated backbone. In this last type, there are strong interactions between the metal center and the organic bridge. For this arrangement, the electronic interactions between the organic bridge and the metal group are possible, and new properties can be obtained because of the combination of the characteristics of the organic polymers with the common properties of the transition metals. Heavy metal atoms in the polymer backbone increase the intersystem crossing rate of the organic lumophores due to enhanced spin-orbit coupling. This populates more of the triplet states facilitating the study of interactions on both singlet and triplet states. The study of energy

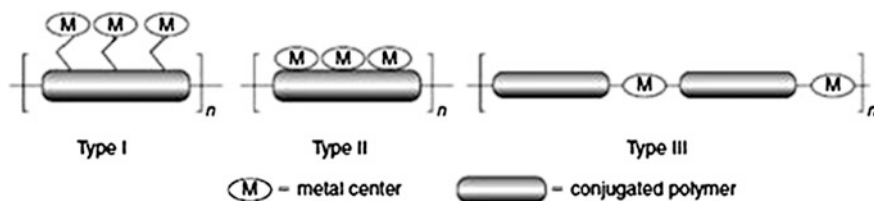


Fig. 2.21 Types of metal-containing polymers

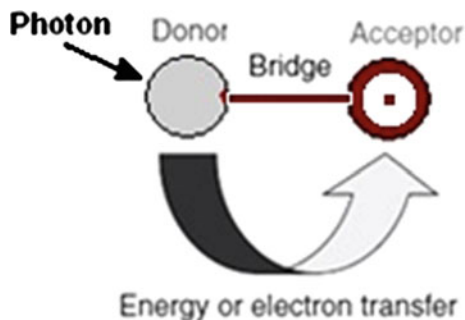
transfer in organic and organometallic polymers is important. In fact, various types of organic and organometallic systems (oligomers and polymers) have been specifically designed for intramolecular energy transfer studies. Molecular architecture was found to play an important role in the efficiency of the energy transfer. The bridge between the donor and the acceptor chromophores exerts an important effect on the rates as well as the mechanism through which the energy transfer occurs. A through-bond mechanism operates very efficiently for the cases of rigid saturated hydrocarbon bridges, while through-space mechanism is efficient for flexible bridges.

The photophysical properties of macromolecules built on M-P and M-CN (isocyanide) bonds, including the metal in the backbone (The presence of the metal atom associated with the porphyrin moiety is examined here). Photosynthesis is a source of inspiration for scientists interested in nonnatural systems that convert light into chemical potential or electrical energy. Molecular wires, optoelectronic gates, switches, and rectifiers are typical examples of molecular electronic devices envisioned for use in energy or electron transfer processes. A basic device structure, stimulating the natural systems, needs a scaffold on which the energy or charge transfer can be induced. Such a scaffold is represented in Fig. 2.22. The approach for this system is the mimicry of the highly efficient photosynthesis process in biological systems, by which an antenna device collects the light energy that the energy and electron transfers lead to the synthesis of the plant's fuel. Porphyrins are an interesting class of compounds used for the study of energy- and electron transfer functions of the natural photosynthetic machinery.

The interest in porphyrins is motivated in part by their photocatalytic activity and electronic properties. Porphyrins are also structurally related to chlorophyll. Cofacial bisporphyrin systems use rigid spacers to provide a unique placement of two chromophores (donor and acceptor) at a given distance, inducing a through-space energy transfer as the shortest pathway for intermolecular interactions and communications.

Recently, the effect of the donor–acceptor separation has been studied. Both the fluorescence lifetime and quantum yield were found to decrease as the distance between the two porphyrins $C_{\text{meso}}-C_{\text{meso}}$ (cd) and $CC_{\text{meso}}-CC_{\text{meso}}$ (ab) decreases (Fig. 2.23). As the two rings get closer to each other, they interact more strongly,

Fig. 2.22 A scaffold for photoinduced intramolecular energy or electron transfer



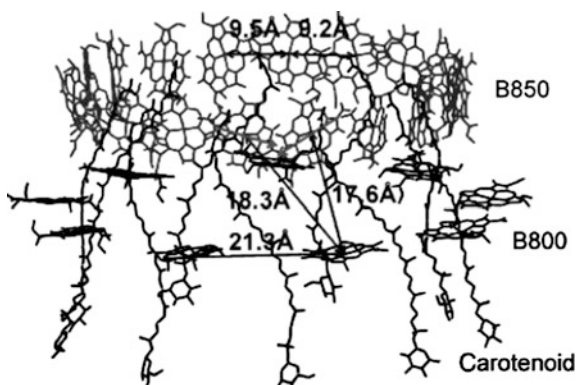
and hence nonradiative deactivation becomes more pronounced. The rate dependence for the S_1 energy transfer (S_1 ET) for such systems exhibits a dependence of the energy transfer (k_{ET}) rate on the $C_{meso}-C_{meso}$ distance. The rate increases as the distance decreases. Face-to-face donor–acceptor separations are on the order of ~ 3.5 Å versus the corresponding various donor–acceptor separations in the living supramolecular structures (found in plants, algae, and cyanobacteria) (Figs. 2.23 and 2.24) which are found to have separation distances to ~ 20 Å. Despite this observation, the S_1 energy transfer data are strikingly slower (two orders of magnitude). Both through-space and through-bond energy transfer mechanisms are known, by which singlet–singlet energy transfer occurs through both Coulombic or dipole–dipole interaction (Förster) and double electron exchange (Dexter) mechanisms.

Different donor-bridge-acceptor based dyads based on metallated and free base porphyrins, by which singlet–singlet energy transfer occurs through both Förster and Dexter mechanisms are given in Fig. 2.25. The S_1 energy transfer in these systems occurs via a contribution from both coulombic and double electron exchange that have almost the same magnitude and are not affected by the donor and acceptor distances. The electronic interactions depend on the donor-bridge energy gap and the bridge conformation (planar or nonplanar). Studies of the



Fig. 2.23 Examples of cofacial face-to-face porphyrin systems with different spacers

Fig. 2.24 A LH II ring showing only the chlorophyll for the B850 network, the noninteracting B800 bacteriochlorophylls and the rhodopin glucosides. Two of the B850 units are marked with arrows, representing the transition moments



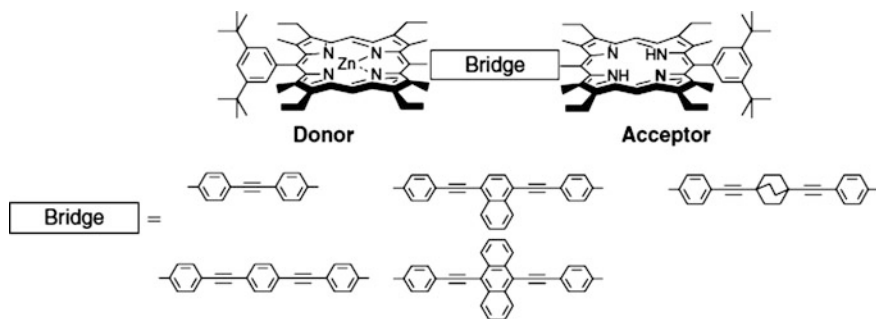
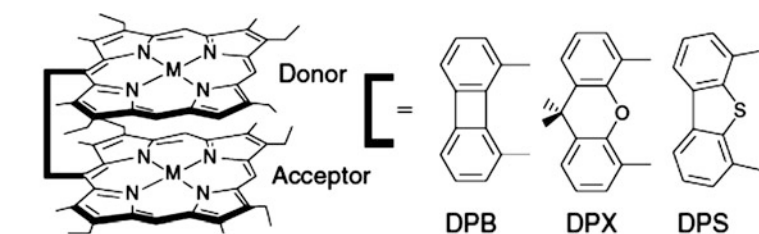


Fig. 2.25 Some donor-bridge-acceptor systems by which energy transfer occurs through both Förster and Dexter mechanisms



Spacer	DPB	DPB	DPB	DPX	DPX	DPX	DPX	DPS	DPS
M	Pt	2H	2H	Pt	2H	2H	Zn	2H	Zn
M'	Pt	Pt	Pd	Pt	Pt	Pd	Pd	Pd	Pd

Fig. 2.26 Examples of cofacial bisporphyrin systems containing heavy atoms

energy transfer rate as a function of the energy gap between the donor and the bridge have facilitated the separation of the two mechanisms. The rates observed for systems with the biggest energy gap were found to be almost equal to the Förster energy transfer rates [14, 15].

Harvey's group studied energy transfers arising from the longer-lived triplet states as well as from the singlet states. These studies involved porphyrins containing a heavy metal (e.g., Pt and Pd), as shown in Fig. 7.27. Spin-orbit coupling of the heavy atom increased the intersystem crossing rates, thus increasing the population of the triplet excited state. Triplet energy transfers can be analyzed only according to the Dexter mechanism because the Förster mechanism does not operate in the triplet excited states due to their diradical nature and the multiplicity change during the process. Energy transfer for the Dexter mechanism occurs via a

double electron exchange—HOMO (acceptor)-HOMO (donor) and LUMO (donor)-LUMO (acceptor)—between triplet states of the donor and acceptor. In these systems (as in Fig. 2.26), the Pd- and Pt-metallated chromophores act as triplet donors, whereas the free base and Zn-containing complexes are the energy acceptors.

Analyses of energy transfer rates revealed that no sensitive transfer was detected for systems in which the spacer was DPS. In contrast, for dyads with the DPB and DPX spacers containing dyads, energy transfer occurred. This result was explained on the basis that singlet states energy transfer occurs via both Förster and Dexter mechanisms in the DPB- and DPX-containing dyads: $C_{\text{meso}}-C_{\text{meso}} = 3.80$ and 4.32 \AA , respectively. The singlet energy transfer mechanism proceeded predominantly via a Dexter mechanism. Conversely, singlet energy transfer in the DPS-containing dyad, $C_{\text{meso}}-C_{\text{meso}} = 6.33 \text{ \AA}$, operated predominantly according to the Förster mechanism. This latter mechanism is inactive in the triplet states. Thus, at such long distances, orbital overlap is poor and energy transfer is either weak or nil. This concept is of importance for designing molecular switches based on the distance separating the donor from the acceptor. Through-bond energy transfer was also observed for porphyrin systems (regardless whether it occurs via a Förster or a Dexter mechanism). Through-bond energy transfer was reported for the rhodium meso-tetraphenylporphyrin-tin, which exhibits a Rh-Sn bond length of 2.5069 \AA and a 3.4 \AA separation between the average macrocycle planes, as in Fig. 2.27.

A photophysical study of these porphyrin systems showed the presence of significant intramolecular triplet energy transfer with an estimated k_{ET} ranging between 10^6 and 10^8 s^{-1} . Rates for the through-bond process were found to be three to five orders of magnitude larger than the through-space energy transfer. Other examples for through-bond energy transfer are shown in Fig. 2.28. The intramolecular energy transfer rates within these systems were found to be slower than those estimated for cofacial systems by two or three orders of magnitude. These results can be helpful in predicting the rates for energy transfer (k_{ET}) for unknown systems.

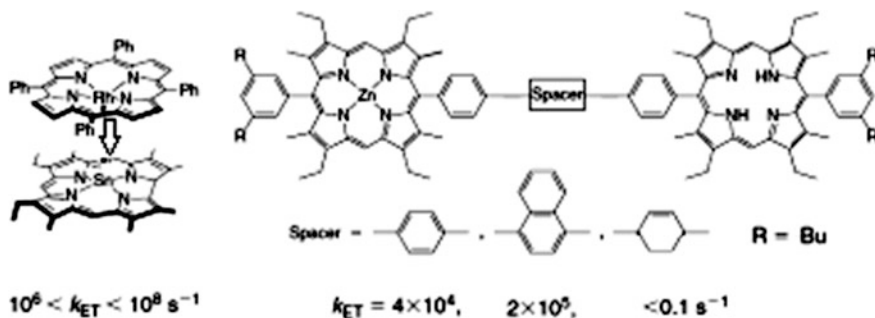


Fig. 2.27 Porphyrin systems with through-bond energy transfer

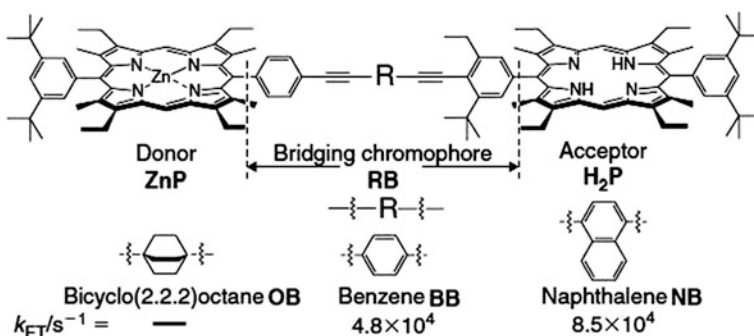


Fig. 2.28 Porphyrin systems with through-bond energy transfer

A similar observation was made by Albinson, using Zn(II) porphyrin as the donor and free base porphyrin as the acceptor. The solvent viscosity and temperature were investigated as factors affecting the donor–acceptor interactions (Fig. 2.28). In this example, and in agreement with Fig. 2.27, the rate increased with an increase of conjugation. Conversely, energy transfer is completely turned off when the conjugation is broken by the presence of the saturated system. This indicates that the through-bond energy transfer process occurs from the higher energy triplet state of Zn(II) porphyrin to the lower lying triplet state of the free base porphyrin. The triplet energy transfer rates were measured over temperatures from 295 to 280 K. The free energies of activation were found to be in the range of 1.0–1.7 kcal/mol (about 4–8 kJ/mol) in low-viscosity solvents, whereas in high-viscosity solvents, the temperature dependence is less pronounced. The triplet energy transfer was dependent on the solvent viscosity. Dramatically slower rates are observed in high-viscosity solvents due to smaller electronic coupling. The triplet excited donor porphyrin was suggested to adopt conformation in less viscous solutions, which have a much larger electronic coupling than is possible in highly viscous media. The porphyrins considered in the study are prone to conformational change in the triplet manifold. This was explained on conformational grounds.

In a donor-spacer-acceptor system (Fig. 2.28), with the ground state exhibiting a dihedral angle near 90°, the electronic coupling is changed in the triplet state to a situation in which the phenyl group should rotate towards the plane of the porphyrin macrocycle, leading to a considerable increase in the electronic coupling. This conformational freedom is lost when the solvent rigidifies, leading to a decrease in the coupling between the donor and the bridge. In solvents of low viscosity, another observation was made. Indeed, the change in temperature led to a triplet state distortion, inducing slower rates for triplet energy transfers.

All in all, the nature of the donor–acceptor linker is undoubtedly a controlling factor for the energy transfer, especially in the case of the triplet state interactions in which the mechanism of the interaction proceeds according to the Dexter mechanism (i.e., double electron exchange). This analysis illustrates the importance of studying different donor–acceptor spacers and their geometries during

photoinduced energy transfer. Interest in the electronic properties of π -conjugated oligomers and polymers and polymers containing metal atoms continues to increase greatly. The metal site can offer chromophores that exhibit MLCT excited states in the π -conjugated polymers systems. This allows a variety of electronic and optical properties that are finding application in numerous areas, including solar energy conversion devices, NLOs, and polymer light-emitting diodes (PLEDs), with applications in physical and chemical sensing, electrochromism, and a wide scope of electrocatalysis.

The presence of the metal allows the synthesis of a wide variety of materials, with a variety of optical, electronic, chemical, and physical characteristics. The particular properties are changed and tuned by varying the metal, metal oxidation state, and metal environment. This volume describes some of these materials and applications for metal-containing sites embedded within polymer matrices and it suggests others.

2.5 Inorganic Photochemistry and Photocatalysis

Inorganic photochemistry and photocatalysis is one of important elements for multidimensional optical storage that offers some conceptions to investigate and develop new medium based on photoelectrochemistry and photocatalysis [16, 17].

2.5.1 *Electron Storage on ZnO Particles*

Zinc oxide is a semiconductor which has often been applied in photoelectrochemistry and photocatalysis. Small ZnO particles show typical size quantization effect, the onset of light absorption and position of the fluorescence band being shifted to shorter wavelengths with decreasing particle size. This effect has now been investigated in more detail to obtain the relationship between particle size and the wavelength of the absorption threshold.

The research in field of colloidal semiconductor nanocrystals has clarified and revealed new concepts and mechanisms in photophysics, electronic structure, magnetism, interfacial chemistry, redox chemistry, charge transport, crystal nucleation and growth, and self-assembly, and has introduced new approaches to energy harvesting and conversion, electronics, catalysis, chemical sensing, and imaging. The quantum dot field is growing rapidly and in many different directions. This new GRC to push forward research in this complex interdisciplinary field and will bring together making exciting contributions in both fundamental and applied research within the field of colloidal nanocrystals.

A improved methods for the preparation of colloidal ZnO solutions of different particle size are described, and the relation between absorption threshold and particle size is reported. CH_2OH radicals radiolytically generated transfer electrons

to ZnO particles. The electrons are long-lived and cause a substantial blue shift of the absorption spectrum of ZnO in a wavelength range of 60 nm below the threshold. The wavelength of maximum bleaching is shifted to shorter wavelengths with decreasing particle size (size quantization effect). Maximum bleaching occurs with a negative absorption coefficient of $1.1 \times 10^5 \text{ M}^{-1}\text{cm}^{-1}$. Electrons are also stored upon UV illumination of colloidal ZnO. The stored electrons react rather slowly with oxygen, the rate constant becoming lower with increasing particle size, and more rapidly with peroxy radicals.

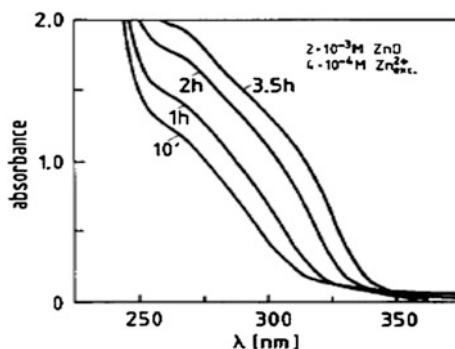
After the preparation of ZnO as transparent colloidal solution became possible the photochemical studies on this material could be extended by the application of the fast kinetic methods of flash photolysis and pulse radiolysis. The previous studies have shown that electrons deposited on small particles of ZnO influence their optical absorption and fluorescence. Excess electrons can be generated either by UV light absorption in the colloidal particles or by electron transfer from reducing free radicals produced radiolytically in the bulk solution. Both methods are described in the present paper. Experiments of this type are of fundamental importance for the understanding of the mechanism of interfacial electron transfer in heterogeneous photocatalysis and of the mechanism of electron storage on semiconductor microelectrodes.

The preparation of ZnO sols has previously been described. In principle, Zn^{2+} ions are reacted with NaOH in alcohol solution, making use of the dehydrating properties of this solvent to prevent the formation of zinc hydroxide. However, it is crucial to use an alcohol having a certain water content that controls the rate of growth of the colloidal particles. The mechanism of ZnO formation is rather complex and poorly understood. Some improved methods of preparation are also described in the present paragraph. Small ZnO particles show typical size quantization effect, the onset of light absorption and position of the fluorescence band being shifted to shorter wavelengths with decreasing particle size. This effect has now been investigated in more detail to obtain the relationship between particle size and the wavelength of the absorption threshold.

ZnO forms stable colloids in methanol if either Zn^{2+} or OH^- ions are present in excess. For the preparations described below, two stock solutions were made: one is 0.2 M NaOH in CH_3OH by dissolving 2.0 g of NaOH in 250 mL of methanol, other one is 0.2 M $\text{Zn}(\text{ClO}_4)_2 \cdot 6\text{H}_2\text{O}$ by dissolving 7.448 g of this salt in 100 mL of methanol p.a. (water content <0.05 %). ZnO Sols is with excess Zn^{2+} ions. The opalescing solution was then stirred overnight at 20 °C. The opalescence disappeared, and a transparent 2×10^{-3} M ZnO solution with 4×10^{-4} M excess Zn^{2+} was obtained. This solution was stable for about 1 week and contained relatively small particles (mean diameter $\sim 20 \text{ \AA}$). Using 1:1 dilution with methanol led to a substantial increase in stability (stable for weeks). Figure 2.29 shows how the spectrum of the colloid developed after the addition of the stock solution.

The absorption threshold moved towards longer wavelengths as the particles grew, which is explained by the quantization of the electronic energy levels in the small particles. The mean size of the ZnO particles in the diluted methanol solution was about 20 Å. The solution had an absorption of only a few percent at 347 nm,

Fig. 2.29 Development of the absorption spectrum of ZnO in methanol at 20 °C and in the presence of 20 % excess Zn^{2+} ions. The long wavelength tail is due to scattering which becomes smaller with increasing reaction time

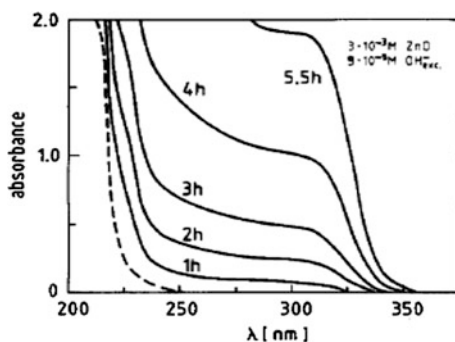


the wavelength of the frequency-doubled ruby laser with which the flash photolysis experiments were performed. A solution with a stronger absorption at 347 nm was obtained by mixing. The diluted methanol solution is with water (60 % water, 40 % solution) under argon. The particles grew in the mixture to about 40 Å.

For ZnO Sols with Excess OH^- Ions, two procedures were applied where first a tetrahydroxozincate solution was made in which ZnO developed in the presence of a small amount of water. In the first procedure, 75 mL of stock solution A was diluted with 600 mL of methanol. A mixture of 15 mL of solution B and 70 mL of methanol was added under vigorous stirring. The zincate solution formed was transparent and stable. ZnO formation was started by adding a mixture of 5 mL of water and 95 mL of methanol under strong shaking. Methanol was added to bring the solution to a volume of 1 L and stirred for 24 h at 20 °C. The transparent ZnO sol, which was stable at 20 °C for weeks, contained 3×10^{-3} M ZnO and 9×10^{-3} M excess OH^- . Lower OH^- concentration led to less stable sols. Figure 2.30 shows the absorption spectrum during the development of the colloid. Again, one observes a shift of the absorption threshold to longer wavelengths.

Note that the threshold after long ripening of the colloid is still far below 372 nm, the threshold of macro crystalline ZnO. In the second procedure, a very concentrated ZnO sols was obtained which then was diluted with methanol. It could also be finished from American Chemical Society Colloidal Semiconductor is

Fig. 2.30 Development of the absorption spectrum of ZnO in methanol at 20 °C and in the presence of 300 % excess OH^- ions. The dashed line is the spectrum of the zincate solution



diluted with 2-propanol or 2-methyl-2-propanol to obtain sols where these diluents were the main solvents (>95 %).

A 10 mL sample of stock solution B was added dropwise to 50 mL of stock solution A. The transparent zincate solution obtained was stored in a closed vessel at 20 °C. ZnO formed over 2 days, the reaction of zincate being initiated by the water content of solution B (due to the water in $\text{Zn}(\text{ClO}_4)_2 \cdot 6\text{H}_2\text{O}$). The sol finally obtained contained 3.3×10^{-2} M ZnO, 0.2 M water, and 0.1 M excess OH^- . As it was stable for only a few days, it was diluted with 940 mL of methanol, giving a solution containing 2×10^{-3} M ZnO and 6×10^{-3} M excess OH^- which was stable at 20 °C for weeks. When the concentrated sol was diluted with 2-methyl-2-propanol or 2-propanol, the particle sizes were determined by transmission electron microscopy. To prepare the samples, a drop of the colloid solution was applied to a copper mesh covered with a carbon film for 30 s and subsequently removed with a paper tip. Adhesion of the particles was promoted by exposing the carbon film to a glow discharge prior to this procedure. The granulation contrast originating from the amorphous carbon film was suppressed by an apodization technique.

Irradiations were carried out with a pulsed laser or a 4-MeV Graff generator. The radicals were produced in a low concentration of less than 10^{-6} M to avoid radical–radical deactivation. In some experiments a train of pulses with long intervals between the pulses was applied. The signals for eight pulses (or trains of pulses) were averaged. The base line was recorded every other pulse and finally subtracted from the recorded signals. The γ -irradiations were carried out with a source. The flash photolysis experiments were performed with a frequency-doubled ruby laser ($\lambda = 347.1$ nm, 15-ns pulse width). The data from several flashes were digitized and transferred to the results of a quantum mechanical calculation in Fig. 2.32 (---).

Fig. 2.31 Electron microscopic histograms of ZnO sample. The arrows point to the extrapolated values of the particle size

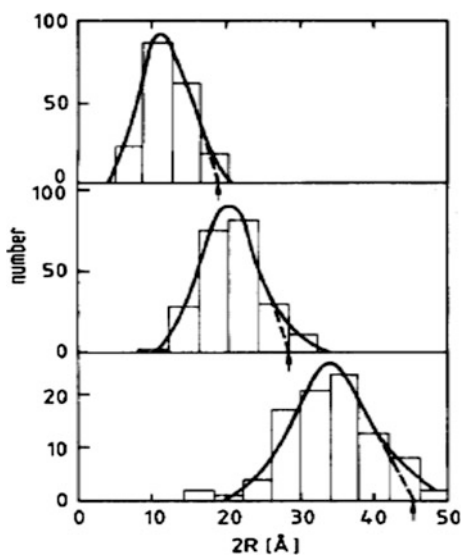
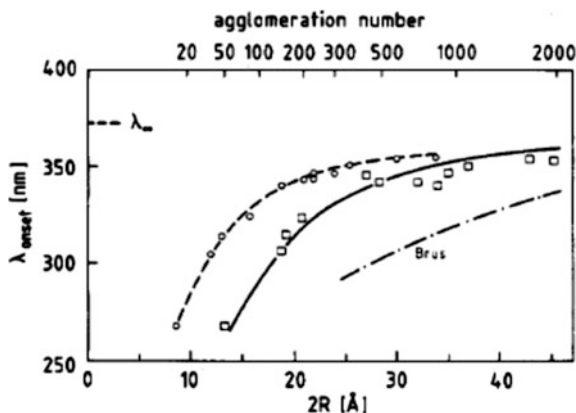


Fig. 2.32 Wavelength of absorption onset as a function of particle size: (squared line) experimental points obtained by extrapolation (see Fig. 2.32); (circled line) mean size of the samples (dotted line) used quantum mechanical calculation



Colloidal ZnO is very sensitive towards UV light. It was therefore necessary to carry out the laser flash and electron pulse experiments with a low-intensity analyzing light beam.

2.5.2 Particle Size and Absorption

Figure 2.31 shows histograms of various ZnO colloids as determined by electron microscopy. The solution was investigated at different times after precipitation, and at different phases of particle growth. As has already been described for cadmium sulfide the particle size, which can be related to the onset of absorption, was obtained by extrapolating the steep part of the size distribution curve. The onset of light absorption was obtained by extrapolating the steep part of the rising absorption curve. In Fig. 2.32, the wavelength of the absorption threshold is plotted versus the particle diameter. Above 40 Å, the particles absorb close to 372 nm, where macro crystalline ZnO starts to absorb. With decreasing size, the onset is more and more rapidly shifted towards shorter wavelengths. Figure 2.32 also contains a curve which relates λ_{onset} with the mean particle size of the samples as determined by electron microscopy. This curve is of practical interest, when one wishes to obtain the mean agglomeration number or the concentration of the particles from the absorption spectrum.

2.5.3 Laser Flash Photolysis

As Fig. 2.33a, b shows the time profiles of the absorbance changes which were recorded after application of a single 347-nm flash of the ruby laser. Immediately after the flash, a negative signal was observed at 320 and 340 nm, respectively.

The higher concentration of oxygen in the solution, the more rapidly it decayed after the flash. In the case of the small particles as Fig. 2.33a the decay was much faster than for the larger ones as Fig. 2.33b. The spectra of the absorbance change are shown in the upper part of Fig. 2.34a, b. The lower part of the figures contains the absorption spectra of the solutions. It is seen that the signal is negative in a wavelength range of about 60 nm below the onset of absorption. In the previous studies on the continuous illumination of deaerated ZnO solutions long-lived bleaching had been observed in this wavelength range. The dashed curve in the lower part of Fig. 2.34b is the absorption spectrum of the solution after the laser flash as calculated from the original absorption spectrum and the changes in

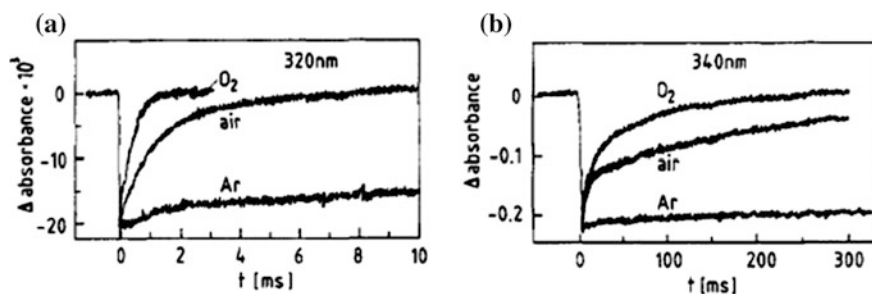


Fig. 2.33 **a** Change in absorption as a function of time after a laser flash. 1×10^{-3} M ZnO and 2×10^{-4} M excess Zn^{2+} in methanol. Concentration of absorbed photons: $4 \times M$. Mean ZnO particle size: 17 Å. **b** Change in absorption as a function of time after a laser flash. 8×10^{-4} M ZnO and 1.6×10^{-4} M Zn^{2+} in methanol-water (40:60 vol.%). Concentration of absorbed photons: 3×10^{-4} M. Mean ZnO particle size: 40 Å

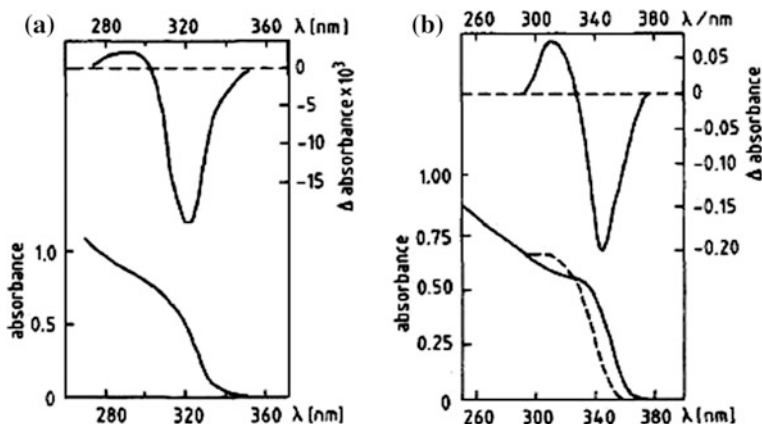
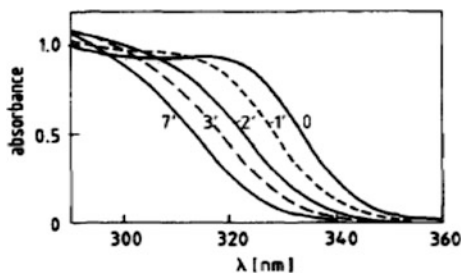


Fig. 2.34 **a** Up absorbance immediately after the laser flash as a function of wavelength. Down absorption spectrum of the ZnO solution which as in Fig. 2.33a. **b** Up absorbance after the laser flash immediately as a function of wavelength. Down absorption spectrum (full line) of the ZnO sol and spectrum (dashed line) of the solution after the laser flash. Solution is in Fig. 2.33b

Fig. 2.35 γ -irradiation of a deaerated 1×10^{-3} M ZnO sol in methanol containing 0.1 M formaldehyde and 3×10^{-3} M NaOH.

Absorption spectrum is at different times of irradiation and dose rate is 2.45×10^4 rad/h

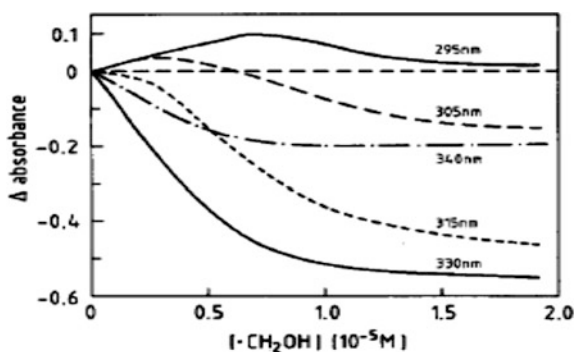


absorption. Note that the absorbance at the laser wavelength of 347 nm was much lower in the experiments of Fig. 2.34 than in those of Figs. 2.33b and 2.34b.

A deaerated solution of 1×10^{-3} M ZnO containing 3×10^{-3} M excess NaOH and 0.1 M formaldehyde as electron scavenger was γ -irradiated at a dose rate of 2.45×10^4 rad/h. Figure 2.35 shows the absorption spectrum at different times of irradiation. It is seen that the onset of absorption was shifted to shorter wavelengths, this effect becoming less and less pronounced with increasing irradiation time until a final shift was reached after about 7 min. γ -Ray absorption produces reducing organic radicals, CH_2OH , with a radiation chemical yield of 6.6 radicals per 100 eV of absorbed radiation energy, which are dissociated in the presence of NaOH: $\text{CH}_2\text{OH} + \text{OH}^- \rightarrow \text{CH}_2\text{O}^- + \text{H}_2\text{O}$. The reaction of these radicals with the colloidal particles produced the same shift of absorption as the direct illumination with UV light.

The shifts persisted after the irradiation for about 20 min and then very slowly disappeared. Exposure of the irradiated solution to air led to an immediate recovery of the absorption spectrum. In Fig. 2.36, the change in absorbance at various wavelengths is plotted as a function of the radiation dose. The latter is given in terms of the concentration of CH_2OH radicals produced. It is recognized that a decrease in absorbance was observed at wavelengths above about 315 nm. At shorter wavelengths an increase occurred in the early stages of irradiation, followed by a decrease at higher doses.

Fig. 2.36 Change in absorbance at various wavelengths as a function of irradiation dose (dose expressed as concentration of radicals generated). Solution is shown in Fig. 2.35



Two sols of different particle size were used in the pulse radiolysis experiments. Sol A contained particles of mean size 30 Å in water-methanol (60:40 vol.%) sol B contained 20 Å particles in methanol. The absorption spectra of both solutions are shown in the lower part of Fig. 2.37.

Two kinds of experiments were performed with these sols. In the first experiment, the solution was saturated with nitrous oxide and the intensity of the analyzing light beam kept very low. Under these conditions, CH_2OH radicals were generated which attacked the colloidal particles after the pulse. In most of the experiments, a train of eight pulses were used, the duration of a pulse being 1.5 ps and the interval between the pulses 50 ms. Typical kinetic traces are shown in Fig. 2.38 for sol A. It can be seen that the absorption at 340 nm decreased within a few milliseconds after each pulse, the decrease after the first pulse being noticeably smaller than after the following ones. At 320 nm, however, an increase after each pulse was observed. Similar observations were made with sol B. The absorbance

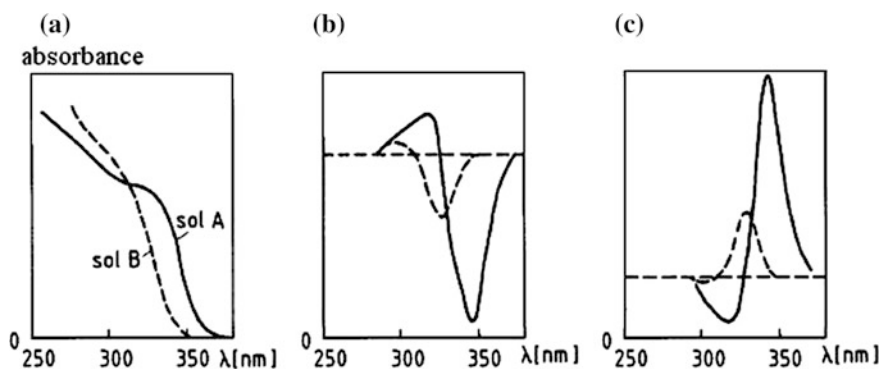
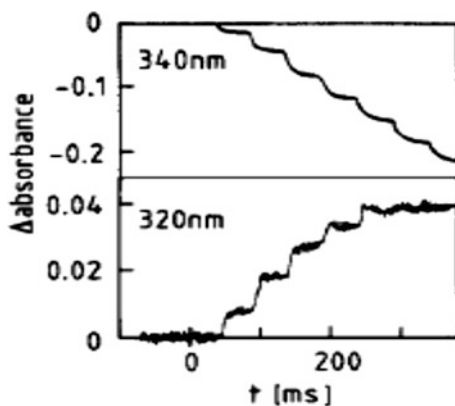


Fig. 2.37 a Absorption spectrum of the two colloids (sol A and B), b difference spectra in the irradiation of the solutions under N_2O and air (c), with N_2O saturated solutions, the intensity of the analyzing light beam was very low and high intensity

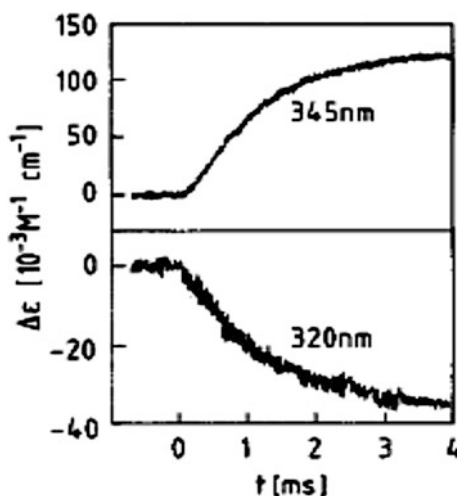
Fig. 2.38 Changes in absorbance of sol A (30 Å, particles) upon irradiation with a train of pulses (irradiation under N_2O , low intensity of analyzing light beam)



changes after the third pulse were used to construct the difference spectra shown in part b of Fig. 2.37. They are very similar to the spectrum obtained with laser illumination (see Fig. 2.35), i.e., bleaching was occurred in a certain wavelength range below the absorption to increase absorption at shorter wavelengths.

The difference spectrum was more intense for sol A ($\Delta\epsilon_{\text{cmax}} = -1.1 \times 10^5 \text{ M}^{-1} \text{ cm}^{-1}$). Note that the observed changes in absorbance were independent of the analyzing light intensity provided that low intensities were applied. In the second experiment, the solutions contained air and the intensity of the analyzing beam was high. Under these circumstances oxidizing free radicals, such as O_2^- and $\text{O}_2\text{CH}_2\text{OH}$, were formed which reacted with the colloidal particles during the interval between the pulses. Figure 2.39 shows kinetic traces obtained with sol A in single-pulse experiments. Depending on the wavelength, bleaching or absorption signals were observed. Note that the half-life time of the buildup of these changes was independent of the wavelength of absorption. It amounted to 0.84 ms. The difference spectra for the two sols are shown in part of Fig. 2.37. It is seen that these spectra are mirror images of the spectra shown in part b. In other words, where bleaching occurred in the experiments of part b absorption signals were observed in the experiment of part a, and vice versa. Note that in these experiments the change in absorption became stronger with increasing intensity of the analyzing light. Experiments under N_2O were also carried out with solutions in which 2-propanol or 2-methyl-2-propanol were the solvents (besides a small amount of methanol; see experimental section). It was found that the $(\text{CH}_3)_2\text{COH}$ radicals, which were generated in 2-propanol, reacted as fast with the colloidal particles as the CH , OH radicals produced in methanol solution. The $\text{CH}_2(\text{CH}_3)_2\text{COH}$ radicals which were generated in 2-methyl-2-propanol did not react with the ZnO particles.

Fig. 2.39 Changes in absorption of sol A in a single-pulse experiment (irradiation under air, high intensity of analyzing light beam)



ZnO cannot be made as a colloid by reaction of Zn^{2+} ions with NaOH as the hydroxide which is formed does not dehydrate: $\text{Zn(OH)}_2 \rightarrow \text{ZnO} + \text{H}_2\text{O}$. In fact, it can be calculated from the thermodynamic data of the substances involved that the dehydration reaction is practically thermoneutral at room temperature. That ZnO is formed in alcoholic solution must be due to a substantially lower free enthalpy of the products of hydration. Kinetically, the process is very complex. It was observed that ZnO is formed in alcoholic solutions only in the presence of small amounts of water. Further in the preparations, first a stable solution of tetrahydroxozincate was made, and the formation of ZnO was initiated by the addition of water to this solution. It thus seems that water exerts a catalyzing effect on the transformation of zincate into ZnO in methanol solution. No detailed mechanism of this catalysis can be given at the present time.

2.5.4 Particle Size and Absorption Threshold

Quantum mechanical calculations of the shift of the band gap in small semiconductor particles were carried out. The lowest eigenstate of an exciton was calculated by solving Schrodinger's equation at the same level of approximation as is generally used in the analysis of bulk crystalline electron-hole states. Both the electron and the hole were considered as particles in a spherical box, and the usual values of the effective masses of the charge carriers were used. More recently, it was shown that the experimental observations on small CdS particles could be well described by wave mechanical one body calculations using a wave function of the form $\exp(-\gamma r)\psi_1(r)$, where the hydrogen-like factor takes account of the Coulomb attraction and $\psi_1(r) = 1/r \sin(\pi(r/R))$ is the lowest particle in-a-spherical-box orbital (r = variational parameter, R = radius of the particle, r = distance from center of particle). For $r \geq R$, a potential increase of 3.8 eV was used. The curve in Fig. 2.32 was calculated by using the above wave function, expressing r and R in units of $\epsilon_\infty \hbar^2 / \mu^* e^2$, where the reduced effective mass, μ^* was 0.1775 and the dielectric constant of ZnO (ϵ_∞) was 3.82, and again using a potential jump of 3.8 eV. Taking into consideration that certain unknowns exist in these calculations such as the exact shape of the particles and the applicability of the bulk values of μ^* and ϵ_∞ , one may conclude that there is good agreement between the experimental observations and the theoretical calculations on small ZnO particles. The results of calculations are also included in Fig. 2.32. They over estimate the size quantization effect.

2.5.5 Blue Shift of Absorption upon Illumination

In the laser flash photolysis experiments (Figs. 2.33 and 2.34) similar observations were made as in the previous studies on the continuous illumination of ZnO sol. The onset of absorption was shifted to shorter wavelengths; i.e., an effect was observed as if the particles had become smaller under illumination. In fact, in our first explanation of the phenomenon, a mechanism of dissolution of illuminated ZnO was discussed and the absorption shift attributed to the decrease in size of the colloidal particles. However, after it was found later in the case of small CdS particles that storage of an electron affected the absorption spectrum in the same way, it was proposed that illumination of ZnO particles also produces excess electrons. The shift is explained by an increase in the energy of the exciton formed by light absorption due to the strong electric field caused by the excess electron. Perhaps, it could also be explained as the first step of “band filling,” where by the excess electron fills the lowest state so that subsequent absorption requires higher photon energies in order to access empty states. The conclusion that the shift is caused in ZnO by excess electrons is corroborated by the fact that the shift in aqueous ZnO sols was much stronger when alcohol was present. The alcohol acts as a scavenger of the positive holes, simultaneously formed upon light absorption, and thus prevents the electrons from recombining with holes.

The excess electrons are long-lived in the absence of oxygen. In the presence of O, they are removed from the colloidal particles which explain the decay of the bleaching signal after the laser flash (Fig. 2.33). However, this reaction is relatively slow. From the half-life time of 0.8 ms in air-saturated solution as Fig. 2.33a, one calculates a rate constant of $3.2 \times 10^6 \text{ M}^{-1} \text{ s}^{-1}$ for the reaction of O₂ with electrons stored on 17 Å ZnO particles. In the case of 40 Å particles to see Fig. 2.33b the specific rate is about 50 times lower. It thus seems that the electrons are present in traps of less negative potential in the case of large particles as is expected from the theory of size quantization. In the laser experiments, where the wavelength of the exciting light was not far from the onset of absorption, smaller particles in the solution were less excited, or even not at all, than the larger particles which possibly absorbed more than one photon. Under these conditions, a more detailed analysis of the data, such as a correlation between the amount of bleaching and the number of excess electrons, did not seem promising. Clearer conditions prevailed in the γ -radiolysis experiments where the number of stored electrons was known and no loss of electrons due to recombination with holes had to be feared. The γ -Radiolysis: Electron Injection from Free Radicals. When reducing radicals, which are formed in the γ -irradiation of methanol or 2-propanol solutions, react with ZnO particles, similar changes in the absorption spectrum were observed as in the UV illumination of such solution. The effects are explained in terms of electron injection from the organic radicals onto ZnO particles. In fact, CH₂OH and (CH₃)₂COH radicals have reduction potentials (−1.0 and −1.5 V, respectively) which are much more negative than the lower edge of the conduction band in ZnO (−0.2 V). On the other hand, the CH₂(CCH₃)₂OH radicals, formed in 2-methyl-2-propanol solution, did not react

with ZnO which is understood in terms of the lower reducing power of such radicals.

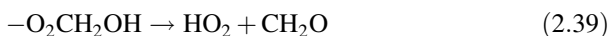
From the initial slope of the curve for 330 nm, where maximum bleaching occurred in the experiments of Fig. 2.36, a negative absorption coefficient of $9 \times 10^4 \text{ M cm}^{-1}$ is calculated. The mean agglomeration number of the colloidal particles was 230. At an overall concentration of $8 \times \text{M ZnO}$, the particle concentration was $3.5 \times 10^{-6} \text{ M}$. The solution had an absorbance of 0.6 at 330 nm (curve 0 in Fig. 2.36), the absorption coefficient of the colloidal particles being $0.6/3.5 \times 10^{-6} = 1.7 \times 10^5 \text{ M cm}^{-1}$. Thus, find that deposition of an electron on a small colloidal ZnO particle is accompanied by a decrease in its 330-nm absorption by almost a factor of 2. This indicates that the excess electron influences not just one ZnO molecule in the colloidal particle but an optical transition in which practically all the ZnO molecules in the particle are involved. It has made similar arguments in previous study on electron deposition on small CdS particles. When more than one electron is deposited per ZnO particle, i.e., when more than about $3.5 \times \text{M}$ free radicals were generated in the experiments of Fig. 2.36, the changes in absorbance no longer increased in a linear manner. At 330 and 340 nm, the absorbance decreased less and less strongly. At 315 nm, little absorption changes occurred during deposition of just one electron, but significant bleaching took place upon the storage of additional electrons. The shorter wavelengths occurred upon deposition of the first electron, which decrease further electron injection. The nature of the stored electrons is not known yet. They could be present in traps or in the form of monovalent zinc ions, Zn^+ . The latter possibility does not seem very plausible because of the very negative redox potential of Zn^+ ($< -2 \text{ V}$). On the other hand, Zn^+ is known to absorb close to 300 nm, i.e., the wavelength where the absorption increased upon deposition of one electron. When more than one electron is present, isolated Zn atoms may be formed.

2.5.6 Reducing Reactions and Oxidizing Radicals

As in the continuous irradiation experiments (Fig. 2.35), the reaction of pulse radiolytically generated CH_2OH radicals with ZnO particles caused bleaching at longer and absorption at shorter wavelengths (Figs. 2.37 and 2.38). Upon application of the first pulse (Fig. 2.38) the changes in absorbance were smaller than in the subsequent ones. This is attributed to traces of oxygen adsorbed on the colloidal particles which cannot be removed by bubbling the solution with another gas. The small radiation dose applied in the first pulse was sufficient to remove this residual oxygen. The rate constant of reaction of the radicals with ZnO particles was determined in a single-pulse experiment using a solution which had been preirradiated with two pulses. At a concentration of ZnO particles of $3.5 \times 10^{-6} \text{ M}$ the half-lifetime of the 340-nm bleaching, which obeyed pseudo-first-order kinetics

was about 2 ms. A rate constant of $1 \times 10^8 \text{ M}^{-1} \text{ s}^{-1}$ is calculated. This value is more than 10 times smaller than expected for a diffusion-controlled reaction.

It has already been mentioned that the intensity of the analyzing light beam had to be kept low in the laser flash and electron pulse experiments using N_2O -saturated solutions in order to avoid storage of electrons on the ZnO particles before the laser flash or electron pulse arrived. In experiments with aerated solutions as Figs. 2.37a and 2.39, the intensity of the analyzing light beam was as strong as in ordinary pulse radiolysis experiments with chemical systems that do not photolyze. The reaction of oxygen with stored electrons being rather slow as described above, illumination with the analyzing light beam led to a certain stationary concentration of stored electrons on the colloidal particles. The oxidizing radicals which were formed in the electron pulse via the processes that reacted with ZnO particles carrying electrons as following:



Removal of an electron by an oxidizing radical was accompanied by the recovery of the bleaching (at 345 nm) and of the absorption (at 320 nm) which were originally caused by this electron. The result being that an absorption signal at 345 nm and a bleaching signal at 320 nm were now observed (see Fig. 2.39). The mirror images of the difference spectra obtained after the attack of reducing and oxidizing radicals (as in Fig. 2.37) are thus readily understood. From the data in Fig. 2.39 it was calculated that the oxidizing radicals reacted with a specific rate of $3.2 \times 10^6 \text{ M}^{-1} \text{ s}^{-1}$ with the colloidal particles.

The changes in absorbance were smaller when ZnO particles of smaller size were used in the experiments of Fig. 2.37. When an excess electron is deposited on a smaller ZnO particle, the number of ZnO molecules affected is smaller, this effect leading to a smaller change in absorbance. On the other hand, one would expect that the optical changes should also become smaller in the case of very large particles (larger than used in the present work) as the electric field produced by the excess electron would be rather weak in parts of the particle. These two opposing effects make believe that there might exist a definite particle size where the absorbance changes that accompany the deposition of one electron are most pronounced. The large bleaching coefficient of $1.1 \times 10^5 \text{ M}^{-1} \text{ cm}^{-1}$, observed for 40–50 Å particles, may be taken as an indication that this particle size is close to 40 Å. However, further experiments with particles of different size are required to check the validity of this supposition. It has recently been proposed that the fluorescence of colloidal ZnO in aerated solution is brought about by a “shuttle” mechanism. An electron generated by light absorption transfers to adsorbed O_2 to form O_2^- . The latter transfers the electron into a deeper trap on the surface. Recombination with a preexisting hole is accompanied by light emission. In the course of the present

studies on solutions in which O_2^- is formed a few experiments were carried out to check this mechanism. In an experiment with the analyzing light beam shut off, fluorescence light should have been emitted, if O_2^- transferred an electron to ZnO and if recombination with a preexisting hole took place. No fluorescence was observed. Have to conclude that the more direct kinetic method of pulse radiolysis does not confirm the above mechanism. A shuttle mechanism in solutions containing methyl viologen, MV^{2+} , as additive has also been proposed, MV^+ acting as the shuttle agent, which is formed by electron transfer to MV^{2+} and then transfers its electron into a lower surface state of ZnO. More recent pulse radiolysis experiments in our laboratory showed that MV^+ does not react with ZnO particles. Again, it must be concluded that a shuttle mechanism is not operative.

2.5.7 Essential Criteria of Photochemical Reactions

Essential criteria for all photochemical reactions is including molecule must absorb light and radiation energy must match energy difference of ground and excited state. Typical absorption range of some important classes of organic compounds is including kinds of simple alkene (190–200 nm), acyclic diene (220–250 nm), cyclic diene (250–270 nm), styrene (270–300 nm), saturated ketones (270–280 nm), α , β -unsaturated ketones (310–330 nm), aromatic ketones/aldehydes (280–300 nm), aromatic compounds (250–280 nm), etc. But the light is absorbed by a molecule also. The Franck–Condon principle says that the heavy atom nuclei do not change their positions. This leads to an initial geometry of the excited state which is usually not the energy minimum. During excitation the electron spin remains unchanged. Spin inversion during excitation is forbidden by quantum mechanics and therefore unlikely. Right after the excitation several things may happen. (1) Vibronic relaxation brings the molecule quickly into the new energy minimum structure for the excited state. Energy is released into the solvent. (2) Intersystem crossing leads to triplet states by spin inversion. The new energy minimum is reached by vibrational relaxation. (3) Emission of light and return to the ground state (luminescence, fluorescence, phosphorescence). (4) Quenching of the excited state: Energy is transferred to another molecule. Usually, we observe diffusion-controlled dynamic quenching by collision. Investigation of this is possible by the Stern–Vollmer plot (1/quantum yield vs concentration of quencher). Gives a straight line for diffusion-controlled quenching; large excess of quencher usually needed (1000 times excess). Molecule goes back to ground state by vibrational (thermal) deactivation (no light emission). The energy goes to the solvent/environment of molecule and pathways of photochemical processes as shown Fig. 2.40 [18, 19].

2.5.8 Main Types of Photochemical Reactions

The excited states are rich in energy. Therefore, reactions may occur that are highly endothermic in the ground state. Using the equation $E = h\nu$ can correlate light of a wavelength of 350 nm with an energy of 343 kJ/mol. In the excited state anti-bonding orbitals are occupied. This may allow reactions which are not possible for electronic reasons in the ground state. Photochemical reaction can include singlet and triplet states. Thermal reactions usually show singlet states only. In photochemical reaction intermediates may be formed which are not accessible at thermal conditions as shown in Fig. 2.40.

The main influence complications to photochemical reaction and practical considerations for experiment as following:

1. Purity of starting materials is importance.

This prerequisite holds for many techniques in synthesis. While working with organometallic intermediates requires exclusion of air and moisture, photochemistry is very sensitive to colored or light absorbing impurities—either in the starting materials or formed during reaction. Both may interfere with the photo processes and may kill the reaction.

2. UV spectra of substrates.

Before starting a photochemical reaction a UV/vis spectrum of the “photoactive” compound is recorded. The “photoactive” compound is the molecule which should be electronically excited and undergo or initiate a reaction from its excited singlet or triplet state. From UV spectra recorded with different compound concentrations the extinction coefficients of all bands can be obtained, even for the weak absorptions which may be of importance. UV spectra of all reagents should be recorded to make sure that there is no or little interference in absorption with the “photoactive” compound. If available, a UV spectrum of the product should be recorded. UV spectra from the reaction mixture may help to identify ground-state interactions of compounds or CT complexes, and guide the way to the best reaction conditions. The UV spectrum of a photochemical reaction is shown in Fig. 2.41.

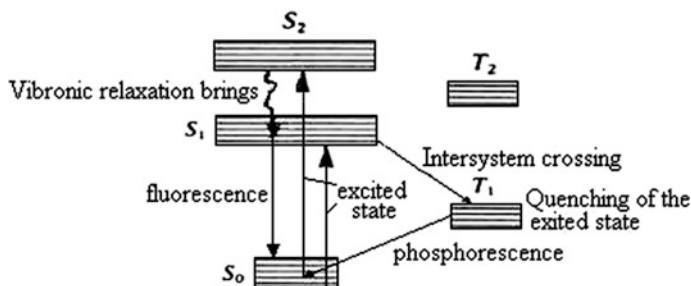


Fig. 2.40 The photochemical reaction may occur

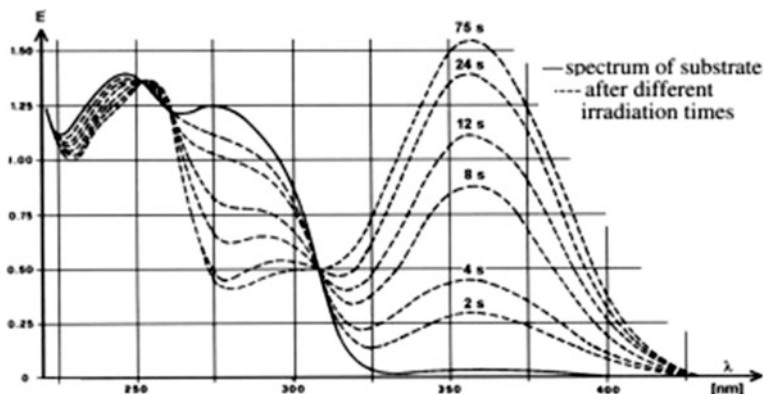


Fig. 2.41 UV spectrum of a photochemical reaction

2.5.9 Solvents

Photochemical reactions can be performed—in principle—in the gas phase, in solid state or in solution. For practical reasons most photochemical reactions are done in solution, therefore the choice of the right solvent is critical. At normal concentrations of a photochemical reaction the concentration of the “photoactive” compound is only 100–1000 times larger than the concentration of the solvent. If the extinction coefficient of the “photoactive” compound is only 10 times higher than that of the solvent at the irradiation wavelength, we will observe a significant filter effect of the solvent. The reaction is much slower than it could be.

Key selection criteria are including: solvent must dissolve reactants (try), solvent should be transparent at the irradiation wavelength and solvent must be free of impurities (analysis; add edta to complex trace metal ion content if necessary). If a reactive intermediate needs to be stabilized by the solvent, this has to be tried out until a solvent is found which matches all criteria. The solvents used for photoreaction is shown in Table 2.1.

2.5.10 Direct Sensitized Photolysis

The absorption characteristics do not tell anything about the behavior of a molecule in the excited state. It may rapidly deactivate via fluorescence or radiationless, it may undergo intersystem crossing into the triplet manifold. If available, data on fluorescence, phosphorescence, lifetimes, and quantum yield are very helpful to understand the processes.

From these data we can learn if it is necessary to sensitize the formation of the triplet state for a reaction or if the triplet is rapidly formed without our

Table 2.1 Solvents used for photoreaction

Solvent	Cut-off wavelength ^a	ϵ_r^b	ET (30) ^c
Water	185	78.30	63.1
Acetonitrile	190	35.94	45.6
<i>N</i> -hexane	195	1.88	31.0
Ethanol	204	24.5	51.9
Methanol	205	32.66	55.4
Cyclohexane	215	2.02	30.9
Diethyl ether	215	4.20	34.5
1,4-dioxane	230	2.21	36.0
Methylene chloride	230	8.93	40.7
Chloroform	245	4.81	39.1
Tetrahydrofuran	245	7.58	37.5
Ethyl acetate	255	6.02	38.1
Acetic acid	250	6.17	51.7
Carbon tetrachloride	265	2.23	32.4
Dimethylsulfoxide	277	46.45	45.1
Benzene	280	2.27	34.3
Toluene	285	2.38	33.9
Pyridine	305	12.91	40.5
Acetone	330	20.56	42.2

^aWavelength (nm) at which E is approximately 1.0 in a 10 mm cell

^bDielectric constant

^cDimroth Reichardt values (kcal/mol) for the longest-wavelength solvatochromic absorption based on a pyridinium-*N*-phenoxide betaine dye 30

help. Sometimes the solvent can be used as a sensitizer. Then it should adsorb at the irradiation wavelength and transfer the energy to the reactant. Acetone is a typical example of such a solvent (adsorbs up to 330 nm). Sensitizers and quenchers can help to investigate a photochemical reaction:

1. Pure singlet reactivity: No reaction in the presence of appropriate triplet sensitizers.
2. Pure triplet reactivity: enhanced product formation in the presence of appropriate sensitizers; no reaction in the presence of triplet quenchers.

Triplet as well as singlet reactivity: combination of methods (1) and (2) gives a product pattern corresponding to the specifically activated states. The sensitizers and quencher in nonpolar solvents were shown in Table 2.2, where (1) benzoic acid, (2) triplet energies in kJ/mol, (3) first excited singlet state energies in kJ/mol, (4) quantum yields for singlet-triplet intersystem crossing, (5) in polar solvents.

Table 2.2 The sensitizers and quencher in nonpolar solvents

Compound	E_T	E_S	Φ_{ISC}
Benzene	353	459	0.25
Toluene	346	445	0.53
Methyl benzoate	326	428	
Acetone	332	372	0.90/1.00
Acetophenone	310	330	1.00
Xanthone	310	324	
Benzaldehyde	301	323	1.00
Triphenylamine	291	362	0.88
Benzophenone	287	316	1.00
Fluorene	282	397	0.22
Triphenylene	280	349	0.86
Biphenyl	274	418	0.84
Phenanthrene	260	346	0.73
Styrene	258	415	0.40
Naphthalene	253	385	0.75
2-acetylnaphthalene	249	325	0.84
Biacetyl	236	267	1.00
Benzil	223	247	0.92
Anthracene	178	318	0.71
Cosine	177	209	0.33
Rose bengale	164	213	0.61
Methylene blue	138	180	0.52

2.6 Reaction Control

In the course of the reaction more and more product is formed which competes with the starting material for light. If the product is available its UV spectrum gives information about possible competition. The increasing absorption of irradiation by the product may stop the reaction before complete conversion will be reached. Therefore, it is important to follow the reaction by UV spectroscopy (see figure above of UV spectra during reaction). The formation of colored byproducts may stop a reaction before complete conversion, too. Chromatographic methods, such as TLC, GC, or HPLC should be used to gain information about the course of the reaction.

2.6.1 Side Reactions Can Easily Become the Major Track

Side reactions of photochemical reactions can in some cases become the major reaction pathway. Examples are photosensitizers, which are use in catalytic or

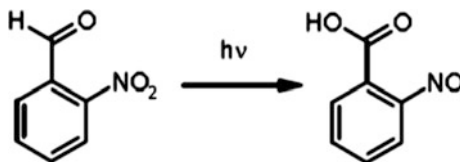
stoichiometric amounts to mediate the wanted photochemical process, but they may also act as photoinitiator of a radical chain reaction. If solvents or starting materials are present that are susceptible to a radical chain process, this reaction will become dominant. Another origin of severe side reaction may be the presence of oxygen. Photooxygenation may be the desired photoprocess, but if not, it may be a side reaction. Oxygen should be excluded to avoid this. Even if only small amounts of peroxides are formed during the reaction they may become hazardous upon work up. The use of inert gas is not necessary, if the essential excited state is not efficiently quenched by triplet oxygen (which is often the case for short living singlet states). Free radicals produced during the reaction may cause side reactions. Radical scavengers, such as phenols, are added to trap them.

2.6.2 Quantum Yield and Chemical Yield

While reactions of “normal ground state” chemistry are described by the chemical yield of the reaction as one major indicator (there are others, in particular when it comes to describe the technical efficiency of a chemical transformation), for the chemistry of excited molecules another parameter has to be considered: The quantum yield of the reaction. The quantum yield is the number of events (e.g., photochemical induced transformation) divided by the number of absorbed photons in a specific system. Quantum yields can range from 0 to 100 or higher; if smaller than 0.01 conversion is very slow (chemical yield may still be high); for photoinitiated chain reactions the quantum yield can be as high as 100.000.

How much light goes into the reaction (determination of the amount of product formed) which has to calculate a quantum yield. A standard chemical procedure used since the 1950s is chemical actinometry. A compound that undergoes a defined photochemical transformation with known quantum yield is used to determine the light intensity. The concentration of the actinometric compound and the pathway of the exposure cell must be sufficiently high to make kinetics of the reaction approx. zero order. In this way, the rate of the reaction is not concentration dependent. The reaction of 2-nitrobenzaldehyde to 2-nitrosobenzaldehyd is a typical example in Fig. 2.42 for example. The quantum yield of the process is 0.5 for irradiation from 300–410 nm, and the $d_{\text{Act}}/dt = I_0\eta f$, where I_0 is light intensity, η is quantum yield and f is fraction of absorbed light.

Fig. 2.42 The reaction of 2-nitrobenzaldehyde to 2-nitrosobenzaldehyd



Typical light sources for photochemistry are including:

1. Wavelength from 300 to 1300 nm lasers, the sun is about also.
2. Low-pressure mercury (Hg approx. 10^{-5} atm) lamp: 185 nm (5 %); 254 (95 %) (see Fig. 2.43).
3. Rayonet lamps (specific emission wavelength from secondary fluorescence emission with coated layer as shown in Fig. 2.43c).
4. Medium pressure Hg lamps (Hg vapor pressure 5 atm) lamps (distinct lines between 250 and 600 nm),
5. High-pressure Hg lamps (Hg vapor pressure approx. 100 atm; expensive, easily damaged) (emission 360–600 nm, broad).
6. Low and high-pressure sodium lamps (emission around 600 nm).
7. High power light-emitting diodes (available at low cost for 650–400 nm; very narrow and intensive emission, long lifetime; UV-LED are currently still expensive. The emission properties of them are shown in Fig. 2.43).

Many types of reactors for photochemical reactions are known, the most typical are:

1. Apparatus for external irradiation (simplest case is an irradiated flask).
2. Immersion-well reactor in which the lamp is surrounded by the reaction solution.
3. Falling film apparatus.
4. Photo microreactor (similar to falling film, but easier to handle).

In all cases the light sources usually needs cooling to avoid its overheating and heating of the reaction solution. The material of the reactor depends on the irradiation wavelength necessary.

For irradiation at 254 nm quartz glass (expensive apparatus) is needed. For irradiation at 300 nm Pyrex glass is needed, and for irradiation >350 nm normal lab glass (window glass) is sufficient. The glass acts as a solid filter. Additional solid or liquid optical filters may be used to restrict the irradiation wavelength.

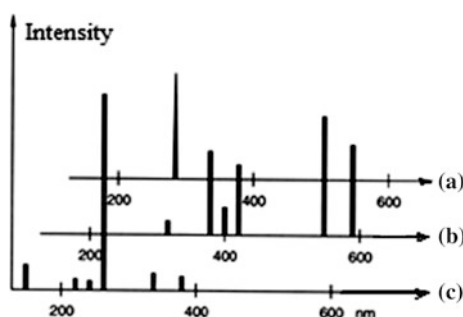


Fig. 2.43 The emission properties of *a* RPR-3000 Å for Rayonet photoreaction. *b* mercury low-pressure lamp and *c* mercury low-pressure lamp (strong 254 nm line)

Low-pressure mercury lamps have their main output at 254 nm. This light severely damages cells, eyes, and skin. Shield reactors; turn lamps off before checking the reaction. Never look into the beam of a high power LED; the lights very high intensity damage your eyes. Ozone generation: Short wavelength light may generate ozone from oxygen. Perform reactions always in a well ventilated fume hood. Lamps: Most lamps operate at high temperature and at high vapor pressure. Never move or touch lamps during operation. Never switch off the cooling right after switching of the lamp.

2.6.3 Photochemical Reactions

The absorption properties of ketones and aldehydes are convenient for irradiation around 300 nm ($n\pi^*$ 330–280 nm). Triplet–singlet energy gap is small (20–70 kJ/mol); intersystem crossing rates are high. Lifetime of first excited singlet state is in the nanosecond region for aliphatic aldehydes and ketones; in the sub-nanosecond region for aromatic aldehydes and ketones. Singlet photochemistry can be detected with aliphatic aldehydes or ketones, while aromatic substrates, such as benzophenone or acetophenone, react exclusively from their corresponding triplet states and are excellent triplet sensitizers.

1. Norrish Type I cleavage reaction (α -cleavage reaction)

This reaction type dominates gas phase photochemistry of many aldehydes and ketones. Less common in solution chemistry is only if no suitable C–H bonds, that are present to allow hydrogen atom abstraction. The examples of norrish type I cleavage reaction (α -cleavage reaction) as shown in Fig. 2.45 Special topic: 1 C–C Bond formation in organic crystals. Photochemical irradiation of crystalline (2*R*,4*S*)-2-carbomethoxy-4-cyano-2,4- diphenyl-3-butanone 1 led to highly efficient decarbonylation reactions. Experiments with optically pure and racemic crystals show that the intermediate radical pairs undergo a highly diastereomers and enantiospecific radical-radical combination that leads to the formation of two adjacent stereogenic centers in good chemical yield and with high chemical control.

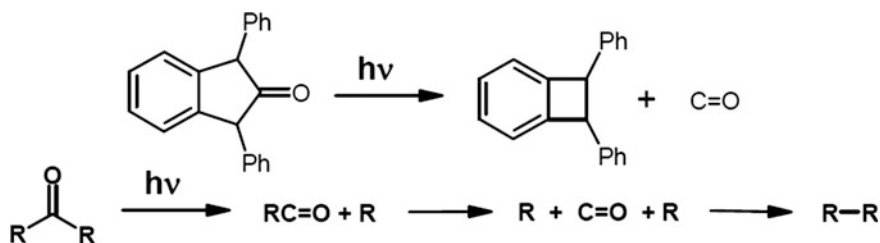


Fig. 2.44 The examples of Norrish type I cleavage reaction

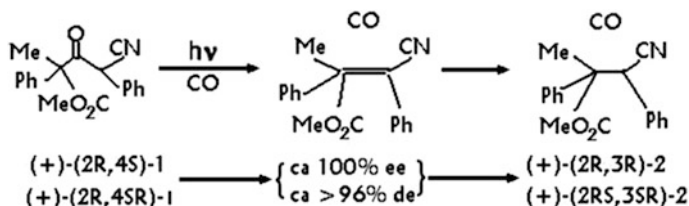


Fig. 2.45 Compound 1 was obtained in enantiomerically pure and racemic forms from 2-methyl-2-phenyl malonic acid monomethyl ester 3b. Samples of (+)-(R)-3b were prepared from the meso-diester 3a by enzymatic desymmetrization with pig liver esterase (90 %) or by resolution of acid (\pm)-3b with (-)-1-(1-naphthyl) ethylamine. Acid (+)-3b was converted into the corresponding acyl chloride, which was reacted with the anion of benzyl cyanide to give ketone (2R,4S)-1 and its diastereomer (2R,4R)-1a (not shown) in 85 % isolated yield in a 4:1 ratio

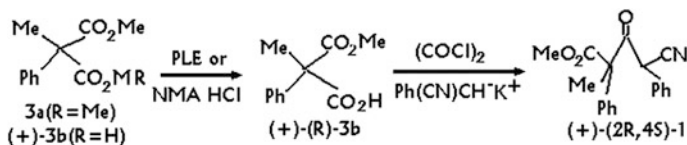


Fig. 2.46 Photochemical experiments with oxygen-free 0.1 M benzene solutions of (+)-(2R,4S)-1 and (\pm)-(2RS,4SR)-1 using a Pyrex filter (>300 nm) at 298 K led to complex product mixtures (as Fig. 2.47). The crystals of (+)-(2R,4S)-1 and (\pm)-(2RS,4SR)-1 (50 mg) irradiated under similar conditions resulted in a reaction with formation of a photoproduct in 40–60 % conversion and >95 % selectivity (in Fig. 2.46)

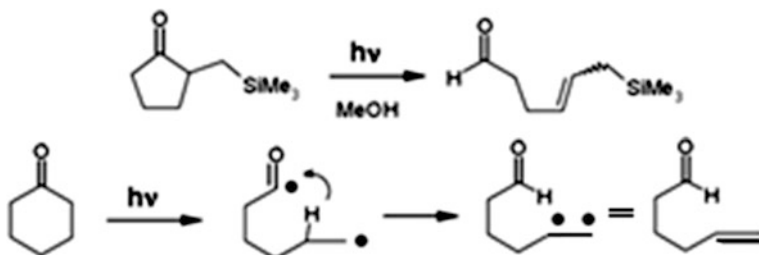


Fig. 2.47 The subsequent hydrogen migration

Reactions with chiral crystals occurred with quantitative enantiomeric yields and >95 % diastereomeric yields as shown in Figs. 2.44, 2.45 and 2.46.

2. Norrish type II photo elimination reaction

Beside carbon monoxide extrusion acyl radicals formed in a α -cleavage can be stabilized by subsequent hydrogen migration as an example is shown in Fig. 2.47.

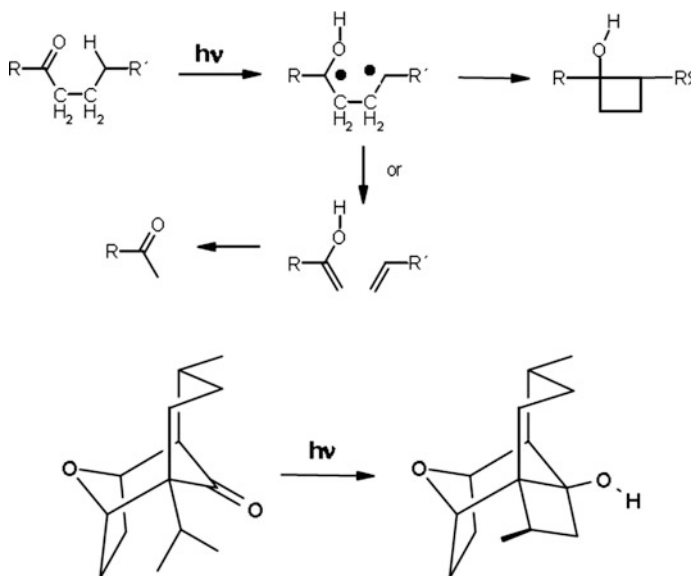


Fig. 2.48 The example the 1,4-diradical leads to cyclobutanols for C=O and C-H groups

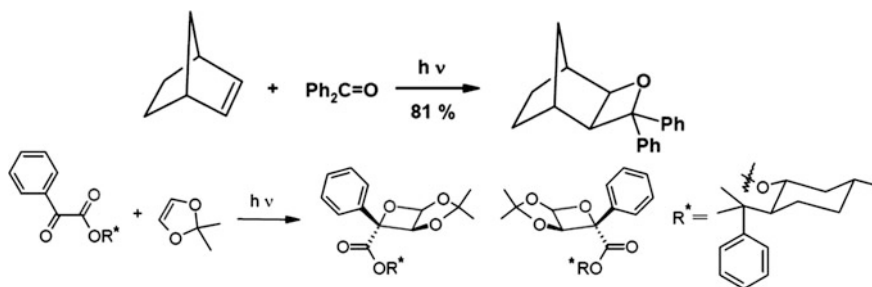


Fig. 2.49 The examples of high diastereoselectivities

3. Cyclobutanol formation

With an appropriate alignment of C=O and C-H groups and no secondary transformation prevents cyclization of the 1,4-diradical leads to cyclobutanols is shown in Fig. 2.48.

4. Photochemical [2 + 2] cycloaddition

The Photochemical [2 + 2] cycloaddition is photochemical [2 + 2] cycloaddition of an alkene and a carbonyl group reaction. Inter- and intra molecular examples are known. High diastereoselectivities can be observed in many examples in Fig. 2.49.

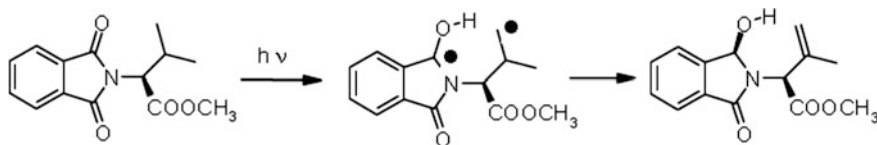
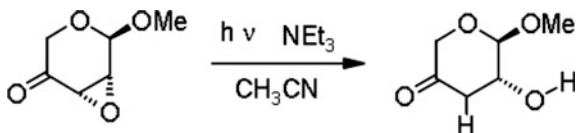


Fig. 2.50 An abstraction of hydrogen from the γ position

Fig. 2.51 The examples of photoreduction of an α, β -epoxy ketone



5. Photoisomerizations and photoreductions

Photoisomerizations and photoreductions are observed. Some examples are shown in Figs. 2.50 and 2.51:

In this reaction the first event is an abstraction of hydrogen from the γ position. Neither Norrish type II nor Yang reaction follow. Instead another hydrogen is stereoselectively transferred, now from the δ position.

The second example is a photoreduction of an α, β -epoxy ketone derived from carbohydrates. Triethylamine acts as the sacrificial electron and hydrogen donor. The configuration of one of the epoxy stereocenters remains intact as Fig. 2.51.

2.6.4 Alkenes

The formation of the lowest excited singlet state of simple alkenes arises from the allowed $\pi-\pi^*$ transition. This generally requires short wavelength irradiation extending to about 200–210 nm. Absorption of solvents and lack of suitable light sources make the use of simple alkenes in preparative photochemistry difficult. Substituted or conjugated derivatives are mainly used. Another possibility to circumvent the problem of absorption at short wavelengths is the use of sensitizers.

1. E,Z-Isomerizations

E,Z-Isomerizations of 1,2-disubstituted alkenes are well documented. A typical example is the photoisomerization of stilbene, where because of different absorption spectra the Z-isomere can be enriched in the photostationary state. A more complex example is the sensitized preparation of enantiomerically enriched trans-cyclooctene as Fig. 2.52.

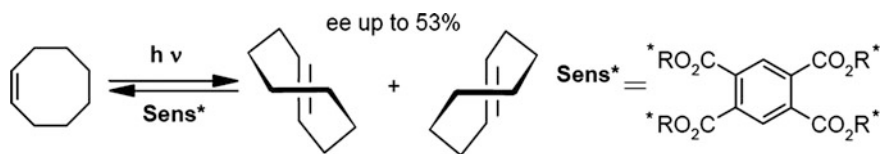


Fig. 2.52 The photoisomerization of stilbene

2. Sigmatropic shifts

These rearrangements involve a migration of a σ -bond across an adjacent π -system. The type of activation (thermal or photochemical) and the stereochemistry can often be predicted by the Woodward-Hoffmann rules. Processes involving stepwise biradical intermediates may be present in photochemical reactions as Fig. 2.53.

3. Di- π -methane rearrangement

This unique rearrangement was discovered later and belongs to the sigmatropic rearrangements of type. The rearrangement is stereospecific and has been used in organic synthesis as Fig. 2.54.

4. [2 + 2] Cycloaddition reactions

These transformations belong to the classic reactions that generally can be rationalized by the Woodward-Hoffmann rules. The [2 + 2] cycloaddition is photochemically allowed and a practical way to cyclobutane derivatives. Cyclobutane ring opening and hexatriene ring closure belong to the most frequently investigated

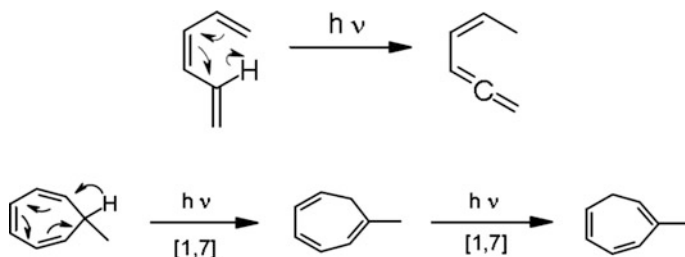


Fig. 2.53 Examples of processes involving stepwise biradical intermediates

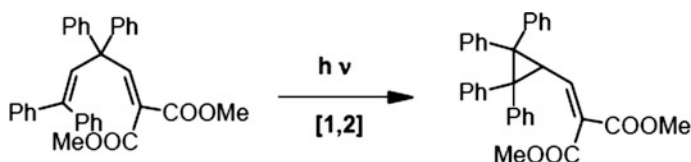


Fig. 2.54 Examples of the Di- π -methane rearrangement

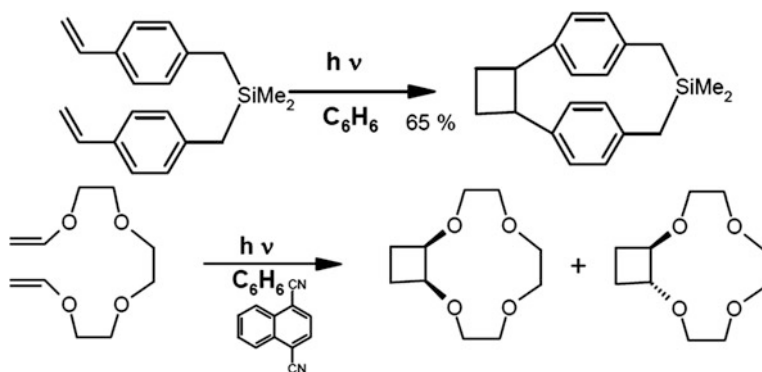


Fig. 2.55 Examples of intramolecular [2 + 2] photocycloaddition

electrocyclic reactions. The intramolecular [2 + 2] photocycloaddition is shown in Fig. 2.55. The length of the side chain leads to a complete control of the regioselectivity of the [2 + 2] photocycloaddition is shown in Fig. 2.56 and in Fig. 2.57.

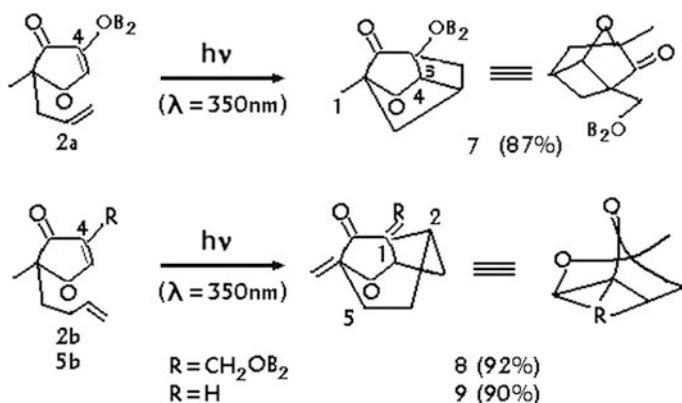


Fig. 2.56 The second example of intermolecular [2 + 2] photocycloaddition

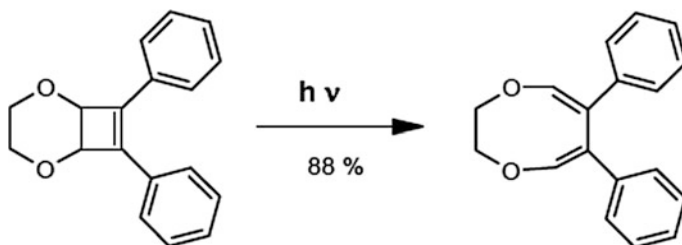


Fig. 2.57 The example of photoinduced electron transfer reactions with irradiation of 405 nm

2.7 Photoinitiation of Radical Reactions

In recent years, photoinitiated polymerization has received revitalized interest as it congregates a wide range of economic and ecological anticipations. For more than 30 years, photopolymerization has been the basis of numerous conventional applications in coatings, adhesives, inks, printing plates, optical wave-guides, and microelectronics. Some other less traditional but interesting applications, including production of optical disc and fabrication of 3D objects are also available. Many studies involving various photopolymerization processes have been continuously conducted in biomaterials for bones and tissue engineering, microchips, optical resins, and recoding media, surface relief gratings, anisotropic materials, polymeric photo-optical control materials, clay and metal nanocomposites, photoresponsive polymers, liquid crystalline materials, interpenetrated networks, microlens, multi-layers, surface modification, block and graft copolymerization, two-photon polymerization, spatially controlled polymerizations, topochemical polymerization, solid-state polymerization, living/controlled polymerization, interfacial polymerization, mechanistically different concurrent polymerizations, pulsed laser polymerization, polymerizations in microheterogenous media, and so forth. Interest has also grown in identifying the reactive species involved in the polymerization process by laser flash photolysis, time-resolved fluorescence and phosphorescence, and electron spin resonance spectroscopy as well as monitoring the polymerization itself by different methods including real-time IR spectroscopy, in-line NIR reflection spectroscopy, differential scanning calorimetry, in situ dielectric analysis, and recently developed optical pyrometry.

2.7.1 Photoinduced Electron Transfer Reactions

Photoinduced electron transfer reactions can be used to initiate radical reactions of alkenes. Both pathways, oxidative leading to a radical cation, and reductive, leading to a radical anion, are possible. The majority of reported examples involve oxidative pathway as Fig. 2.58, another example in Fig. 2.59.

1. Photoinduced cyclobutane ring opening

This reaction occurs in light dependent enzymatic DNA repair in bacteria. The enzymatic redox cofactor flavin is excited in its reduced form, transfers an electron onto the thymine cyclobutane dimer, which undergoes stepwise ring opening as radical anion. The electron is transferred back to the flavin and a new cycle can begin as shown in Fig. 2.60.

2. Alkene photocycloadditions in organic synthesis

Photochemical synthesis of a complex skeleton found in natural products. In contrast to simple homoallyl vinyl ethers, which have been shown to undergo

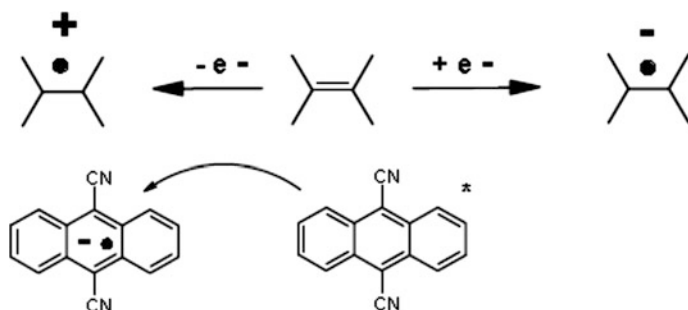


Fig. 2.58 Three examples of oxidative pathway

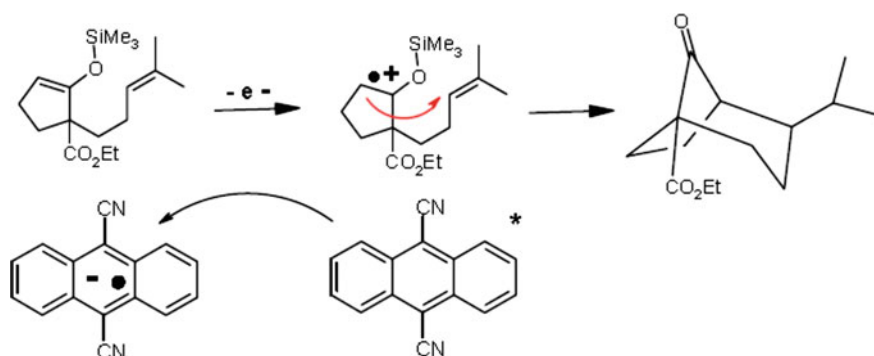


Fig. 2.59 Photooxidation of an enol silyl ether

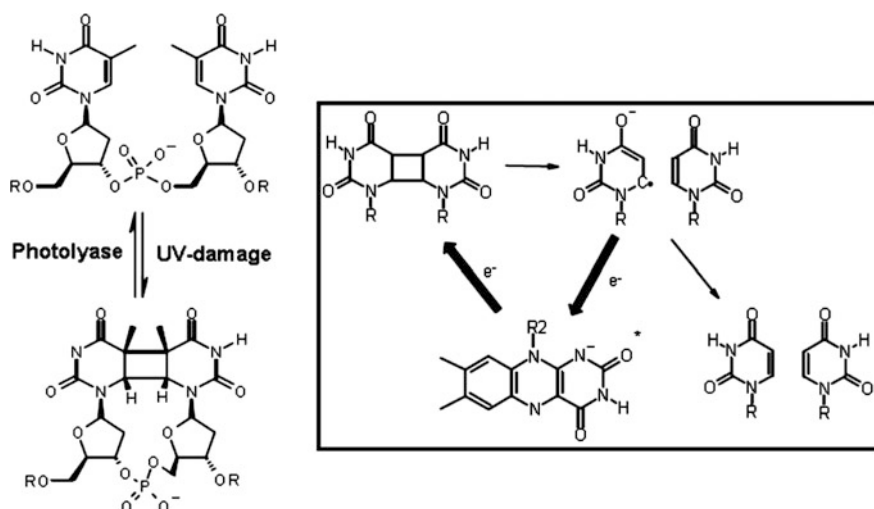
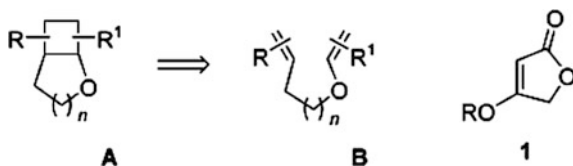


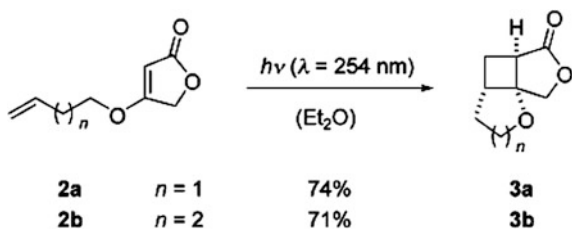
Fig. 2.60 The electron is transferred back to the flavin

Fig. 2.61 The photocycloaddition reactions

Cu-catalyzed [2 + 2] photocycloadditions, the more highly substituted substrates of type B do not react as desired, but decompose in the presence of the copper salts. As an alternative to enol ethers derivatives of tetronic acid (**1**, R=H) were tested in direct [2 + 2] photocycloaddition reactions as shown in Fig. 2.61. These building blocks deliver excellent results under irradiation conditions.

Synthesis of 2-oxabicyclo[3.2.0]heptanes by intramolecular [2 + 2] photocycloadd, tetronates of the general formula **2** are available from tetronic acid or its derivatives and alkenols by nucleophilic substitution. The intramolecular [2 + 2] photocycloaddition of the O-bridged dienes **2** proceeds smoothly yielding tetrahydrofuran **3a** and tetrahydropyran **3b** with excellent diastereoselectivity as photocycloaddition reactions as shown in Fig. 2.62. In each case, a single product is observed in diastereomerically pure form. The relative configuration was assigned by NOESY experiments and X-ray crystallographic analysis. The light source in the irradiation experiments was either a TNN 15/32 (Original Hanau, Heraeus Noblelight) low-pressure mercury arc or lamps of the type RPR-2437 Å (Rayonet).

Intramolecular [2 + 2] photocycloaddition of α -alkenyl tetronates, analogous experiments in acetone as the solvent or with a triplet sensitizer (benzophenone, acetophenone) in diethyl ether or acetonitrile were less successful and led to the formation of side products. The intramolecular photocycloaddition is not restricted by the position of the alkenyl side chain. In compound **4** the α -alkenyl chain is attached at C3, in compound **6** at C5. The cyclization of these substrates gives tricyclic products **5** (see Fig. 2.63) and **7** with high chemo-, regio-, and stereoselectivity. In all cases (Fig. 2.63 **3**, **5**, **7**), a single product was formed in which the cyclobutane ring and the annelated five- or six-membered rings are connected in a *cis* fashion. The facial diastereoselectivity in the reaction **6** to **7** can be understood as the attack of the terminal alkene to the face of the tetronate to which the alkyl chain is directed by the stereogenic center at C5 as shown in Figs. 2.63, 2.64 and 2.65.

Fig. 2.62 Tetronates of the general formula

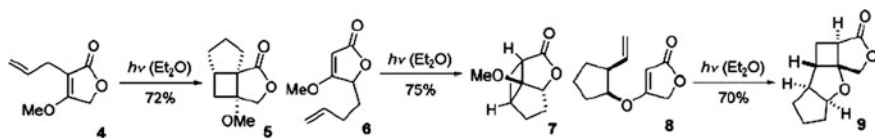


Fig. 2.63 Intramolecular [2 + 2] photocycloaddition of further substituted tetronates

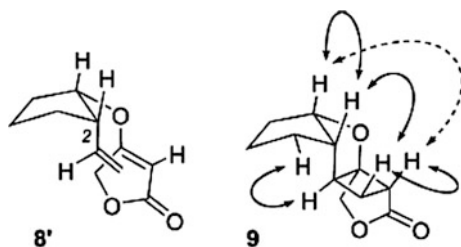


Fig. 2.64 Preferred conformation of compound 8 in the reaction to form 9 and NOESY contacts in the tetracyclic compound 9 (*dashed line* medium, *solid line* strong)

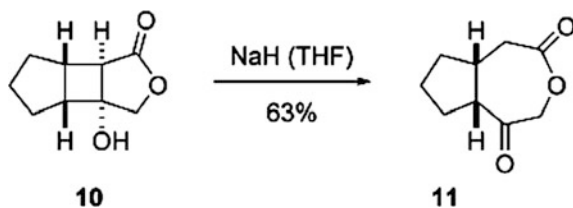


Fig. 2.65 Retroaldol reaction of the photocycloaddition product 10

The methodology was expanded to use the cyclobutane ring in the products for subsequent fragmentation reactions. A retroaldol reaction converts 10 into the ketolactone 11 upon treatment with a base.

2.7.2 Nitrogen-Containing Compounds

The presence of a nitrogen atom often alters the photophysical and photochemical properties of a given chromophore. Many nitrogen-containing compounds are much easier to oxidize than the corresponding nitrogen-free analogous. Aza-di- π -methane rearrangements as Fig. 2.66.

1. Decomposition of azo-compounds

As an alternative to heat or transition metal ions light can be used to generate carbenes from azo-compounds as Fig. 2.67.

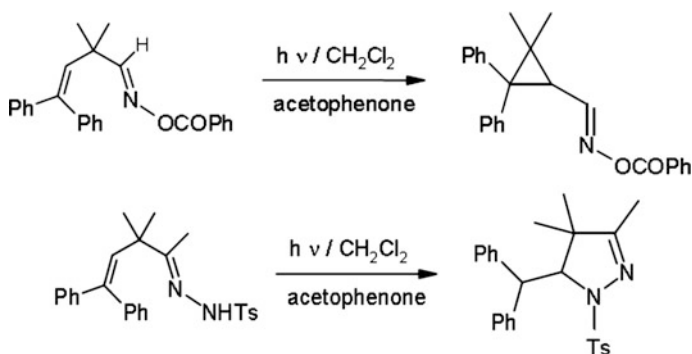


Fig. 2.66 Acetophenone is used as triplet sensitizer

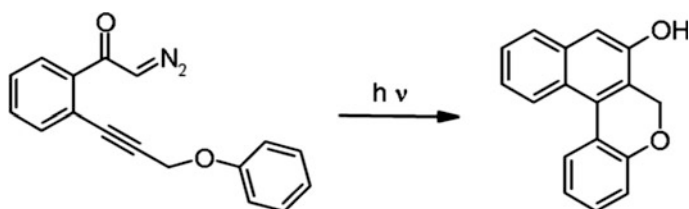


Fig. 2.67 Decomposition of azo-compounds

2. Aromatic compounds

The origin of reactivity of arenes (which are usually not very reactive) in the electronically excited state results from changes in the electron distribution. If benzene is irradiated with light of 254 nm small amounts for benzvalene and fulvene are formed. Upon irradiation with light of 203 nm formation of Dewar benzene is observed. Such isomerizations may be the initial steps of arene photoreactions as Figs. 2.68 and 2.69.

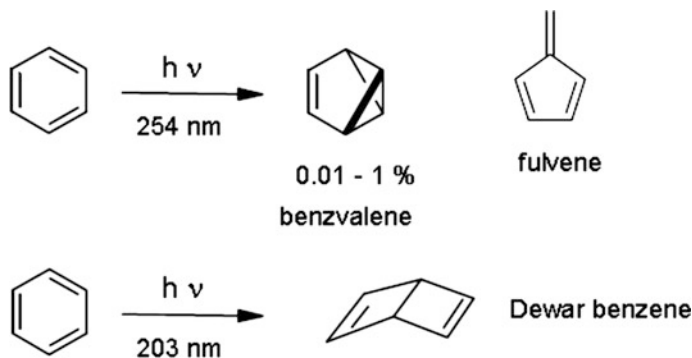


Fig. 2.68 The origin of reactivity of arenes

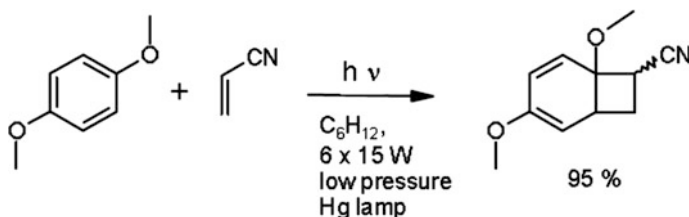


Fig. 2.69 Ortho-cycloaddition to benzene

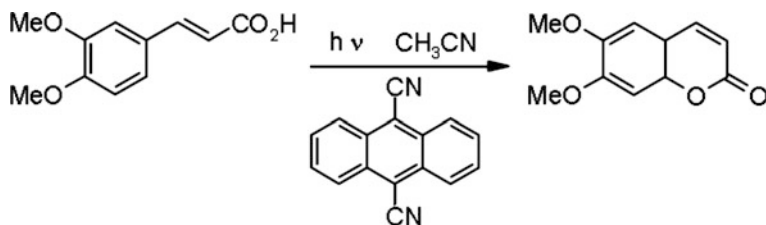


Fig. 2.70 Photoaddition by photooxidation: Synthesis of 6,7-dimethoxycoumarin Synthesis of 3-hydroperoxy-4-methyl-3-penten-2-ol

This is the photochemical key step of the synthesis of Pagodan. The photoreaction gives a mixture with about 30 % of the cyclization product. Laborious purification is necessary as Fig. 2.70.

2.7.3 Photooxygenation and Photoreduction

Singlet oxygen is an easily available reagent. It can be generated from triplet oxygen in many solvents by a broad variety of sensitizers. The reaction of organic compounds with singlet oxygen can lead to reactive molecules, such as hydroperoxides, 1, 2-dioxetanes, and endoperoxides. These compounds are useful for subsequent transformations. Examples as shown in Fig. 2.71.

TPP means tetraphenylporphyrin. The mechanism can be described as an ene-type reaction. In general the reactivity of an alkene is in this reaction increases with alkyl substitution, because an electrophilic reagent is attacking. Terminal

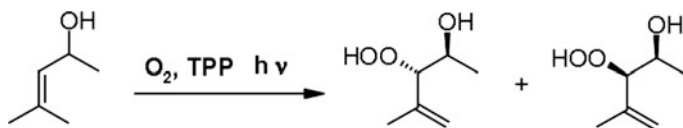


Fig. 2.71 Compounds are useful for subsequent transformations

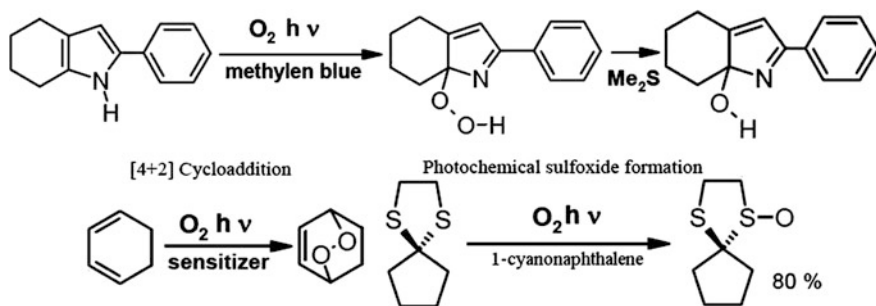


Fig. 2.72 The examples of two alkyl substituents vs one hydrogen and one alkyl substituent

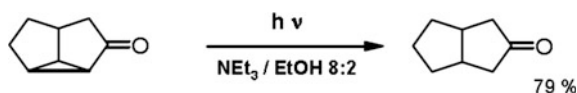


Fig. 2.73 The reduction of a strained bond in a tricyclic molecule. The irradiation is in a Rayonet photoreactor at 300 nm

alkenes usually do not react. If there is competition of several allyl positions for hydrogen abstraction, a general rule says that hydrogen abstraction occurs from the side of the double bond that is more substituted as Fig. 2.72.

Photoinduced electron transfer can lead to reduction processes, e.g. irradiation of the compound to be reduced in the presence of a sacrificial amine as electron donor. An example is the reduction of a strained bond in a tricyclic molecule as Fig. 2.73.

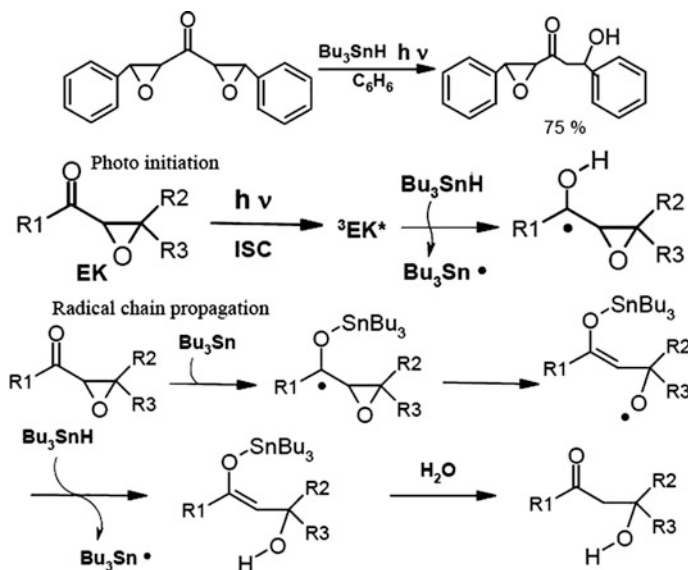


Fig. 2.74 An alternative reducing agent

An alternative reducing agent is tributyl tin hydride. The reductive epoxide opening is photochemically initiated and proceeds by a radical chain mechanism as Fig. 2.74.

2.7.4 Photochemistry in Organized Systems

The selectivity of photochemical reactions can increase if the environment in which the reaction occurs has a specific geometry. This can either be the case in the solid state. The best known example is the [2 + 2] photocycloaddition of cinamic acid, which gives many isomers in solution, while irradiation of a crystal leads to fewer products. However, photochemistry in the solid state is difficult to predict in many cases. Therefore, modern approaches focus on topological reaction control in solution using templates to which the reactants are covalently or non-covalently bound as Fig. 2.75.

Photochemical reaction within a hydrogen-bonded aggregate is shown in Figs. 2.76 and 2.77.

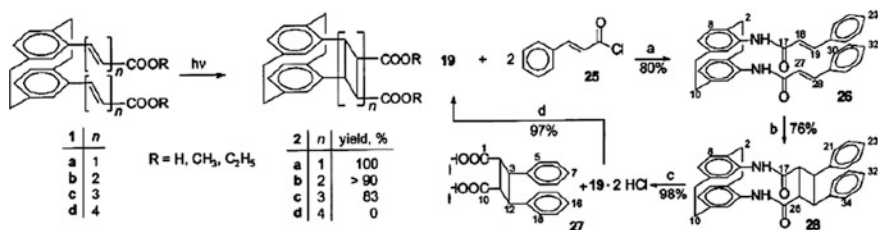


Fig. 2.75 Examples of Topochemical reaction control of [2 + 2] cycloadditions in solution. Compound 19 is a [2.2] paracyclophane-diamine

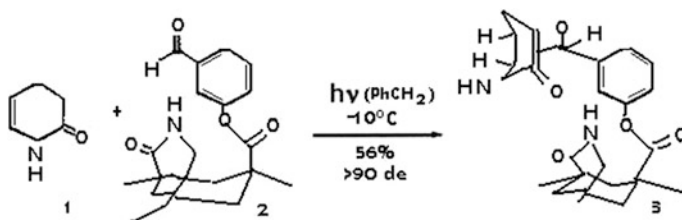


Fig. 2.76 The intra-assembly

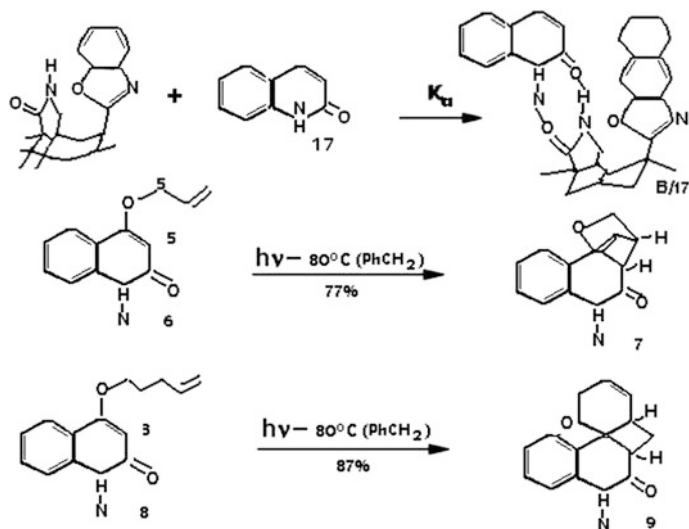


Fig. 2.77 Catalytic with template molecule: Enantioselective Norrish–Yang cyclization on a chiral template

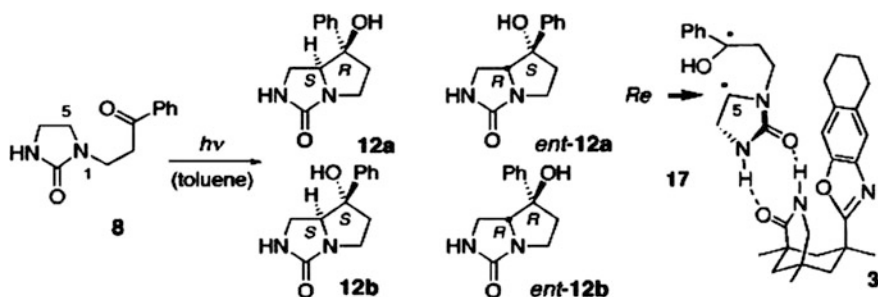


Fig. 2.78 The stereoisomers of the reaction compound 12a

From all possible stereoisomers of the reaction compound 12a was formed preferentially if the reaction was performed in the presence of the chiral template as Figs. 2.78 and 2.79.

2.7.5 Photochromic Compounds

Photochromism characterizes reversible reactions in which one or both directions of the process can be triggered photochemically. The absorption spectra of starting material and product differ with respect to absorption wavelength and extinction;

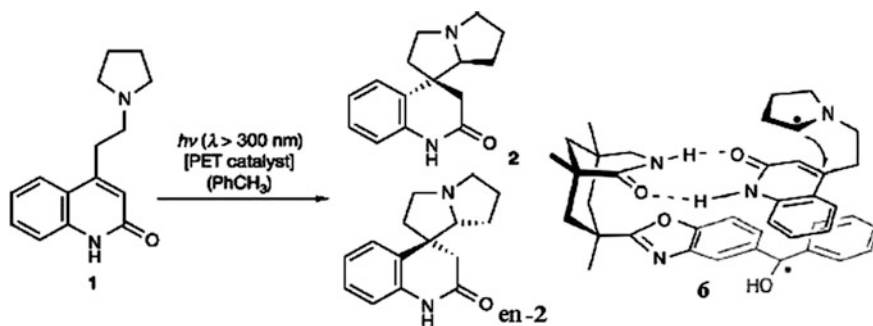


Fig. 2.79 Enantioselective catalytic PET-induced cyclization reaction

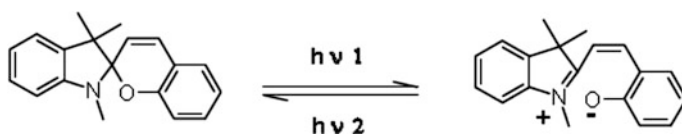


Fig. 2.80 Photochromic switches

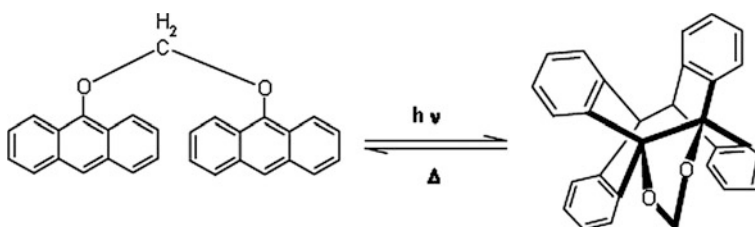


Fig. 2.81 Close: high-pressure Hg lamp in Pyrex. Open: heat diethyl ether solution with hairdryer for 15 min

therefore each process can be addressed more or less selectively. Photochromic switches can be regarded as a simple way of information storage. Many examples involve charge separation that leads to a different electronic structure with different absorption properties. The spiropyran—merocyanine dye system is one of the classics as Fig. 2.80.

The photodimerization of tethered anthracene has found to be thermally reversible by simple heating in diethyl ether is shown in Fig. 2.81.

The spiro compound—betaine switch is shown in Fig. 2.82.

The dithienylethylene allows reversible switching with UV and visible light is shown in Fig. 2.83.

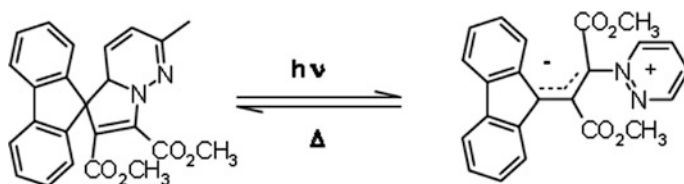


Fig. 2.82 Spiro compound—betaine switch Irradiation with visible light; half-life of the betaine at 20 °C: 14.4 min

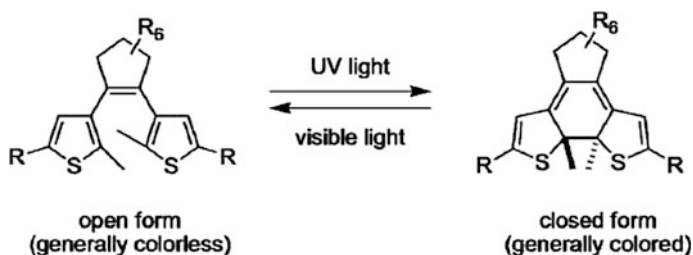


Fig. 2.83 The dithienylethylene allows reversible switching with UV and visible light. These switches can show (depending on R)

2.7.6 Photocleavable Protecting Groups and Linkers

The protecting groups as the norrish type II: ortho-nitrobenzyl alcohols is shown in Fig. 2.84.

For amino acids and heterocycles of protecting groups is shown in Fig. 2.85. For nucleic acids and sugars is shown in Fig. 2.86.

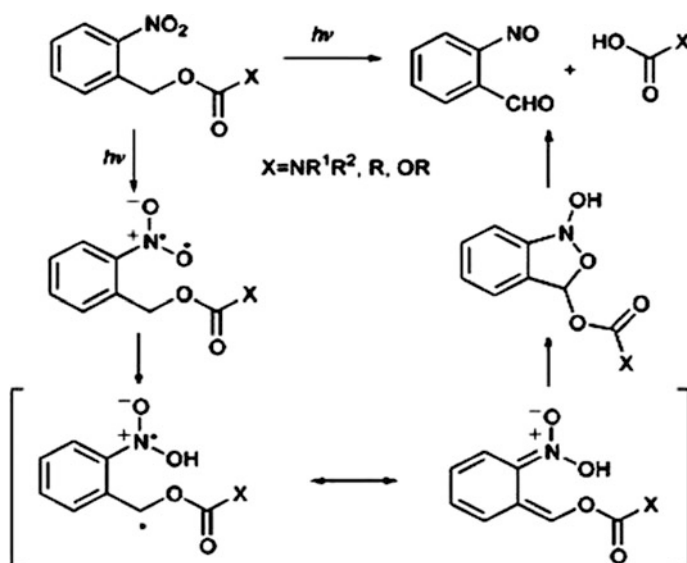


Fig. 2.84 The norrish type II: ortho-nitrobenzyl alcohols

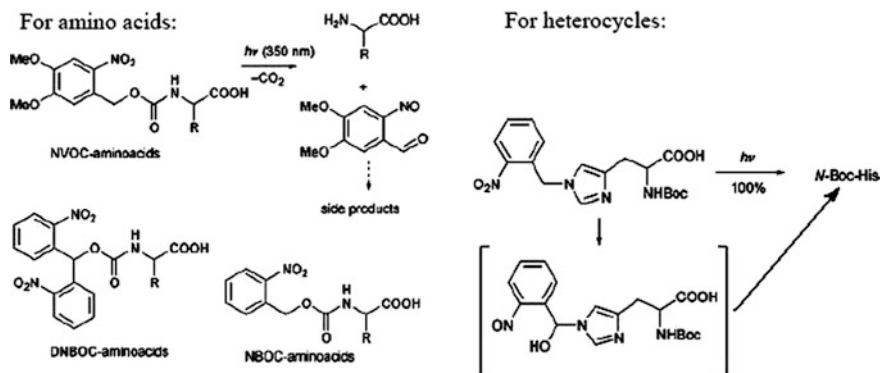


Fig. 2.85 For amino acids and heterocycles

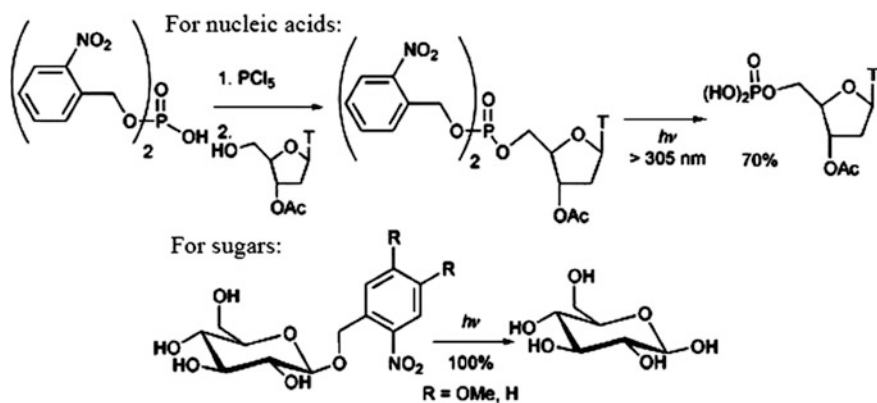


Fig. 2.86 For nucleic acids and sugars of protecting groups

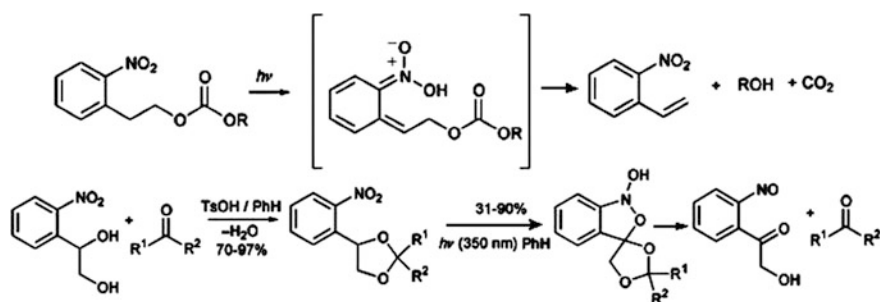


Fig. 2.87 The functional group to be protected is linked in β -position and protecting group for ketones

Different reaction pathway if functional group to be protected is linked in β -position and protecting group for ketones is shown in Fig. 2.87.

The PET example: Benzophenone as oxidant is shown in Fig. 2.88.

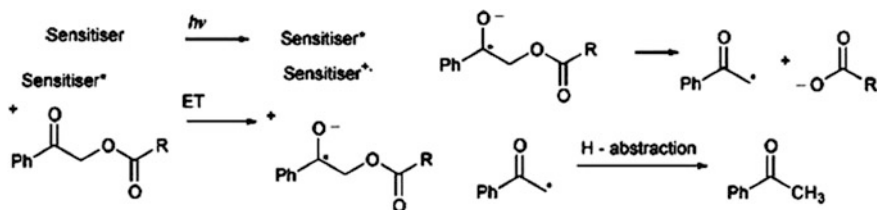


Fig. 2.88 Photoinduced electron transfer—Benzophenone as oxidant

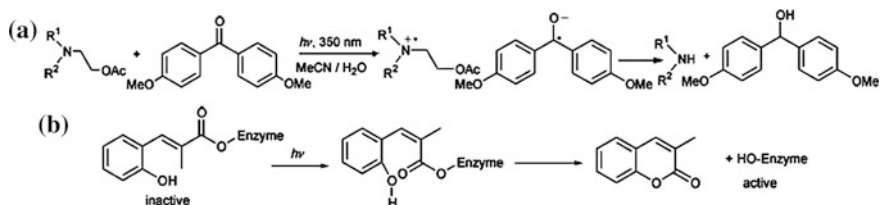


Fig. 2.89 **a** photodeprotection of an amine by wavelength of 350 nm light, **b** photoisomerization of *cis-trans*

The Photodeprotection of an amine (a) and the photoisomerization: *cis-trans* (b) is shown in Fig. 2.89.

2.8 Insertion Rate and Effective Capacity of Multidimensional Storage

Whether magnetic and optical data storage systems required constrained modulation codes also. These codes transform in a lossless manner, streams of arbitrary binary data into binary sequences that satisfy certain prescribed constraints. The set of words from which the code sequences may be drawn is referred to as a constrained system or simply a constraint. A constraint is characterized by a finite directed labeled graph, the paths of which generate the words in the set. These systems was initiated by Shannon who defined the capacity of a constrained system S as

$$\text{cap}(S) = \limsup_{n \rightarrow \infty} \frac{\log_2 |S(n)|}{n}, \quad (2.41)$$

where $S(n)$ denotes the number of sequences of S of length exactly n . Shannon showed that whenever there is a rate $p:q$ encoder (that is, an encoder which generates on average q output symbols for every p input bits) of a constrained system, then must have $p/q \leq \text{cap}(S)$. Furthermore, this bound is tight. The definition of

constraint and capacity generalizes to higher-dimensional constraints. If S denotes a 2D constraint and $S(m, n)$ denotes the set of $m \times n$ arrays in S , and then

$$\text{cap}(S) = \limsup_{m, n \rightarrow \infty} \frac{\log_2 |S(m, n)|}{mn}. \quad (2.42)$$

So the insertion rate and effective capacity is an important research goal for multidimensional optical storage. The corresponding coding, error-correcting code, maximum insertion rate and capacity have been proposed. Typically in digital storage systems source data is encoded twice before written to the medium. First an error-correcting code (or ECC) encodes the source data into a codeword, and then a constrained (or modulation) code is used to transform the codeword into a sequence of bits that can be written reliably to the device. When reading back the data the process is reversed. As the decoder for the constrained code is typically a hard decoder, this scheme has the disadvantage of not making soft information available to the ECC decoder, thereby, limiting its error correction capability. A reverse concatenation scheme is considered where the user bits are first transformed into a constrained sequence in which certain entries are left unconstrained—i.e., filling them with any combination of bits would result in a sequence satisfying the constraint. Then, a systematic ECC of suitable rate is applied, placing the redundancy (parity-check) bits in these unconstrained positions. Since the error correction capability of the ECC depends on the number of redundancy bits, it is desirable that the number of unconstrained positions be as large as possible. On the other hand, increasing the number of unconstrained positions naturally reduces the rate of the constrained encoder. The tradeoff function defines for a given “density” of unconstrained positions the maximum rate of the constrained encoder. They also define the maximum insertion rate as essentially the largest asymptotic density of unconstrained positions possible for the constrained code. Extend some of these ideas to multidimensional constrained systems. Defined the maximum insertion rate of a multidimensional constraint and show that, for isotropic constraints, it is equal to the maximum insertion rate of the underlying one-dimensional constraint. The maximum insertion rate of an isotropic constraint is a lower bound on the limiting value of the capacity as the number of dimensions goes to infinity. Finally, that for isotropic constraints, whose underlying one-dimensional constraint has finite memory, when the maximum insertion rate is zero, the capacity decreases to zero exponentially fast as the number of dimensions goes to infinity [20–22].

2.8.1 *Multidimensional Constraints with Unconstrained Positions*

Multidimensional constraints given a finite directed graph whose edges are labeled with symbols from some finite alphabet, each path in the graph corresponds to a

finite word attained by reading the labels of the edges of the path in sequence. The path is said to generate the word, and the set of all such generated words is a one-dimensional constrained system or a one-dimensional constraint. The graph is a presentation of the constraint, and its vertices are usually called states and edges, transitions. An example of a one-dimensional constrained system, commonly found in magnetic and optical storage systems, is the (d, k) -run length limited constraint, denoted by $\text{RLL}(d, k)$, for nonnegative integers $d \leq k$. This is the set of all binary words that contain at least d zeros between pairs of adjacent '1's and do not contain more than k consecutive '0's anywhere. The k parameter is allowed to be ∞ which signifies no upper bound on the length of a run of zeros.

Consider multidimensional constraints of dimension D , constructed from one-dimensional constraints, by requiring that all the "rows," in a given direction, of a D -dimensional array satisfy a one-dimensional constraint. More precisely, fix a finite alphabet Σ and positive integer D . For a D -tuple $\mathbf{m} = (m_1, \dots, m_D)$ of positive integers, let Γ be a D -dimensional $m_1 \times m_2 \times \dots \times m_D$ array of symbols of Σ whose entries are indexed an array a D -dimensional array of size \mathbf{m} , as:

$$\mathbf{j} \in \{0, \dots, m_1 - 1\} \times \{0, \dots, m_2 - 1\} \times \dots \times \{0, \dots, m_D - 1\}, \quad (2.43)$$

where

$$D\text{-tuples } (m_i^{(1)}, \dots, m_i^{(D)})_{i=1}^\infty, (m_i^{(j)})_{i=1}^\infty, \quad j = 1, 2, \dots, D. \quad (2.44)$$

Given an integer $1 \leq i \leq D$, a row in direction i of Γ is a sequence of entries of Γ of the form

$$(\Gamma_{k_1, k_2, \dots, k_{i-1}, j, k_{i+1}, \dots, k_D})_{i=0}^{m_i-1} \quad 0 \leq k_l \leq m_l - 1; \quad 1 \leq l \leq D, l \neq i. \quad (2.45)$$

where Γ satisfies a (one-dimensional) constraint in direction i , if every row in direction i of the array belongs to the constraint. Let Σ^m denote all D -dimensional arrays of size \mathbf{m} over Σ , and define $\Sigma^{*****} = \Sigma^{*D}$, where the number of $*$'s in the superscript is D , as the union of Σ^m over all such D_m ; that is, Σ^{*D} is the set of all finite-size D -dimensional arrays. Deal with subsets of Σ^{*D} defined in the following manner. Let S_1, \dots, S_D be D (one-dimensional) constraints over Σ . Denote by $S_1 \otimes S_2 \otimes \dots \otimes S_D$ the set of finite D -dimensional arrays satisfying the constraint S_i in direction i ; $i = 1, 2, \dots, D$. A D -dimensional constrained system or D -dimensional constraint, and by saying that a D -dimensional array satisfies the constraint we mean that it belongs to the constraint. Often $S_1 = S_2 = \dots = S_D = S$, in which case the constraint $S_1 \otimes \dots \otimes S_D$ is called isotropic (or symmetric in some papers) and abbreviate it by $S^{\otimes D}$. Let S be a D -dimensional binary constrained system. For a D_m $\mathbf{m} = (m_1, \dots, m_D)$, denote by $N(S, \mathbf{m})$ the number of D -dimensional $m_1 \times m_2 \times \dots \times m_D$ arrays satisfying S , and define

$$\mathcal{M}(S, \mathbf{m}) = (\log \mathcal{N}(S, \mathbf{m})) / \prod_{i=1}^D m_i,$$

where the base of the logarithm is 2 and take $\log(0)$ to be $-\infty$. The capacity of S , denoted $\text{cap}(S)$, is defined by

$$\text{cap}(S) = \lim_{m \rightarrow \infty} \mathcal{M}(S, \mathbf{m}_i), \quad (2.46)$$

i.e.

$$\text{cap}(S) = \inf_{\mathbf{m}} \mathcal{M}(S, \mathbf{m}). \quad (2.47)$$

where $(m_i)_{i=1}^\infty$ is a sequence of D -tuples diverging to infinity. Since $\log \mathcal{N}(S)$ is sub-additive, the above limit exists, is independent of the choice of $(m_i)_{i=1}^\infty$ and satisfies [23, 24].

2.8.2 Unconstrained Positions and the Maximum Insertion Rate

Restrict to the binary alphabet and set $\Sigma = \{0, 1\}$. Let $\widehat{\Sigma}$ denote the extended alphabet, $\{0, 1, \Psi\}$, and let m be a D -tuple of positive integers. For a D -dimensional array $\Gamma \in \widehat{\Sigma}^m$ with ‘0’s, ‘1’s, and ‘ Ψ ’s, define the set of all fillings of Γ by, $\Phi(\Gamma) = \{\Delta \in \Sigma^m : \text{for every index } j, \text{ if } \Gamma_j \neq \Psi \text{ then } \Delta_j = \Gamma_j\}$; thus $\Phi(\Gamma)$ contains all the (binary) arrays attained by filling every ‘ Ψ ’ of Γ with ‘0’ or ‘1’ independently. Next we define, the set \widehat{S} of D -dimensional arrays with entries in $\widehat{\Sigma}$ by,

$$\widehat{S} = \{\Gamma \in \widehat{\Sigma}^{*D} : \Phi(\Gamma) \subseteq S\}, \quad (2.48)$$

thus \widehat{S} contains all the arrays over $\widehat{\Sigma}$ such that every filling of the ‘ Ψ ’s by ‘0’s and ‘1’s results in an array that satisfies S . If S is a binary one-dimensional constraint, shows how to construct a presentation for \widehat{S} . Thus, \widehat{S} is a one-dimensional constrained system. If $S = S \otimes \dots \otimes S_D$ for some D one-dimensional constraints S_1, \dots, S_D , then it is easily verified that $\widehat{S} = \widehat{S}_1 \otimes \dots \otimes \widehat{S}_D$, and hence \widehat{S} is a D -dimensional constraint as well. For a binary constrained system S , its maximum insertion rate is the maximal asymptotic density of ‘ Ψ ’s in arrays of \widehat{S} when the array size approaches infinity. More precisely, given an array $\Gamma \in \Delta \Sigma \Psi D$, let $\rho(\Gamma)$ denote the density of ‘ Ψ ’s in Γ , that is the ratio of the number of ‘ Ψ ’s to the total number of symbols in Γ . Define the maximum insertion rate of S , denoted $\mu(S)$, by

$$\mu(S) = \sup_{(\Gamma_i)_{i=1}^\infty \subseteq \widehat{S}} \limsup_{i \rightarrow \infty} \rho(\Gamma_i), \quad (2.49)$$

where the sup above is taken over all sequences of D -dimensional arrays in \widehat{S} whose corresponding sequence of sizes diverges to infinity. For a binary one-dimensional constraint, S , let \widehat{G} be a presentation for \widehat{S} . The density of squares in a path of G is the ratio of the number of edges in the path labeled with a ‘ Ψ ’, to the total number of edges in the path. It is shown that $\mu(S)$ is equal to the maximum density of ‘ Ψ ’s in a simple cycle of \widehat{G} , and is rational therefore. Additionally, it is shown that the maximum insertion rate of the RLL constraints is given by

$$\mu(\mathbf{RLL}(d, k)) = \frac{\left\lfloor \frac{k-d}{d+1} \right\rfloor}{\left\lfloor \frac{k+1}{d+1} \right\rfloor (d+1)} \quad (2.50)$$

$$\text{i.e. } \mu(\mathbf{RLL}(d, \infty)) = \frac{1}{d+1}, \quad (2.51)$$

for nonnegative integers $d \leq k$.

For multidimensional isotropic constraints constructed from a one-dimensional constraint S , it is somewhat surprising that the maximum insertion rate remains the same. This is stated in the following theorem:

$$\begin{aligned} \mu(S) &\leq \min\{\mu(S_1), \dots, \mu(S_D)\} \\ S_1 = \dots = S_D = T &\text{ then } \mu(S) = \mu(T) \end{aligned} \quad (2.52)$$

Since the maximum insertion rate of a one-dimensional constraint can be computed from a presentation of \widehat{S} . Let S be a one-dimensional constraint as:

$$\text{cap}_\infty(S) \geq \mu(S). \quad (2.53)$$

That for $S = \mathbf{RLL}(d, \infty)$, Eq. (2.53) holds with equality. This is also true for one-dimensional constraints S with maximum insertion rate zero and finite memory. This follows from the next theorem. A labeled graph G has finite memory m , if all paths of length m , generating the same word, terminate at the same vertex of G . A one-dimensional constraint has finite memory if it has a presentation with finite memory. The memory of such a constraint is the smallest memory of its finite memory presentations.

Let S be a one-dimensional constraint with finite memory m . If $\mu(S) = 0$ for all positive integers D ,

$$\text{cap}(S^{\otimes(D+1)}) \leq \frac{m}{m+1} \text{cap}(S^{\otimes D}). \quad (2.54)$$

In particular $\text{cap}_\infty(S) = 0$. Consider the constraint $\text{RLL}(d, k)$ has memory k , and by Eqs. (2.50) and (2.51), $\mu(\text{RLL}(d, k)) = 0$ if and only if $k \leq 2d$. Thus we can obtain the following results:

1. When d, k be nonnegative integers such that $d \leq k$. Then $\text{cap}_\infty(\text{RLL}(d, k)) = 0$ if and only if $k \leq 2d$. Another constraints found in magnetic and optical recording, is the multiple-spaced run length constraints denoted $\text{RLL}(d, k, s)$. These are characterized by nonnegative integers d, k, s with $d \leq k$. A binary word satisfies $\text{RLL}(d, k, s)$ if it satisfies $\text{RLL}(d, k)$ and the length of each run of zeros is a multiple of s . A storage system is employing the $\text{RLL}(2, 18, 2)$.
2. When d, k, s be nonnegative integers such that $d \leq k$ and $s > 1$. Then

$$\text{cap}(\mathbf{RLL}(d, k, s)^{\otimes D}) \leq \left(\frac{k}{k+1} \right)^{D-1} \text{cap}(\mathbf{RLL}(d, k, s)). \quad (2.55)$$

If $1 \leq j \leq D$ be an integer such that $\mu(S_j) = \min\{\mu(S_1), \dots, \mu(S_D)\}$. Fix a positive real number ϵ , and let $(\Gamma_i)_{i=1}^\infty \subseteq \Psi\hat{S}$ be a sequence of D -dimensional arrays with sizes diverging to infinity, such that

$$\limsup_{i \rightarrow \infty} \rho(\Gamma_i) \geq \mu(S) - \epsilon. \quad (2.56)$$

For a positive integer i , consider the set of rows in direction j of Γ_i . Since $\rho(\Gamma_i)$ is the average of the densities of Ψ 's in these rows, there exist a row with density of squares at least $\rho(\Gamma_i)$. Let z_i be such a row. Clearly $z_i \in \hat{S}_j$, and therefore

$$\mu(S_j) \geq \limsup_{i \rightarrow \infty} \rho(z_i) \geq \limsup_{i \rightarrow \infty} \rho(\Gamma_i) \geq \mu(S) - \epsilon. \quad (2.57)$$

Since ϵ is arbitrary, that have $\mu(S_j) \geq \mu(S)$. Fix a presentation \hat{G} for \hat{T} , and let $w = w_0 \dots w_{n-1}$ be a word in \hat{T} generated by a cycle of \hat{G} with density of Ψ 's equal to $\mu(T)$. For each positive integer i , let Γ_i be the D -dimensional array of size with entries given by

$$(\Gamma_i)_{(m_1, m_2, \dots, m_D)} = \mathcal{W}_{(m_1 + m_2 + \dots + m_D) \bmod n}. \quad (2.58)$$

Then every row (in any direction) of Γ_i is a cyclic shift of i concatenations of ω , and in \hat{T} . Thus, $(\Gamma_i)_{i=1}^\infty \subseteq \hat{S}$ and $\rho(\Gamma_i) = \mu(T)$, for $i = 1, 2, \dots$. It follows that $\mu(S) \geq \mu(T)$.

For any D -dimensional constraint S , $\text{cap}(S) \geq \mu(S)$, that is $\text{cap}(S^{\otimes D}) \geq \mu(S^{\otimes D}) = \mu(S)$ for any positive integer D . Taking the limit as $D \rightarrow \infty$,

let ϵ be a positive real number and let $(\Gamma_i)_{i=1}^\infty \subseteq \widehat{S}$ be a sequence of D -dimensional arrays, with sizes diverging to infinity, satisfying $\limsup_{i \rightarrow \infty} \rho(\Gamma_i) \geq \mu(S) - \epsilon$. Denote by m_i the size of Γ_i , and by n_i the product of entries in m_i (i.e., n_i is the number of symbols in Γ_i). Since each of the $2^{\rho(\Gamma_i)n_i}$ ways of replacing the ‘ Ψ ’s in Γ_i by ‘0’s and ‘1’s results in a distinct array of S , that $M(S, m_i) \geq \rho(\Gamma_i)$, and consequently as ϵ is arbitrary

$$\text{cap}(S) = \lim_{i \rightarrow \infty} \mathcal{M}(S, \mathbf{m}_i) \geq \limsup_{i \rightarrow \infty} \rho(\Gamma_i) \geq \mu(S) - \epsilon. \quad (2.59)$$

If S is irreducible, i.e., has an irreducible (strongly connected) presentation. Need the following definition. Let $\Sigma = \{0, 1\}$. For a word $\omega \in \Sigma^*$ denote by $|\omega|$ the number of symbols (length) in ω . To one-dimensional constrained system S , (m, a) -determined, for nonnegative integers m and a , if there do not exist two words $x0y, x1y \in S$, such that $|x| = m$ and $|y| = a$. Thus, if ω is a word of an (m, a) -determined constraint, then each symbol placed sufficiently far from the beginning and end of ω is uniquely determined by its m preceding symbols and a succeeding symbols. Now, let S be a general one-dimensional constraint. If $\mu(S) > 0$, then, since there exist arbitrarily long words $x, y \in \Sigma^*$ such that $x, y \in \widehat{S}$, it follows that S is not (m, a) -determined for any nonnegative integers m . Let S be an irreducible one-dimensional constrained system with finite memory m . If $\mu(S) = 0$ then S is (m, m) -determined. Assume to the contrary that there exist two words $x0y, x1y \in S$, where x, y are binary words of length m . Let $\alpha_0 \rightarrow \alpha_1 \rightarrow \dots \rightarrow \alpha_{2m+1}, \beta_0 \rightarrow \beta_1 \rightarrow \dots \rightarrow \beta_{2m+1}$ be the paths in G generating $x0y, x1y$, respectively, where $\alpha_0, \dots, \alpha_{2m+1}, \beta_0, \dots, \beta_{2m+1}$ are states in G . Since G has memory m , it follows that $\alpha_m = \beta_m$ and $\alpha_{2m+1} = \beta_{2m+1}$. Since G is irreducible there exists a path $\alpha_{2m+1} \rightarrow \gamma_1 \rightarrow \gamma_2 \rightarrow \dots \rightarrow \gamma_{l-2m}$ connecting α_{2m+1} to α_m , and generating some word z . Therefore, G contains the cycles $\alpha_m \rightarrow \alpha_{m+1} \rightarrow \dots \rightarrow \alpha_{2m+1} \rightarrow \gamma_1 \rightarrow \dots \rightarrow \gamma_{l-2m} \rightarrow \alpha_m$ and $\alpha_m = \beta_m \rightarrow \beta_{m+1} \rightarrow \dots \rightarrow \beta_{2m+1} \rightarrow \gamma_1 \rightarrow \dots \rightarrow \gamma_l \rightarrow \beta_{m=2m}$, that generate the words $0yz$ and $1yz$, respectively. Consequently, for any finite sequence of bits $b_1, b_2, \dots, b_i \in \Sigma$, the word $b_{1yz}b_{2yz} \dots b_{iyz} \in S$. Hence, $(\Psi_{yz})_i \in \widehat{S}$, for all positive integers i , contradicting the assumption that $\mu(S) = 0$. If S is an (m, a) -determined constraint, the capacity of $S^{\otimes D}$ decreases at least exponentially fast with D . This is a generalization where $S = \text{RLL}(d, k)$ with $k \leq 2d$ and for general (m, a) -determined constraints as well. If S be a one-dimensional (m, a) -determined constraint, for all positive integers D , then

$$\text{cap}(S^{\otimes(D+1)}) \leq \frac{b}{b+1} \text{cap}(S^{\otimes D}), \quad (2.60)$$

where $b = \min\{m, a\}$.

For the case $b = a$. The case $b = m$ is handled similarly. Let l be a positive integer. Denote by l the D -tuple with every entry equal to l , and let m_l be the $(D+1) - e$ given by $m_l = (m + l(a+1), l, l, \dots, l)$. That $N(S^{\otimes D}, m_l)$ is the number

of arrays in $S^{\otimes D+1}$ of size ml bound $N(S^{\otimes(D+1)}, m_l)$ from above. For an array Γ of size ml and integer $0 \leq i < m + l(a+1)$, denote by $\Gamma^{(i)}$ the D -dimensional sub-array of Γ of size l , consisting of the entries Γ_{ij} ; $j \in \{0, 1, \dots, l-1\}D$. Let $i_r = m + r(a+1)$; $r = 0, 1, \dots, l-1$, can set

$$A = \{0, 1, \dots, m + l(a+1) - 1\} \setminus \{i_r : r = 0, \dots, l-1\}. \quad (2.61)$$

For each array Γ of size ml in $S^{\otimes(D+1)}$, each of the sub-arrays $\Gamma^{(i)}$ satisfies $S^{\otimes D}$. construct all such arrays Γ by first selecting the sub-arrays $\Gamma^{(k)}$; $k \in A$ —each chosen from the set of arrays of size l in $S^{\otimes D}$ and then completing the entries of the sub-arrays $\Gamma^{(ir)}$; $r = 0, 1, \dots, l-1$, that for each possible choice of the sub-arrays $\Gamma^{(k)}$; $k \in A$ there is at most one possibility to complete the sub-arrays $\Gamma^{(ir)}$; $r = 0, 1, \dots, l-1$ such that the resulting array Γ satisfies $S^{\otimes(D+1)}$. For $j \in \{0, 1, \dots, l-1\}D$, consider the sequence of entries $\Gamma_j^{(0)}, \Gamma_j^{(1)}, \dots, \Gamma_j^{(m+l(a+1)-1)}$. It is a row in direction 1 of Γ , and contains the yet unselected entries: $\Gamma_j^{(i0)}, \dots, \Gamma_j^{(il-1)}$.

Complete these entries in sequence. The entry $\Gamma_j^{(i0)}$ is preceded by m , already selected, entries in the row and succeeded by a , already selected, entries in the row. Thus, since S is (m, a) -determined, there is at most one possibility to complete it. For $r \geq 1$, after completing the entries $\Gamma_j^{(ik)}$, for $0 \leq k < r$ the entry $\Gamma_j^{(ir)}$ is preceded by (at least) m completed entries in the row, and succeeded by a completed entries in the row. There is at most one possibility to complete it. Therefore, for each selection of the sub-arrays $\Gamma^{(k)}$; $k \in A$ there is at most one possibility to complete the rest of Γ so that the resulting array satisfies $S^{\otimes(D+1)}$. Since there are $N(S^{\otimes D}, l)^{m+la}$ ways to select the sub-arrays $\Gamma^{(k)}$; $k \in A$, it follows that $N(S^{\otimes(D+1)}, ml) \leq N(S^{\otimes D}, l)m + la$. Hence,

$$\begin{aligned} \mathcal{M}(S^{\otimes(D+1)}, m_l) &= \frac{\log \mathcal{N}(S^{\otimes(D+1)}, m_l)}{l^D(m + l(a+1))} \\ &\leq \frac{(m + la) \log \mathcal{N}(S^{\otimes D}, 1)}{l^D(m + l(a+1))} \\ &= \frac{m + la}{m + l(a+1)} \mathcal{M}(S^{\otimes D}, 1) \end{aligned} \quad (2.62)$$

Taking the limit is as $l \rightarrow \infty$, can obtain the result.

Let S be an irreducible one-dimensional constraint with finite memory m . S is (m, m) -determined. A reducible constraint with finite memory and $\mu(S) = 0$ need not be (m, a) -determined for any m and a . For example, consider the constraint S consisting of all sequences of the form $0^u 1^v$ where u, v are arbitrary nonnegative integers. This constraint is presented by a graph with two states a, b , a self loop labeled 0 at a , an edge from a to b labeled 1, and a self loop at b labeled 1. This presentation has finite memory, but S is reducible since a 0 can never follow a 1. And $\mu(S) = 0$ since any string in \hat{S} can contain at most one (at a transition from 0 to 1).

But S is not (m, a) determined for any m, a since $0^m \times 1^a$ can be filled in by $x = 0$ or $x = 1$. There can be much more complicated constraints with these features.

If S be any one-dimensional constraint with finite memory m and $\mu(S) = 0$. For each sequence x in S and positive integer N , let $V_N(x)$ be the set of sequences y in S such that $y_i = x_i$ whenever i is not divisible by N . By using the general structure of reducible graphs one can show that $|V_{m+1}(x)|$ is uniformly bounded over all x in S .

The maximum insertion rate of a constraint is a lower bound on its capacity, a simple upper bound on the maximum insertion rate for a constrained system. For isotropic D -dimensional constraints, it turns out that the maximum insertion rate is equal to the maximum insertion rate of the underlying one-dimensional constraint. For such constraints, the maximum insertion rate provides a lower bound on the limiting value of the capacity as the number of dimensions grows to infinity. That for isotropic constraints with maximum insertion rate 0, in which the underlying one-dimensional constraint has finite memory, the limiting value of the capacity is in fact 0 and the rate of convergence is exponential [25–27].

References

1. J. Song, D.-Y. Xu, G.-S. Qi, Multilevel read-only optical recording methods. *Chin. Phys.* **15** (8), 1788–1792 (2006)
2. N.S. Allen, J.F. Rabek (eds.), *New Trends in the Photochemistry* (New York, 2007)
3. V. Balzani, P. Ceroni, A. Juris, *Photochemistry and Photophysics: Concepts, Research, Applications* (Wiley, New York, 2014)
4. N.J. Turro, J.C. Scaiano, *Modern Molecular Photochemistry of Organic Molecules* (New York, 2010)
5. A. Albini, *Photochemistry* (Research Press, Champaign, 2011)
6. T. Tümkür, et al., Control of Förster energy transfer in vicinity of metallic surfaces and hyperbolic metamaterials. *Faraday Discuss. F.D.* **178** (2014)
7. B. Lebeau, C. Marichal, A. Mirjöl, G.J.A.A. de Soler-Illia, R. Buestrich, M. Popall, L. Mazerolles, C. Sanchez, Synthesis of highly ordered mesoporous hybrid silica from aromatic fluorinated organosilane precursors. *New J. Chem.* **27**, 166 (2003)
8. J. Feldhaus, K. Dardis, H. Kavanagh, J. Luna, Pedregosa Gutierrez, Single-shot characterization of independent femtosecond extreme ultraviolet free electron and infrared laser pulses. *App. Phys. Lett.* **90**, 131108 (2007)
9. J.Y. Bae, O.H. Park, J.I. Jung, K.T. Ranjit, B.S. Bae, Photoionization of methylphenothiazine and photoluminescence of erbium 8-hydroxyquinolate in transparent mesoporous silica films by spin-coating on silicon. *Microporous Mesoporous Mater.* **67**, 265 (2004)
10. N.S. Makarov, *Ultrafast Two-Photon Absorption in Organic Molecules: Quantitative Spectroscopy and Applications* (Montana State University, Bozeman, 2010)
11. H. Zhang, A.S. Dvornikov et al., Single-beam two-photon-recorded monolithic multilayer optical disks. *Proc. SPIE* **4090**, 174–178 (2000)
12. D. Xu, L. Ma, 3-Dimension digital storage technology. *SPIE* **4085**, 5–10 (2000)
13. X. Cheng, H. Jia, D. Xu, Vector diffraction analysis of optical disk readout. *Appl. Opt.* **39**(34), 6436–6440 (2000)
14. Y. Wang, B. Yao, N. Menke, Y. Chen, M. Fan, Optical image operation based on holographic polarization multiplexing of fulgide film. *Chin. Opt. Lett.* **9**(s1), s10302 (2011)

15. L.-P. Chang, Hybrid solid-state disks: combining heterogeneous NAND flash in large SSDs. in *Proceedings of the 13th Asia South Pacific Design Automation Conference (ASP-DAC)*, pp. 428–433 (2008)
16. Z. Zhang, D. Xu, Diffraction analysis of optical disk read-out signal deterioration caused by edge decline of groove. in *ISOS-5th International Symposium on Optical Storage*, pp. 19–25 (2000)
17. E.P. Walker, X. Zheng, F.B. McCormick, H. Zhang, N.H. Kim, J. Costa, A.S. Dvornikov, Servo error signal generation for 2-photon recorded monolithic multilayer optical data storage. ODS 2000 Proc. SPIE **4090**, 179–184 (2000)
18. H. Zhang, A.S. Dvornikov, E.P. Walker, N.H. Kim, F.B. McCormick, Single-beam two-photon-recorded monolithic multi-layer optical disks. ODS 2000 Proc. SPIE **4090**, 174–178 (2000)
19. H. Hua, D. Xu, L. Pan, Modulation code and PRML detection for multi-level run-length-limited DVD channels. in *2006 Optical Data Storage Topical Meeting*, pp. 112–114 (2006)
20. D. Kitayama, M. Yaita, Laminated metamaterial flat lens at millimeter-wave frequencies. Opt. Expr. **23**(18), 23348–23356 (2015)
21. J. Song, K. Chen, D.-Y. Xu, Simulation and experiment study on recording mask in mastering. Optoelectron. Laser **17**(3), 265–268 (2006)
22. J. Nunn, I.A. Walmsley, M.G. Raymer, K. Surmacz, F.C. Waldermann, Z. Wang, D. Jaksch, Phys. Rev. A **75**, 011401(R) (2007)
23. D.-Y. Xu, Q. Zhang, J. Jun, Z. Lei, Replication method for gray-degree recording optical disc, Tsinghua University, CN03119279.3, 2013
24. D.-Y. Xu, X. Fan, G. Qi, Q. Kun, Control method of laser drive for multi-level mastering and burning recording, Tsinghua University, CN03121143.7, 2003
25. D.-Y. Xu, Y. Ni, L. Pan, K. Chen, J. Xiong, D. Lu, H. Wu, J. Ma, J. Pei, Replication method of multi-level CD-ROM, Tsinghua University, CN200510053509.3, 2005
26. J.Y. Bae, J.I. Jung, O.H. Park, B.S. Bae, K.T. Ranjit, L. Kevan, Synthesis and characterization of mesoporous silicafilms by spin-coating on silicon: photoionization of methylphenothiazine and photoluminescence of erbium 8-hydroxyquinolinatein mesoporous silica films. Stud. Surf. Sci. Catal. **146**, 65 (2003)
27. D.Y. Xu, S. Jie, G. Qi, P. She, Digital color disc recording and reading method, Tsinghua University, CN200410037430.7, 2005

Multi-dimensional Optical Storage

Xu, D.

2016, XIX, 679 p. 565 illus., 92 illus. in color., Hardcover

ISBN: 978-981-10-0930-3